



HAL
open science

**Numerical and experimental study of the heating of alumina under microwave field in hybrid configuration.
Application to sintering**

Inès Ghorbel

► **To cite this version:**

Inès Ghorbel. Numerical and experimental study of the heating of alumina under microwave field in hybrid configuration. Application to sintering. Other. Université de Lyon, 2021. English. NNT : 2021LYSEM021 . tel-03351332

HAL Id: tel-03351332

<https://theses.hal.science/tel-03351332>

Submitted on 22 Sep 2021

HAL is a multi-disciplinary open access archive for the deposit and dissemination of scientific research documents, whether they are published or not. The documents may come from teaching and research institutions in France or abroad, or from public or private research centers.

L'archive ouverte pluridisciplinaire **HAL**, est destinée au dépôt et à la diffusion de documents scientifiques de niveau recherche, publiés ou non, émanant des établissements d'enseignement et de recherche français ou étrangers, des laboratoires publics ou privés.



N°d'ordre NNT : 2021LYSEM021

THESE de DOCTORAT DE L'UNIVERSITE DE LYON
opérée au sein de
l'École des Mines de Saint-Etienne

École Doctorale N° 488
Sciences, Ingénierie, Santé

Spécialité de doctorat : Mécanique et Ingénierie

Soutenue publiquement le 28/06/2021, par :
Inès GHORBEL

**Étude numérique et expérimentale du
chauffage de l'alumine sous champ micro-onde
en configuration hybride. Application au
frittage**

-

**Numerical and experimental study of the
heating of alumina under microwave field in
hybrid configuration. Application to
sintering**

Devant le jury composé de :

Bouvard, Didier	Professeur	Grenoble INP	Président
Marinel, Sylvain	Professeur	ENSICAEN	Rapporteur
Silva, Luisa	Professeur	ECN	Rapporteuse
Manière, Charles	CR CNRS	CRISMAT	Examineur
Bruchon, Julien	Professeur	Mines Saint-Étienne	Directeur de thèse
Moulin, Nicolas	Maître-assistant	Mines Saint-Étienne	Co-directeur de thèse
Ganster, Patrick	Chargé de recherche	Mines Saint-Étienne	Co-encadrant de thèse
Meunier, Christophe	Ingénieur	Mines Saint-Étienne	Invité

Spécialités doctorales

SCIENCES ET GENIE DES MATERIAUX
MECANIQUE ET INGENIERIE
GENIE DES PROCEDES
SCIENCES DE LA TERRE
SCIENCES ET GENIE DE L'ENVIRONNEMENT

Responsables :

K. Wolski Directeur de recherche
S. Drapier, professeur
F. Gruy, Maître de recherche
B. Guy, Directeur de recherche
V.Laforest, Directeur de recherche

Spécialités doctorales

MATHEMATIQUES APPLIQUEES
INFORMATIQUE
SCIENCES DES IMAGES ET DES FORMES
GENIE INDUSTRIEL
MICROELECTRONIQUE

Responsables

M. Batton-Hubert
O. Boissier, Professeur
JC. Pinoli, Professeur
N. Absi, Maître de recherche
Ph. Lalevée, Professeur

EMSE : Enseignants-chercheurs et chercheurs autorisés à diriger des thèses de doctorat (titulaires d'un doctorat d'État ou d'une HDR)

ABSI	Nabil	MR	Génie industriel	CMP
AUGUSTO	Vincent	MR	Génie industriel	CIS
AVRIL	Stéphane	PR	Mécanique et ingénierie	CIS
BADEL	Pierre	PR	Mécanique et ingénierie	CIS
BALBO	Flavien	PR	Informatique	FAYOL
BASSEREAU	Jean-François	PR	Sciences et génie des matériaux	SMS
BATTON-HUBERT	Mireille	PR	Mathématiques appliquées	FAYOL
BEIGBEDER	Michel	MA	Informatique	FAYOL
BILAL	Blayac	DR	Sciences et génie de l'environnement	SPIN
BLAYAC	Sylvain	PR	Microélectronique	CMP
BOISSIER	Olivier	PR	Informatique	FAYOL
BONNEFOY	Olivier	PR	Génie des Procédés	SPIN
BORBELY	Andras	DR	Sciences et génie des matériaux	SMS
BOUCHER	Xavier	PR	Génie Industriel	FAYOL
BRUCHON	Julien	PR	Mécanique et ingénierie	SMS
CAMEIRAO	Ana	PR	Génie des Procédés	SPIN
CHRISTIEN	Frédéric	PR	Science et génie des matériaux	SMS
DAUZERE-PERES	Stéphane	PR	Génie Industriel	CMP
DEBAYLE	Johan	MR	Sciences des Images et des Formes	SPIN
DEGEORGE	Jean-Michel	MA	Génie industriel	Fayol
DELAFOSSÉ	David	PR	Sciences et génie des matériaux	SMS
DELORME	Xavier	PR	Génie industriel	FAYOL
DESRAYAUD	Christophe	PR	Mécanique et ingénierie	SMS
DJENIZIAN	Thierry	PR	Science et génie des matériaux	CMP
BERGER-DOUCE	Sandrine	PR	Sciences de gestion	FAYOL
DRAPIER	Sylvain	PR	Mécanique et ingénierie	SMS
DUTERTRE	Jean-Max	PR	Microélectronique	CMP
EL MRABET	Nadia	MA	Microélectronique	CMP
FAUCHEU	Jenny	MA	Sciences et génie des matériaux	SMS
FAVERGEON	Loïc	MR	Génie des Procédés	SPIN
FEILLET	Dominique	PR	Génie Industriel	CMP
FOREST	Valérie	PR	Génie des Procédés	CIS
FRACZKIEWICZ	Anna	DR	Sciences et génie des matériaux	SMS
GAVET	Yann	MA	Sciences des Images et des Formes	SPIN
GERINGER	Jean	MA	Sciences et génie des matériaux	CIS
GONDRAN	Natacha	MA	Sciences et génie de l'environnement	FAYOL
GONZALEZ FELIU	Jesus	MA	Sciences économiques	FAYOL
GRAILLOT	Didier	DR	Sciences et génie de l'environnement	SPIN
GRIMAUD	Frederic	EC	Génie mathématiques et industriel	FAYOL
GROSSEAU	Philippe	DR	Génie des Procédés	SPIN
GRUY	Frédéric	PR	Génie des Procédés	SPIN
HAN	Woo-Suck	MR	Mécanique et ingénierie	SMS
HERRI	Jean Michel	PR	Génie des Procédés	SPIN
ISMAILOVA	Esmá	MC	Microélectronique	CMP
KERMOUCHE	Guillaume	PR	Mécanique et Ingénierie	SMS
KLOCKER	Helmüt	DR	Sciences et génie des matériaux	SMS
LAFORÉST	Valérie	DR	Sciences et génie de l'environnement	FAYOL
LERICHE	Rodolphe	DR	Mécanique et ingénierie	FAYOL
LIOTIER	Pierre-Jacques	MA	Mécanique et ingénierie	SMS
MEDINI	Khaled	EC	Sciences et génie de l'environnement	FAYOL
MOLIMARD	Jérôme	PR	Mécanique et ingénierie	CIS
MOULIN	Nicolas	MA	Mécanique et ingénierie	SMS
MOUTTE	Jacques	MR	Génie des Procédés	SPIN
NAVARRO	Laurent	MR	Mécanique et ingénierie	CIS
NEUBERT	Gilles	PR	Génie industriel	FAYOL
NIKOLOVSKI	Jean-Pierre	Ingénieur de recherche	Mécanique et ingénierie	CMP
O CONNOR	Rodney Philip	PR	Microélectronique	CMP
PICARD	Gauthier	PR	Informatique	FAYOL
PINOLI	Jean Charles	PR	Sciences des Images et des Formes	SPIN
POURCHEZ	Jérémy	DR	Génie des Procédés	CIS
ROUSSY	Agnès	MA	Microélectronique	CMP
SANAUR	Sébastien	MA	Microélectronique	CMP
SERRIS	Eric	IRD	Génie des Procédés	FAYOL
STOLARZ	Jacques	CR	Sciences et génie des matériaux	SMS
VALDIVIESO	François	PR	Sciences et génie des matériaux	SMS
VIRICELLE	Jean Paul	DR	Génie des Procédés	SPIN
WOLSKI	Krzysztof	DR	Sciences et génie des matériaux	SMS
XIE	Xiaolan	PR	Génie industriel	CIS
YUGMA	Gallian	MR	Génie industriel	CMP

ACKNOWLEDGMENTS

Here I would like to express my gratitude to all the people who have accompanied me, who have helped me and whom I have had the chance to work with over the past three and a half years since I started my Ph.D. studies.

First of all, I would like to express my heartfelt thanks to my thesis directors and supervisor: Prof. Julien BRUCHON, Assistant Prof. Nicolas MOULIN and CR. Patrick GANSTER, who gave me the opportunity to start this Ph.D. thesis. Their excellent input and support throughout the entire Ph.D. were invaluable for completing this dissertation. My research work could not have been completed without their support and guidance. Besides my directors and supervisor, I would like to thank the members of my Ph.D. Committee: Prof. Didier BOUVARD, Prof. Sylvain MARINEL, Prof. Luisa SILVA and CR.CNRS Charles MANIERE. Thanks so much for serving as my Committee members and for their valuable suggestions.

I would also like to thank the researchers and professors at CRISMAT Caen laboratory. I am grateful for the 1 month I spent there and for the exchange of research work that we had.

I also would like to thank my family who were my backbone and support for all the phases of the Ph.D. I would like also to thank my friends for their kindness and support during the hard and good times of the studies. I would like also to thank my colleagues, researchers and staff of EMSE, for their kindness and academic exchanges.

Contents

General introduction	1
Introduction générale	5
1 Material and process	9
1.1 Introduction	10
1.2 Sintering	10
1.2.1 Definition	10
1.2.2 Stages of sintering	10
1.2.3 Diffusion phenomena	11
1.3 Microwave heating	13
1.3.1 Maxwell's equations	14
1.3.2 Electromagnetic wave/matter interactions	16
1.3.2.1 Polarization phenomena	16
1.3.2.2 MW heating for dielectric materials: complex permittivity	19
1.3.2.3 Relation between mw heating and materials' properties	21
1.3.3 Direct versus hybrid microwave heating	23
1.4 Microwave heating equipment	26
1.4.1 Microwave generators	26
1.4.2 Guided propagation	28
1.4.3 Microwave cavities	30
1.5 Materials	31
1.5.1 Alumina	31
1.5.2 Silicon Carbide	33
1.6 Conclusion	34
2 Method	37
2.1 Introduction	38
2.2 Experimental procedure	38
2.2.1 Temperature measurement	38
2.2.1.1 Thermocouple	38
2.2.1.2 Pyrometer	39
2.2.1.3 Infrared camera	41
2.2.2 Emissivity measurement	42
2.2.2.1 Literature on emissivity measurement	42
2.2.2.2 Principle of the used calibration technique	45
2.2.3 Microwave set-up	46
2.3 Numerical procedure	48

2.3.1	Modelling of microwave heating and sintering	48
2.3.1.1	EM problem: wave equation and boundary conditions	48
2.3.1.2	Thermal problem	49
2.3.1.3	Mechanics	49
2.3.1.4	Multi-physics coupling and numerical resolution	51
2.3.2	Computational domain and boundary conditions	53
2.3.3	Mesh sensibility analysis	54
2.4	Conclusion	56
3	Numerical and experimental thermal analysis for direct mw heating of SiC	59
3.1	Introduction	60
3.2	Experimental procedure	60
3.2.1	Emissivity measurement	60
3.2.2	Microwave heating	61
3.3	Numerical simulation	63
3.3.1	Numerical results	63
3.3.2	Discussion	66
3.3.3	Sensitivity analysis	67
3.3.3.1	Real part of the relative permittivity	68
3.3.3.2	Imaginary part of the relative permittivity	69
3.3.3.3	Specific heat	70
3.3.3.4	Thermal conductivity	71
3.3.4	Effect of the insulating support	72
3.4	Conclusion	74
4	Microwave heating of alumina: influence of density	77
4.1	Introduction	78
4.2	Material and methods : Experimental	78
4.2.1	Dilatometric tests	78
4.2.1.1	Evaluation of the relative density	79
4.2.1.2	Dilatometry results	80
4.2.2	Calibration of the pyrometer	81
4.3	Experimental results	82
4.4	Modelization of microwave heating of alumina at different density	85
4.4.1	Density dependence of material parameters	86
4.4.1.1	Effective medium approximation	86
4.4.2	Boundary conditions	89
4.4.3	Numerical results	89
4.5	Discussion	90
4.6	Conclusion	96
5	Towards the simulation of microwave sintering in hybrid configuration	99
5.1	Introduction	100
5.2	Microwave sintering	100
5.2.1	Experimental set-up	100
5.2.2	Development of the sintering cell	101

5.2.2.1	Choice of susceptor configuration	101
5.2.2.2	Sintering cell	103
5.2.3	Thermal cycle	104
5.3	Numerical simulations	108
5.3.1	Computational domain	108
5.3.2	Numerical model and boundary conditions	108
5.3.3	Material parameters	111
5.4	Numerical results and discussion	111
5.5	Conclusion	114
Conclusion and outlook		117
Conclusion et perspectives		121
A	Time-average of poynting vector	127
B	Heat source term	129
C	Electromagnetic-thermal material properties	131
D	Wave propagation equation	133
E	Permittivity calculation as function of relative density : EMA approximation	135
Bibliographie		137

List of Figures

1.1	Relative density during the sintering stages.	11
1.2	Thermal cycle during sintering.	11
1.3	Different diffusion mechanisms contributing to the mass transport between two particles during sintering [87].	12
1.4	Necks between the particles created during sintering [35].	13
1.5	History of microwave materials processing [44].	14
1.6	The electromagnetic spectrum with some applications depending on frequency [44].	15
1.7	3D representation of electromagnetic field components.	15
1.8	Interfacial (space-charge) polarization: spatial distribution of charges a) without an electric field b) in presence of an electric field [106].	16
1.9	Dipolar (orientation) polarization: orientation of dipoles: a) without an electric field b) in presence of an electric field.	17
1.10	Ionic polarization: displacement of opposite charges a) without an electric field b) in presence of an electric field.	17
1.11	Electronic polarization: electronic cloud and nucleus a) without an electric field b) in presence of an electric field.	18
1.12	Variation of a) the dielectric constant ϵ' and b) the loss factor ϵ'' for a typical dielectric material in a large range of frequencies [29, 106].	19
1.13	Loss factor variation as function of temperature for a low-loss ceramic [94].	20
1.14	Complex values [59] of relative permittivity of SiC from Baeraky [11] et Batt <i>et al</i> [13].	21
1.15	Microwave - material interaction.	24
1.16	Imaginary part of the dielectric permittivity versus temperature for silicon carbide and alumina materials [11, 56].	24
1.17	Microwave heating: a)direct vs b) indirect.	25
1.18	Surface temperature versus time during direct (without susceptor) and hybrid (with susceptor) microwave heating [6].	26
1.19	Frequency spectral distribution of 2.45 GHz microwave radiation for a) magnetron generator and b) solid state (semi conductor) generator [45].	27
1.20	Magnetron (left) and solid state (right) generators [45].	27
1.21	Microwave distribution in rectangular waveguide for a transverse electric mode (TE) and a transverse magnetic mode (TM) [102].	28
1.22	E-Field and H-Field distributions in different modes in rectangular waveguides [30].	29

1.23	Waveguide size: a) photograph of the different size of waveguides used for 915 MHz, 2.45 GHz and 5.8 GHz (from left to right) b) WR340 waveguide with dimensions [44].	29
1.24	Single mode cavity.	30
1.25	Multimode cavity: a) electric field distribution inside the charged multimode cavity [26], b) schematic view of a multimode cavity.	31
1.26	α -alumina structure: blue circles represent the O^{2-} anions, small black circles represent Al^{3+} cations and small empty circles vacant octahedral interstices [28].	32
1.27	Structure transformation of alumina [98].	32
1.28	Stacking sequences of the crystal structure of 3C-SiC, 4H-SiC and 6H-SiC. The chain structures that define the stacking sequence are in dark color while selected Si-C bonds are in red color [64].	34
2.1	Working principle of a thermocouple [103].	38
2.2	Spectral luminance as function of the wavelength for a black body, at different temperatures [26].	40
2.3	Schematic of the pyrometer calibration by fusion of a calibration material [53].	42
2.4	Photographs of the sample at T_a (temperature before melting point) with the four different calibration materials [53].	43
2.5	Pyrometer calibration: (a) method used [37], (b) thermal cycle.	46
2.6	Schematics (a) and photograph (b) of single-mode microwave device [37].	47
2.7	Multiphysics couplings.	51
2.8	General simulation procedure of microwave sintering.	52
2.9	3D geometry of the microwave cavity [37].	53
2.10	Microwave cavity with the different physical domains [37].	53
2.11	Boundary conditions for the microwave heating [37].	54
2.12	Mesh sensibility for coarse, fine and very fine meshes [37].	55
3.1	Apparent emissivity evolution in range of the temperature [373 K - 1173 K] (published in [37]).	60
3.2	Different orientations studied for microwave heating of a SiC sample [37]. The red point presents the measurement point of the temperature.	61
3.3	Reflected power P_r for the studied cases with an incident power $P_{in} = 50$ W [37].	62
3.4	Temperature evolution at the temperature measurement point for the four cases [37].	62
3.5	Computed electric field a) empty cavity b) cavity, sample and insulating support before resonance, c) cavity, sample and insulating support after resonance for case 1 [37].	64
3.6	Average intensity of the electric field obtained by simulation for different cavity lengths in the four investigated cases. Star markers correspond to the cavity lengths measured experimentally [37].	65

3.7	Numerically and experimentally temperature evolution at the temperature measurement point (red point) for the four cases [37].	66
3.8	Equilibrium temperature measured at red point, as a function of the cavity length for the different sample orientations [37].	67
3.9	(a) ϵ'_r evolution as function on temperature and (b) temperature evolution at the surface of a SiC sample in case 1 orientation for ϵ'_r min and ϵ'_r max values.	68
3.10	Norm of the electric field during microwave heating for ϵ'_r min and ϵ'_r max.	69
3.11	ϵ''_r sensitivity : (a) ϵ''_r evolution as function on temperature (b) Temperature evolution at a surface of a SiC sample in case 1 orientation for ϵ''_r min and ϵ''_r max values.	70
3.12	(a) C_p change over temperature, and (b) temperature change over time at a surface of a SiC sample in case 1 orientation for C_p min and C_p max values.	71
3.13	(a) κ change over temperature and, (b) temperature change over time at a surface of the SiC sample in case 1 orientation for κ min and κ max values.	72
3.14	Average electric field intensity for Hyp 1 and Hyp 2 for case 1.	73
3.15	Temperature evolution during microwave heating for Hyp 1 and Hyp 2 using case 1.	73
4.1	Working principle of dilatometer.	79
4.2	Relative density evolution as a function of the temperature for alumina sample during thermal cycle.	81
4.3	Parallelepipedic samples with 43.8 % (left), 55 % (middle) and 97 % (right) relative density	81
4.4	Apparent emissivity of alumina samples with 43.8 %, 55 % and 97 % relative densities in the temperature range [373 K - 1173 K].	82
4.5	(a) Temperature evolution and (b) the corresponding reflected power during the heating of a 55% relative density sample for 50 W power supplied.	83
4.6	(a) Temperature evolution of 55 % sample for 50 W and 100 W power supplied and (b) the corresponding reflected power.	84
4.7	Sample temperature and microwave reflected power during microwave heat for 50 W (left) and 100 W (right) power supplied of 43.8%, 55% and 97% samples.	85
4.8	Effective medium illustration [91].	87
4.9	Alumina relative permittivity as function of both temperature and relative density calculated by the EMA approximation (left) real part (right) imaginary part.	87
4.10	Alumina parameter plotted as functions of temperature for three densities ($D=43.8\%$, $D=55\%$, $D=97\%$) in the range of the temperature [300 K - 1500 K] (a) relative permittivity real part, (b) relative permittivity imaginary part, (c) specific heat and (d) thermal conductivity.	88
4.11	Boundary conditions of the thermal problem used for Alumina microwave heating.	89

4.12	Average intensity of the electric field obtained by simulation for different cavity lengths for the three densities ($D=43.8\%$, $D=55\%$ and $D=97\%$). Star markers correspond to the cavity lengths measured experimentally.	90
4.13	Temperature evolution during microwave heating, for the three densities (43.8%, 55% and 97%), obtained by numerical simulation using EMA approximation.	91
4.14	Temperature evolution during microwave heating for $D=43.8\%$, $D=55\%$ and $D=97\%$ using the new values.	92
4.15	Thermal boundary conditions while considering all the boundary of the insulating support are thermal insulating.	93
4.16	Temperature evolution during microwave for the $D=43.8\%$ alumina sample and the insulating support, measured at the red point, while considering all the boundary of the insulating support are thermal insulating.	93
4.17	(a) Temperature evolution and (b) reflected power during microwave heating with and without air cooling using a sample made of ©RATH.	95
5.1	Experimental set-up at CRISMAT laboratory.	101
5.2	Studied configurations: a) perpendicular configuration, b) parallel configuration.	102
5.3	Electric field distribution in both sample and susceptors for a) perpendicular configuration and b) parallel configuration.	103
5.4	Cell sintering: an explanatory scheme with a photograph of the thermal camera.	104
5.5	Photograph of the plasma phenomenon.	105
5.6	Applied thermal cycle.	106
5.7	The evolution of the incident, the reflected power and the piston position (PCC).	106
5.8	Temperature evolution a) at a surface of the sample measured by thermal camera and pyrometer b) at a surface of the susceptor and sample measured by the thermal camera.	107
5.9	3D geometry of the microwave cavity used for the sintering.	108
5.10	Microwave cavity with the different physical domains.	109
5.11	Boundary conditions used for the microwave sintering simulation.	110
5.12	Surface to surface radiation condition.	111
5.13	Set point, average, sample and susceptor (measured at the red points) temperatures evolution during thermal cycle with temperature iso-values at three different instants.	112
5.14	The temperature along a line passing through the insulating box, the susceptors and the sample in X direction at three different instants.	113
5.15	Delivered incident power during simulation for fixed and moving piston.	114
5.16	Volume integral of the total heat source terms in the susceptors, the sample and the insulating support.	114
E.1	Real part of the permittivity using EMA approximation for a relative density $D = 43.8\%$	136

List of Tables

1.1	Relative comparison of magnetron and solid state generator characteristics [44].	27
2.1	Base Metal Thermocouples temperature ranges [96].	38
2.2	Noble Metal Thermocouples temperature ranges [96].	39
2.3	Characteristics of the monochromatic pyrometers used for the microwave heating and sintering.	41
2.4	Characteristics of the thermal camera used for the microwave sintering. . .	42
2.5	Characteristic lengths of elements of cavity, sample and insulating support for coarse, fine and very fine meshes.	55
2.6	Mesh sensitivity analysis: number of DOF and computation time (on 12 cores of an Intel Xeon Gold 6128 bi-processor at 3.4 GHz) for three different meshes.	55
3.1	Values of material parameters for the study of sensitivity.	67
4.1	Alumina parameter evolution for three densities ($D=43.8\%$, $D=55\%$, $D=97\%$) in the range of the temperature [300 K-1500 K].	89
4.2	Measured and predicated complex permittivity of porous and sintered alumina samples at ambient temperature.	91
4.3	New values of the imaginary part of the permittivity of alumina materials. .	92
C.1	Electromagnetic-thermal material properties.	132

Nomenclature

Electromagnetic symbols

- **E** electric field (V.m^{-1})
- **D** electric displacement field (C.m^2)
- **H** magnetic field (A.m^{-1})
- **B** magnetic flux density field (T)
- **P** dielectric polarization field (C.m^2)
- **M** magnetization field (A.m^{-1})
- ϵ^* complex permittivity (F.m^{-1})
- ϵ_r^* complex relative permittivity
- ϵ_r' relative permittivity real part
- ϵ_r'' relative permittivity imaginary part
- ϵ_0 vacuum permittivity ($8.85418782 \times 10^{-12} \text{ F.m}^{-1}$)
- μ^* complex permeability (H.m^{-1})
- μ_r^* complex relative permeability
- μ_r' relative permeability real part
- μ_r'' relative permeability imaginary part
- μ_0 vacuum permeability ($4\pi \times 10^{-7} \text{ H.m}^{-1}$)
- σ_e electric conductivity (S.m^{-1})
- ω angular frequency (rad.s^{-1})
- **j** the complex number
- P_{in} incident power (W)
- P_r reflected power (W)

Thermal symbols

- $\bar{\rho}$ density (kg.m^{-3})

- C_p specific heat ($\text{J.kg}^{-1}.\text{K}^{-1}$)
- κ thermal conductivity ($\text{W.m}^{-1}.\text{K}^{-1}$)
- Φ heat flux (W.m^{-2})
- Φ_r surface to ambient radiative heat flux (W.m^{-2})
- Φ_c convective heat flux (W.m^{-2})
- σ_B Stefan-Boltzmann constant ($5.670367 \times 10^{-8} \text{ W.m}^{-2}.\text{K}^{-4}$)
- ϵ emissivity
- Q_{EM} heat source (W.m^{-3})
- h heat transfer coefficient ($5 \text{ W.m}^{-2}.\text{K}^{-1}$)
- T temperature (K)
- T_{amb} ambient temperature (K)

Mechanic symbols

- σ Cauchy stress tensor
- \mathbf{f} volume forces vector
- σ_{eq} equivalent stress
- $\dot{\epsilon}_{eq}$ equivalent strain rate
- $\bar{\rho}_{th}$ theoretical density (kg.m^{-3})
- D relative density
- $\dot{\epsilon}$ strain rate tensor
- \mathbf{I} identity tensor
- Pl sintering stress (Pa)
- α surface energy (J.m^{-2})
- r_0 average particle radius (m)
- θ porosity
- \dot{e} rate of volume change (s^{-1})
- $\dot{\gamma}$ rate of shape change (s^{-2})
- V_{pores} pores volume (m^{-3})
- V total volume (m^{-3})
- m particle mass (kg)

General introduction

Heating and subsequent sintering under microwave irradiation have been studied over the last few decades, both in the context of fundamental research [91] and industrial applications, for various materials such as metals [4, 56, 90], ceramics [27, 48, 55, 57, 59] and composites [54, 67]. Due to the penetration of the electromagnetic wave into the material, this process offers volumetric and selective heating, low energy consumption and short processing time. This PhD work focuses on ceramic materials with no or low magnetic loss. In this case, the contribution of the magnetic field to microwave heating is negligible [97, 93, 58]. Hence, the heating is only due to the electric field, and is governed by the dielectric loss. In fact, only materials with high dielectric loss at room temperature (such as silicon carbide, zinc oxide, etc) can be heated effectively in direct configuration, *i.e* without using susceptors [73]. For materials with low dielectric loss (such as alumina), a hybrid configuration using susceptors, usually in Silicon Carbide (SiC), should be used to initiate microwave heating [27, 57, 59].

Despite all the benefits of microwave heating, the process is difficult to control. Indeed, conventional temperature measuring devices, such as thermocouples, cannot be used because they interact with microwaves. For this reason, non-contact devices such as infrared pyrometers and/or thermal cameras are more suitable for monitoring and controlling the process, but they must in any case be calibrated [27, 81]. When using a single mode microwave cavity, another difficulty arises from the position of the sample which has to correspond to a maximum of the electric field for efficient heating. However, the sample disturbs the electromagnetic field during heating due to the evolution of its dielectric properties with the temperature. As a result, the electromagnetic wave no longer remains stationary, which leads to destructive interference in the electric field. Therefore, the length of the microwave cavity must be continuously adjusted during heating to keep the electric field stationary.

Understanding microwave sintering requires a multidisciplinary perspective, combining electromagnetic, thermal and mechanical approaches. Indeed, the propagation of an electromagnetic wave in a material generates heat dissipation, leading to temperature heterogeneities, which is turn active mass transport mechanisms resulting in densification of the material [72]. Moreover, the thermo-physical parameters involved in the description of these phenomena (specific heat C_p , thermal conductivity κ and complex relative permittivity ϵ_r), depend strongly on both temperature and density. To tackle this complexity, the numerical simulations are often associated with experiments to evaluate temperature fields [21, 42, 46, 55, 56, 57, 59, 108, 109, 111] in system to be heated.

This work proposes a numerical/experimental comparison of microwave heating, then

sintering, of an alumina sample, first in a direct configuration (without susceptors), then in a hybrid configuration (with SiC susceptors) in order to reach the sintering temperature. In view of the complexity and intertwining of the phenomena involved, we have endeavoured to choose simple situations, where each phenomenon can be identified almost individually. First, we consider "pure" materials (SiC or alumina) (without doping for example) in order to have access, via the literature, to their physical parameters, in particular dielectric parameters such as permeability. Then, we use a 2.45 GHz single mode microwave cavity, in order to clearly identify, experimentally or by simulation, the electric field distribution. The length of this cavity will be adjusted to the resonance length before each experiment, at room temperature, but will not be modified during heating, in order to limit the number of parameters in the simulations. An exception will be made for the sintering study. Finally, the situations that we address are of increasing complexity: the study of the orientation in the electric field of a SiC sample, which is a material that couples strongly with microwaves; the study of direct microwave heating of alumina samples of different densities; the study of microwave heating of the alumina/SiC couple, up to the sintering of the alumina. In each situation, the comparison between simulation and experiment allows us to analyse the predominant phenomena and to evaluate if the model used takes them into account correctly. Moreover, the simulation allows access to volume quantities that are inaccessible by experiments.

This manuscript is structured in five Chapters:

The first chapter is an introductory chapter, presenting the sintering process, Maxwell's equations and the description of the electromagnetic wave/matter interaction. In addition, the properties of alumina and silicon carbide, the materials of interest in this work, are briefly mentioned.

The second chapter presents the experimental set-up and numerical strategy used to study the microwave heating of silicon carbide (Chapter 3) and alumina (Chapter 4) samples, as well as the microwave heating of the Alumina - SiC system (Chapter 5), leading to the sintering of alumina.

The third chapter is dedicated to the numerical and experimental analysis of the direct microwave heating of a parallelepipedic SiC sample. The effect of the orientation of the sample in the electric field and the length of the cavity on microwave heating is investigated.

Chapter 4 focuses on determining the influence of density on the thermo-physical properties of alumina and consequently on its microwave heating. Numerical and experimental investigations are also carried out to understand the complex behaviour of the temperature observed in the experiments.

The fifth chapter proposes a prospective work on the microwave sintering of alumina in hybrid configuration, treated both from an experimental and a modelling/simulation point of view. This work was carried out in collaboration between Mines Saint-Étienne

and the CRISMAT laboratory in Caen.

Finally, the conclusions are drawn from this PhD work as well as some perspectives related to future works.

Introduction générale

Le chauffage et le frittage sous champ micro-ondes ont été étudiés au cours des dernières décennies, dans le cadre de la recherche fondamentale [91] ainsi que dans celui des applications industrielles, pour divers matériaux tels que les métaux [4, 56, 90], les céramiques [27, 48, 55, 57, 59] et les composites [54, 67]. Grâce à la pénétration de l'onde électromagnétique dans le matériau, ce procédé permet d'obtenir un chauffage volumique et sélectif, une faible consommation d'énergie et un temps de traitement court. Ce travail de thèse se concentre sur les matériaux céramiques à perte magnétique nulle ou faible. Dans ce cas, la contribution du champ magnétique au chauffage par micro-ondes est négligeable [97, 93, 58]. Par conséquent, l'échauffement est uniquement dû au champ électrique et est régi par la perte diélectrique. En effet, seuls les matériaux à forte perte diélectrique (tels que le carbure de silicium, l'oxyde de zinc, etc.) peuvent être chauffés efficacement à température ambiante en configuration directe, c'est-à-dire sans utiliser de suscepteurs [73]. Pour les matériaux à faible perte diélectrique (comme l'alumine), une configuration hybride utilisant des suscepteurs, généralement en carbure de silicium (SiC), doit être utilisée pour initier le chauffage par micro-ondes [27, 57, 59].

Malgré tous les avantages du chauffage par micro-ondes, le procédé est difficile à contrôler. En effet, les dispositifs conventionnels de mesure de la température, tels que les thermocouples, ne peuvent pas être utilisés car ils interagissent avec les micro-ondes. C'est pourquoi les dispositifs sans contact tels que les pyromètres infrarouges et/ou les caméras thermiques sont plus adaptés à la surveillance et au contrôle du procédé, mais ils doivent dans tous les cas être étalonnés [27, 81]. Lors de l'utilisation d'une cavité micro-ondes monomode, une autre difficulté provient de la position de l'échantillon qui doit correspondre à un maximum du champ électrique pour un chauffage efficace. Il apparaît également que, l'échantillon perturbe le champ électromagnétique pendant le chauffage en raison de l'évolution de ses propriétés diélectriques avec la température. Par conséquent, l'onde électromagnétique ne reste plus stationnaire, ce qui entraîne une interférence destructive dans le champ électrique. La longueur de la cavité micro-ondes doit alors être ajustée en permanence pendant le chauffage pour que le champ électrique reste stationnaire.

La compréhension du frittage par micro-ondes nécessite une approche multidisciplinaire, combinant des domaines électromagnétiques, thermiques et mécaniques. En effet, la propagation d'une onde électromagnétique dans un matériau génère une dissipation de chaleur, conduisant à des hétérogénéités de température, qui à leur tour activent des mécanismes de transport de masse entraînant une densification du matériau [72]. De plus, les paramètres thermo-physiques intervenant dans la description de ces phénomènes (chaleur spécifique C_p , conductivité thermique κ et la permittivité relative complexe ϵ_r),

dépendent fortement de la température et de la densité. Pour faire face à cette complexité, les simulations numériques sont souvent associées à des expériences pour évaluer les champs de température [21, 42, 46, 55, 56, 57, 59, 108, 109, 111] dans le système à chauffer.

Ce travail propose une comparaison numérique/expérimentale du chauffage par micro-ondes, puis du frittage, d'un échantillon d'alumine, d'abord dans une configuration directe (sans suscepteurs), puis dans une configuration hybride (avec des suscepteurs en SiC) afin d'atteindre la température de frittage. Compte tenu de la complexité et de l'imbrication des phénomènes en cause, nous nous sommes efforcés de choisir des situations simples, dans lesquelles chaque phénomène peut être identifié de manière quasi individuelle. Tout d'abord, nous considérons des matériaux " purs " (SiC ou alumine sans dopage) afin d'avoir accès, via la littérature, à leurs paramètres physiques, en particulier les paramètres diélectriques tels que la perméabilité. Ensuite, nous utilisons une cavité micro-onde monomode de 2.45 GHz, afin de bien identifier, expérimentalement ou par simulation, la distribution du champ électrique. La longueur de cette cavité sera ajustée à la longueur de résonance avant chaque expérience, à température ambiante, mais ne sera pas modifiée pendant le chauffage, afin de limiter le nombre de paramètres dans les simulations. Une exception sera faite pour l'étude de frittage. Enfin, les situations que nous abordons sont de plus en plus complexes : l'étude de l'orientation dans le champ électrique d'un échantillon de SiC, qui est un matériau qui se couple fortement avec les micro-ondes; l'étude du chauffage direct par micro-ondes d'échantillons d'alumine de différentes densités ; l'étude du chauffage par micro-ondes du couple alumine/SiC, jusqu'au frittage de l'alumine. Dans chaque situation, la comparaison entre simulation et expérience permet d'analyser les phénomènes prédominants et d'évaluer si le modèle utilisé les prend correctement en compte. De plus, la simulation permet d'accéder à des quantités de volume inaccessibles par les expériences.

Ce manuscrit est structuré en cinq chapitres :

Le premier chapitre est un chapitre introductif, présentant le processus de frittage, les équations de Maxwell et la description de l'interaction onde électromagnétique/matière. Dans ce chapitre, les propriétés de l'alumine et du carbure de silicium, matériaux qui nous intéressent dans ce travail, sont également présentés.

Le deuxième chapitre présente le montage expérimental et la stratégie numérique utilisés pour étudier le chauffage par micro-ondes d'échantillons de carbure de silicium (Chapitre 3) et d'alumine (Chapitre 4), ainsi que le chauffage par micro-ondes du système Alumine - SiC (Chapitre 5), conduisant au frittage de l'alumine.

Le troisième chapitre est consacré à l'analyse numérique et expérimentale du chauffage direct par micro-ondes d'un échantillon parallélépipédique en SiC. L'effet de l'orientation de l'échantillon dans le champ électrique et de la longueur de la cavité sur le chauffage par micro-ondes est étudié.

Le chapitre 4 s'attache à la détermination de l'influence de la densité sur les propriétés thermo-physiques de l'alumine et par conséquent de son chauffage par micro-ondes. Des investigations numériques et expérimentales sont également menées pour comprendre l'évolution complexe de la température qui est observée dans les expériences.

Le cinquième chapitre propose un travail prospectif sur le frittage micro-ondes de l'alumine en configuration hybride, traité tant d'un point de vue expérimental que de modélisation/simulation. Ce travail a été réalisé en collaboration entre Mines Saint-Étienne et le laboratoire CRISMAT de Caen.

Enfin, les conclusions sont tirées de ce travail de thèse ainsi que quelques perspectives liées à de futurs travaux.

Chapter 1

Material and process

Contents

1.1 Introduction	10
1.2 Sintering	10
1.2.1 Definition	10
1.2.2 Stages of sintering	10
1.2.3 Diffusion phenomena	11
1.3 Microwave heating	13
1.3.1 Maxwell's equations	14
1.3.2 Electromagnetic wave/matter interactions	16
1.3.3 Direct versus hybrid microwave heating	23
1.4 Microwave heating equipment	26
1.4.1 Microwave generators	26
1.4.2 Guided propagation	28
1.4.3 Microwave cavities	30
1.5 Materials	31
1.5.1 Alumina	31
1.5.2 Silicon Carbide	33
1.6 Conclusion	34

1.1 Introduction

The control of microwave sintering can only be achieved by characterizing the phenomena occurring during the process, their physical and mathematical modelling, and the confrontation between experimental and numerical results. However, this program is still challenging since it requires the interaction between different fields of expertise: skills in experimental characterization, physical modelling in the fields of diffusion, thermo-mechanics and electromagnetism, and finally skills in numerical simulation. That is why a literature review is first necessary to get onto this subject. For that, a description of sintering process with the different stages and diffusion phenomena is first presented. The second section is dedicated to the microwave heating where Maxwell's equations, the wave propagation, the electromagnetic wave/matter interaction are described. The complex permittivity which is a key parameter for the wave/matter interaction is then introduced as it can influence the choice of the microwave heating set-up : direct heating for high dielectric loss materials and hybrid configurations for low dielectric loss material. The fourth section is devoted to the description of different microwave generators and cavities. The aim of this PhD work, is to study the microwave heating/sintering of two materials: silicon carbide and alumina. A description of these materials is given in the fifth section.

1.2 Sintering

1.2.1 Definition

Sintering is the consolidation of a compacted powder under the action of heat in order to obtain a material with a desired density and microstructure. Several mass transport mechanisms, notably by diffusion, are activated by the thermal treatment associated with this the process. Two types of sintering can be considered:

- Solid state sintering, where the temperature of all the particles or grains is below the melting temperature of the material.
- Liquid state sintering, where some components of the material can melt.

This work investigates the solid-state sintering. Stages of sintering and diffusion phenomena will be presented in next sections.

1.2.2 Stages of sintering

Based on the evolution of the relative density, sintering process can be described through three stages as shown in Figure 1.1. After the initial shaping step, consisting in compacting the powder to obtain the green sample with a given porosity, three stages can be distinguished in the sintering of a sample.

1. First stage: creation of necks between the grains by surface diffusion. This diffusion path does not densify the material. The relative density remains between 0.55 and 0.65 for ceramics [86].

2. Intermediate stage: densification of the material under the action of volume diffusion and grain boundary diffusion. This latter diffusion path is essential for the densification. The relative density evolves from 0.65 to more than 0.9, the open pores are eliminated, and only pores trapped in the solid (closed porosity) remain at the end of this stage.
3. Final stage: closed porosity is eliminated by the transport of gas molecules along the grain boundaries. The relative density becomes very close to 1.

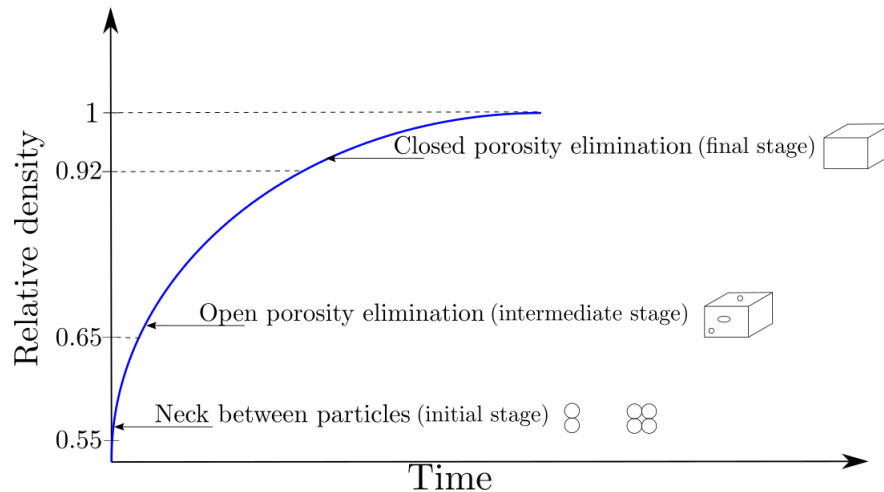


FIGURE 1.1 – Relative density during the sintering stages.

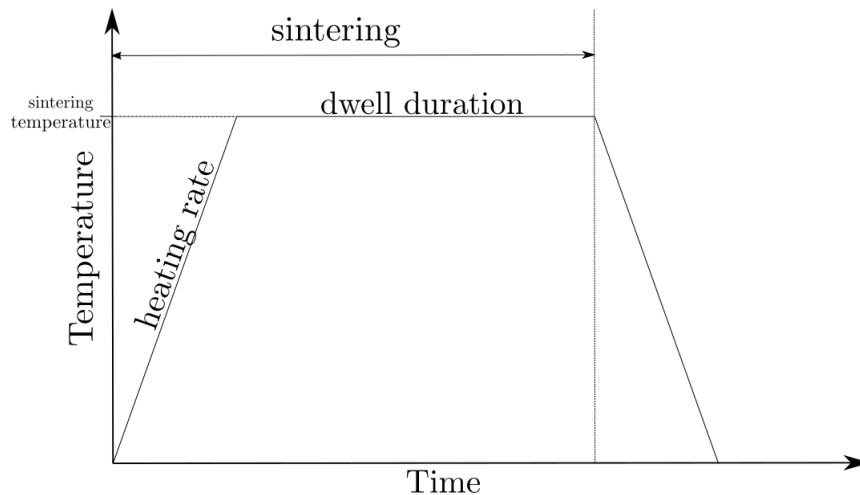


FIGURE 1.2 – Thermal cycle during sintering.

Figure 1.2 shows the thermal cycle associated with the sintering process. The cycle corresponds to control the heating rate until the sintering temperature which is maintained for a time. The heating rate, the sintering temperature and the dwell time are key parameters as they determine the final temperature and thus, the material properties.

1.2.3 Diffusion phenomena

As already mentioned, during sintering, the microstructure of the material changes due to thermo-activated mass transport phenomena, through different diffusion paths

which correspond to surface, grain boundary and volume (bulk) diffusion. These phenomena are represented at the scale of two grains in Figure 1.3. While surface diffusion contribute to the adhesion and growth of the necks between particles without densification [9] (see Figure 1.4), volume and grain boundary mechanisms induce densification:

- On the surface, material transport is a non densifying mechanism, *i.e* taking place without reducing the distance between the centres of the grains. It includes the surface diffusion, the volume diffusion from the surface, and the vapor transport (numbered 1, 2 and 3 respectively in Figure 1.3). The atoms are simply redistributed over the surface, and more specifically towards the neck between two grains.
- On the volume, material transport is a densifying mechanism, *i.e* reducing the distance between the centres of the grains and consequently implying the shrinkage of the material. It includes volume and grain boundary diffusion paths, or a combination of both (numbered 4 and 5 in Figure 1.3). A plastic flow, due to dislocation motion (number 6), can also be considered in metals, but it can be neglected for ceramic materials.

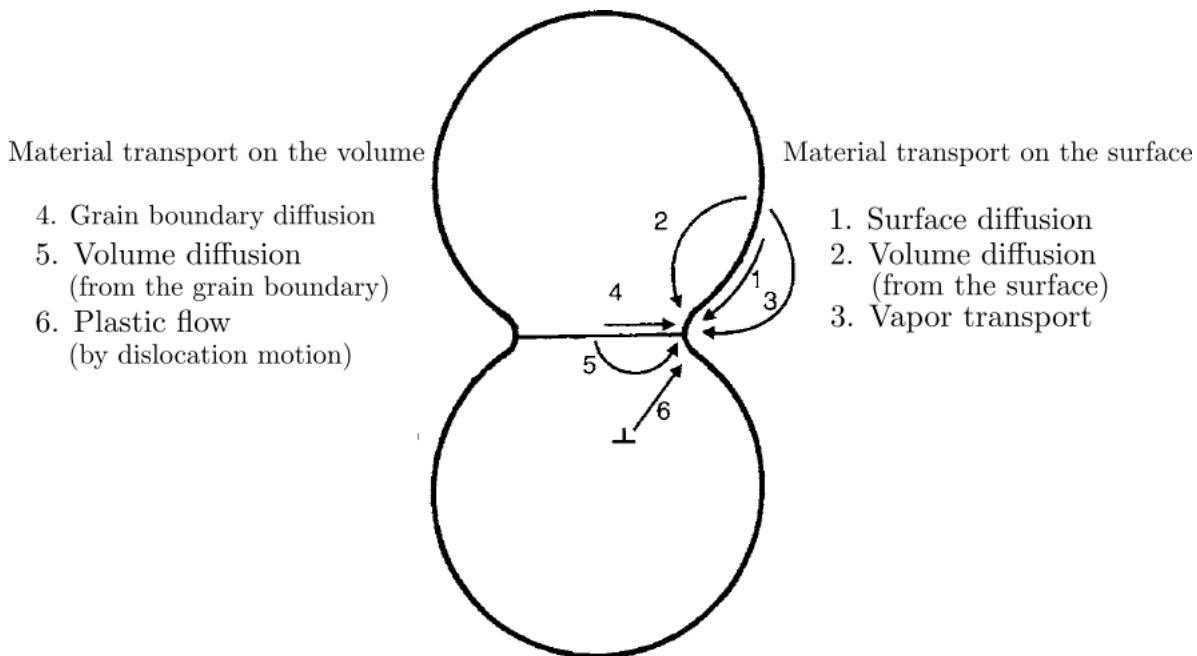


FIGURE 1.3 – Different diffusion mechanisms contributing to the mass transport between two particles during sintering [87].

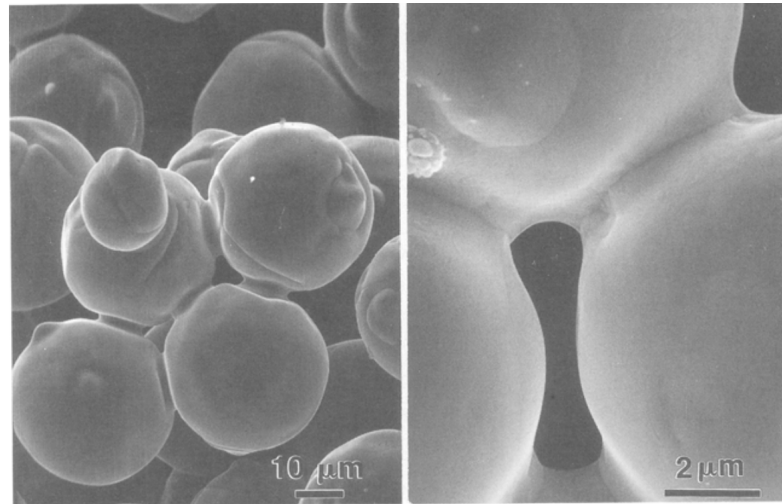


FIGURE 1.4 – Necks between the particles created during sintering [35].

1.3 Microwave heating

Traditionally, the sintering of ceramics is carried out in a conventional furnace where the material is heated by: radiation/convection from a heater resistor to the material followed by heat transfer within the material (from outside to inside). New heating techniques have been developed in recent decades in order to decrease the energy consumption or to optimize the process time [2, 3, 101]). Among these techniques, we can mention SPS (Spark Plasma Sintering) process [34, 76], induction sintering [41, 70], flash sintering [16, 74], microwave sintering [44, 75], etc.

In this work, we are interested with microwave heating. The history of microwave materials processing is briefly presented in Figure 1.5 which traces the beginnings of microwave material processing back to 1920 with the development of magnetrons. In 1947, Raytheon introduced the first commercial microwave oven [44], which was developed later on 1952 [45]. In the latter half of 1970's, the technology of microwave sintering of ceramics was discovered. Subsequently, during the 80's various fundamental researches were applied to sintering of different ceramics. And at the end of 80's, various studies in the Unites-State showed an acceleration of the sintering kinetics associated to a decrease in sintering temperature. Since then, different researches had been developed on this effect, known as the "microwave effect".

In a microwave oven, the material couples with the electromagnetic field and the electromagnetic energy is converted into thermal energy. In this case, and contrary to the heating in a conventional furnace, the material itself is a source of heat. Microwave heating has several advantages over conventional heating [2, 3, 5, 19, 22, 99, 101] such as volumetric and selective heating, energy saving (according to Agrawal *et al* [3, 5]: in some cases up to 90% energy saving have been reported, and according to Bykov *et al* [19] the energy consumption in the process of sintering alumina-based ceramic at a temperature of 1600°C is about 4 kW.h⁻¹.kg⁻¹ for microwave heating versus 59 kW.h⁻¹.kg⁻¹ for fast conventional heating in a resistive oven), rapid heating, property-improving (changes in densification kinetics provide much finer microstructures in the sintered product, which gives a much higher yield mechanical properties [5]).

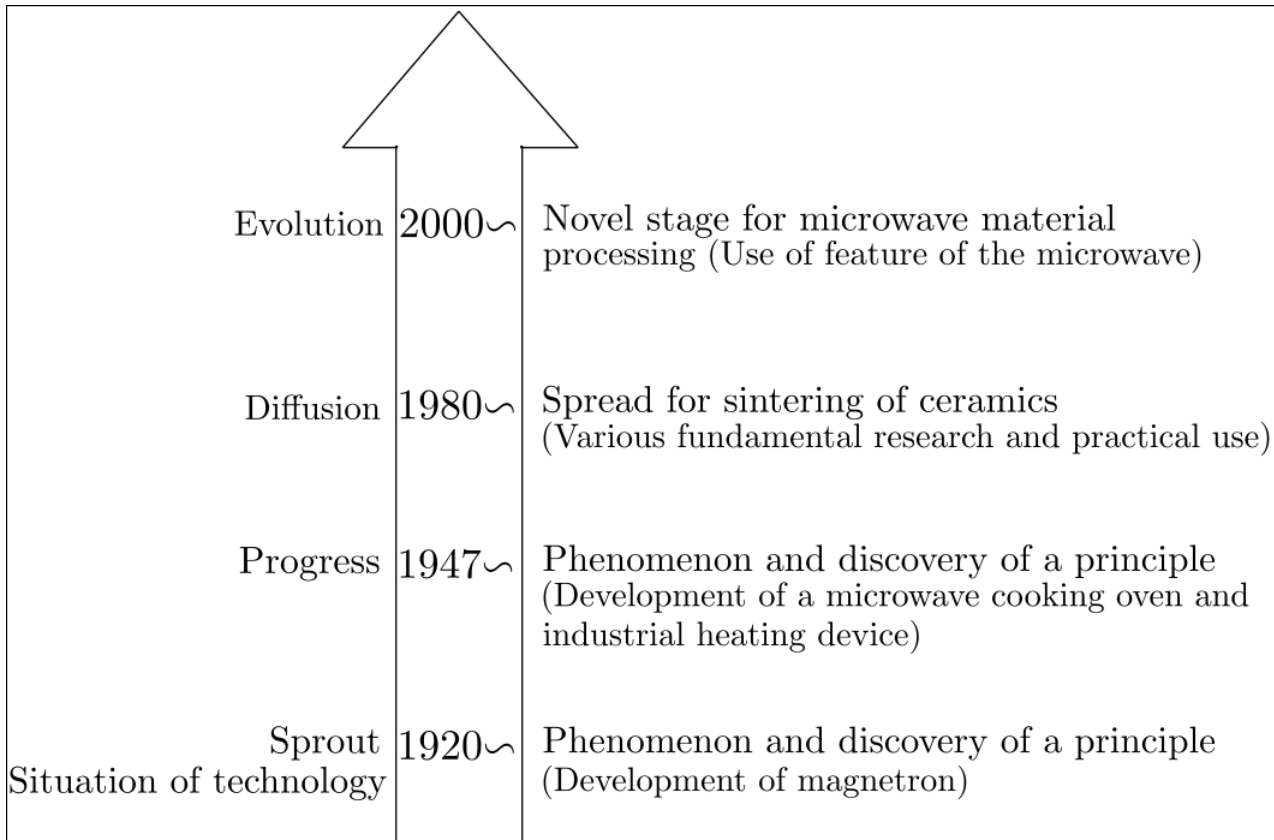


FIGURE 1.5 – History of microwave materials processing [44].

The next part of this chapter presents the principle of microwave heating, the interaction of the electromagnetic field with matter and an explanation of the difference between direct and indirect microwave heating which will be used later in this work.

1.3.1 Maxwell's equations

Microwaves are electromagnetic waves with a frequency f ranging from 300 MHz to 300 GHz corresponding to a wavelength λ ranging from 1 mm to 1 m (Figure 1.6). According to Horikoshi *et al* [45], "microwaves as all electromagnetic waves, are characterised that they (i) have no mass, (ii) cannot collide with each other, (iii) are free to move at the speed of the light, (iv) possess significant energy and (v) are reflected on a metal surface". As described in Figure 1.7, electromagnetic waves are composed of an electric field \mathbf{E} , associated to a magnetic field \mathbf{H} , such that \mathbf{E} and \mathbf{H} are orthogonal to each other and are both perpendicular to the propagation vector \mathbf{k} , with the relation $\|\mathbf{k}\| = 2\pi/\lambda$.

1.3. Microwave heating

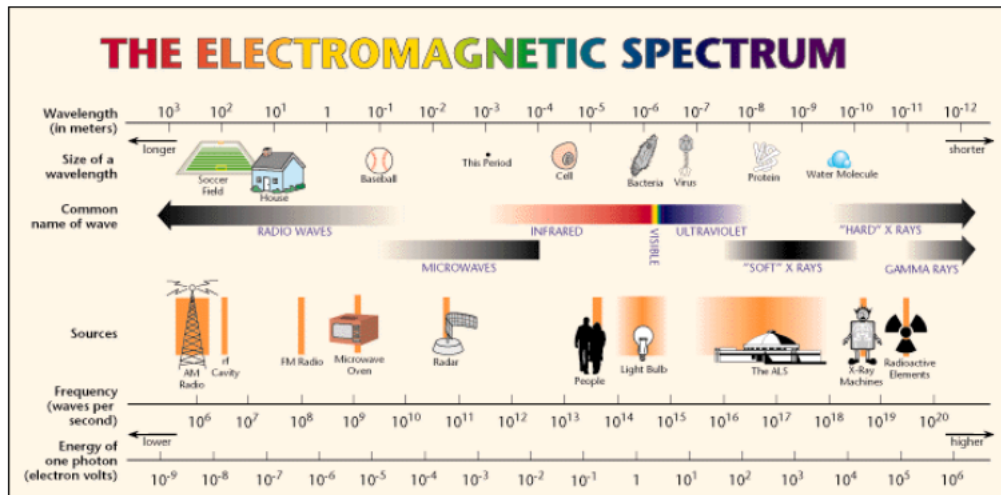


FIGURE 1.6 – The electromagnetic spectrum with some applications depending on frequency [44].

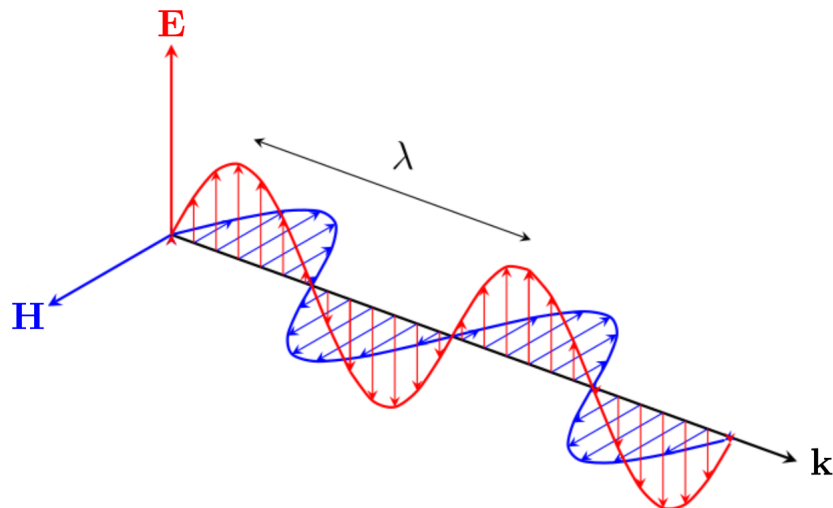


FIGURE 1.7 – 3D representation of electromagnetic field components.

The electromagnetic wave propagates through vacuum or materials. The behaviour of the electric and magnetic fields generated by accelerating or oscillating electric charges is described by Maxwell's equations:

- Gauss's law:

$$\nabla \cdot \mathbf{D} = \rho \quad (1.1)$$

- Flux's law:

$$\nabla \cdot \mathbf{B} = 0 \quad (1.2)$$

- Faraday's law:

$$\nabla \times \mathbf{E} = -\frac{\partial \mathbf{B}}{\partial t} \quad (1.3)$$

- Ampere' law:

$$\nabla \times \mathbf{H} = \mathbf{J} + \frac{\partial \mathbf{D}}{\partial t} \quad (1.4)$$

where ρ is the charge density, \mathbf{D} is the electric displacement field, \mathbf{B} is the magnetic flux density, \mathbf{J} is the current density.

1.3.2 Electromagnetic wave/matter interactions

When an electromagnetic wave penetrates a material, the electric and magnetic fields of microwave agitate the orientation, position and movement of dipoles [67]. The interaction of the electromagnetic field with the matter is represented by the following relations:

$$\mathbf{D} = \varepsilon_0 \mathbf{E} + \mathbf{P} = \varepsilon^* \mathbf{E} \quad (1.5)$$

$$\mathbf{J} = \sigma_e \mathbf{E} \quad (1.6)$$

$$\mathbf{B} = \mu_0 \mathbf{H} + \mathbf{M} = \mu^* \mathbf{H} \quad (1.7)$$

where ε_0 is vacuum permittivity ($\varepsilon_0 = 8.85418782 \times 10^{-12}$ F/m), \mathbf{P} is the polarization field, ε^* is the complex dielectric permittivity (characterising the interaction of non-free charges with the electric field), σ_e is the electric conductivity (characterising the interaction of free charges with the electric field), μ_0 is the vacuum permeability, \mathbf{M} is magnetization field and μ^* is the complex magnetic permeability (interaction with magnetic field).

1.3.2.1 Polarization phenomena

The interaction of the electric field with a material generates a redistribution of the electric charges, called polarization. These polarizations include space charge polarization, dipolar polarization, ionic polarization and electronic polarization.

- Space charge (interfacial) polarization: this type of polarization is involved in heterogeneous materials (composed of several phases) and for low frequencies (Figure 1.12). Under the effect of an electric field, the charges that can move are attracted to the interfaces of the different phases (Figure 1.8). The accumulation of these charges forms this interfacial polarization.

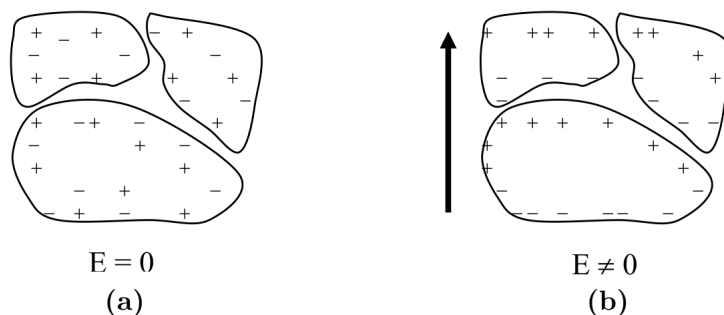


FIGURE 1.8 – Interfacial (space-charge) polarization: spatial distribution of charges a) without an electric field b) in presence of an electric field [106].

- Dipolar (orientation) polarization: this type of polarization is related to the dipole orientation. Indeed, in the absence of an electric field, the dipoles are randomly

oriented so no polarization exists (Figure 1.9 a)). Once an electric field is applied, these dipoles reorient themselves in order to be parallel to the E field (Figure 1.9 b)). The frequency of this polarization is 10^9 Hz, corresponding to microwaves (Figure 1.12).

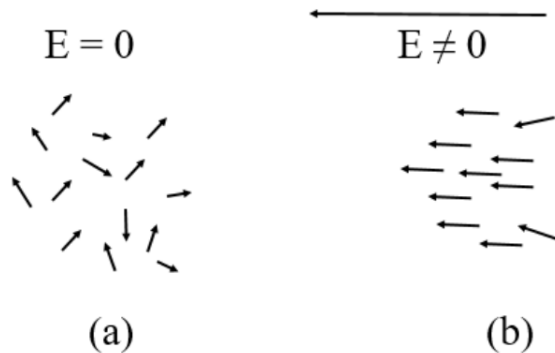


FIGURE 1.9 – Dipolar (orientation) polarization: orientation of dipoles: a) without an electric field b) in presence of an electric field.

- Ionic polarization: this type of polarization is defined as the displacement of opposite charges or groups of atoms in equilibrium positions under an electric field (Figure 1.10). It is active only for frequencies corresponding to infrared range frequencies (10^{12} to 10^{13} Hz, see Figure 1.12).

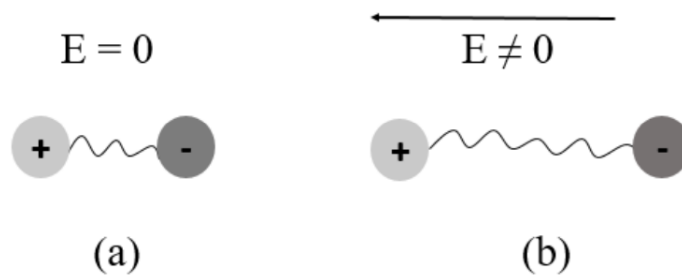


FIGURE 1.10 – Ionic polarization: displacement of opposite charges a) without an electric field b) in presence of an electric field.

- Electronic polarization: this phenomenon is present in all dielectrics, and is based on the fact that under an electric field, the electron cloud in each atom is slightly displaced with respect to the nucleus, giving an induced dipole (Figure 1.11). This effect occurs at the low frequencies, but becomes preponderant around 10^{14} Hz (Figure 1.12).

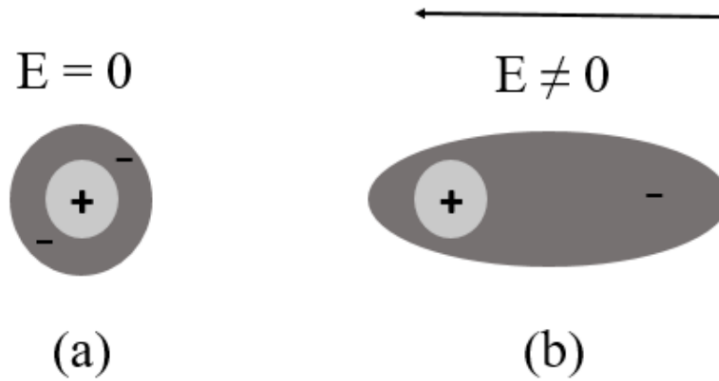


FIGURE 1.11 – Electronic polarization: electronic cloud and nucleus a) without an electric field b) in presence of an electric field.

All these phenomena appear in the real and imaginary parts of the complex permittivity $\epsilon^* = \epsilon' - j\epsilon''$ (with $j^2 = -1$), which is presented in the next paragraph. Figure 1.12 shows the dielectric parameters as functions of frequency: the higher the frequency is, the lower the different dielectric polarizations are. In fact, when the frequency increases, the dipoles no longer have enough time to respond to the electric field. As a result, no motion is induced in the molecules, no energy is dissipated by this means, and no heating occurs by dielectric polarization [106]. However, for microwave frequency (red box in Figure 1.12), there is a contribution of polarization mechanisms to the material heating. Figure 1.12 shows also that each maximum of ϵ'' coincides with a change of regime, or more precisely with a limit of absorption of a type of load. The frequencies associated with this phenomenon correspond to the natural resonance frequencies for which absorption by this type of load is maximum.

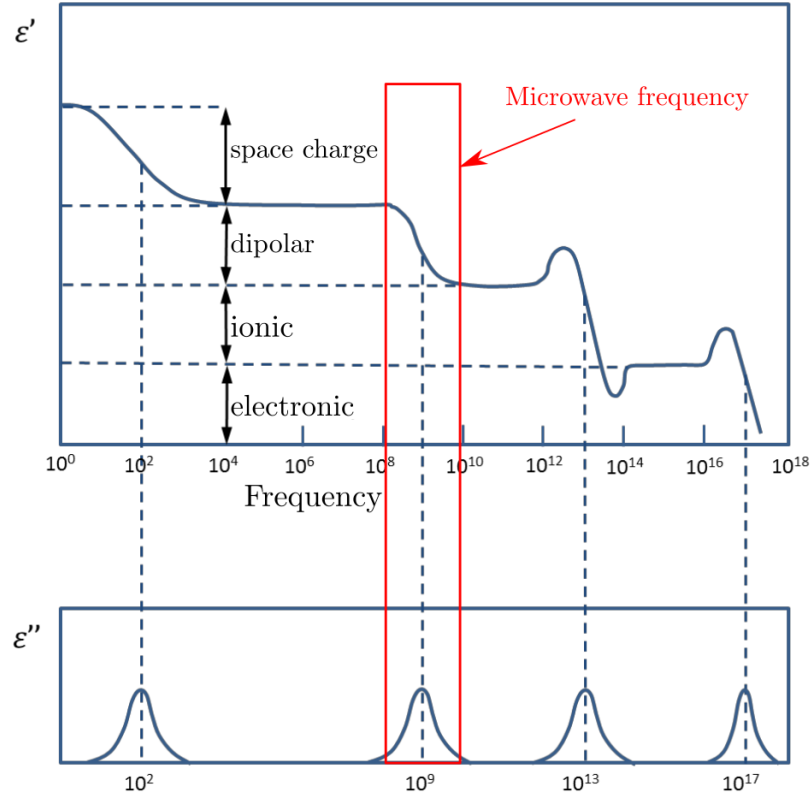


FIGURE 1.12 – Variation of a) the dielectric constant ϵ' and b) the loss factor ϵ'' for a typical dielectric material in a large range of frequencies [29, 106].

1.3.2.2 Microwave heating for dielectric materials: complex permittivity

In this work, we are interested with ceramic materials, which are considered as dielectric materials. For dielectric materials, it is necessary to quantify the electromagnetic wave-matter interaction. This interaction is macroscopically, described by the complex relative permittivity:

$$\epsilon^* = \epsilon'(\omega) - j\epsilon''(\omega) = \epsilon_0(\epsilon'_r - j\epsilon''_r) = \epsilon_0\epsilon_r^* \quad (1.8)$$

where ϵ' is the real part of the complex permittivity, ϵ'' is the imaginary part of the complex permittivity, ϵ_r^* is the complex relative permittivity, ϵ'_r , ϵ''_r are the real and the imaginary part of the complex relative permittivity and j the complex number such as $j^2 = -1$. ω is the wave frequency.

The dielectric permittivity reflects the response of a given medium to an applied electric field. In fact the term ϵ' (called dielectric constant) is associated to the ability of the medium to store potential energy from the field, while ϵ'' (called dielectric loss) is related to dissipation of this energy into heat. We can then define a loss factor $\tan \delta$ as [44]:

$$\tan \delta = \frac{\epsilon''}{\epsilon'} = \frac{\epsilon''_r}{\epsilon'_r} \quad (1.9)$$

In addition to dielectric losses, another physical loss mechanism can also absorb electrical energy and convert it into heat. This property is called electrical conductivity σ_e , where as a result of the movement of free charges, an electrical current can be created and dissipated as heat by joule effect. The total imaginary part of the permittivity is then

the sum of the dielectric losses and the conductive losses [63, 89]:

$$\varepsilon_t'' = \varepsilon'' + \frac{\sigma_e}{\omega\varepsilon_0} \quad (1.10)$$

And the loss factor $\tan\delta$ will be written as:

$$\tan\delta = \frac{\varepsilon''}{\varepsilon'} = \frac{\varepsilon_r''}{\varepsilon_r'} + \frac{\sigma_e}{\omega\varepsilon_0\varepsilon_r'} \quad (1.11)$$

Figure 1.13 presents how loss factor behaves with temperature for low-loss ceramic. It shows that $\tan\delta$ is low at ambient temperature, while beyond a critical temperature, the loss factor rises rapidly and the matter couples with microwaves. That's why for low-loss material at room temperature, it's necessary to use a susceptor (material with high dielectric loss at ambient temperature) in order to initiate the heating under microwaves at room temperature.

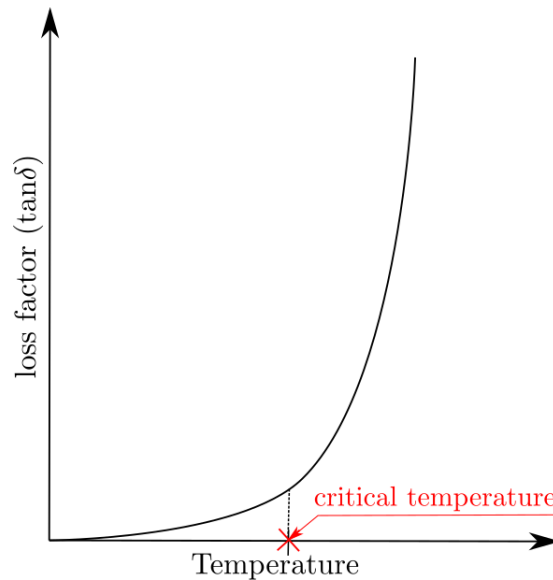


FIGURE 1.13 – Loss factor variation as function of temperature for a low-loss ceramic [94].

The dielectric permittivity is a key parameter for the microwave-matter interaction. However, the value of this parameter is difficult to obtain, in particular when considering its changes with temperature. For example, for silicon carbide, two main references exist in the literature which are Batt *et al* [13] and Baeraky [11], whose results are presented in Figure 1.14. One of the interests of this work is therefore, by comparing numerical simulations and experiments of heating, to determine the reliability of these data.

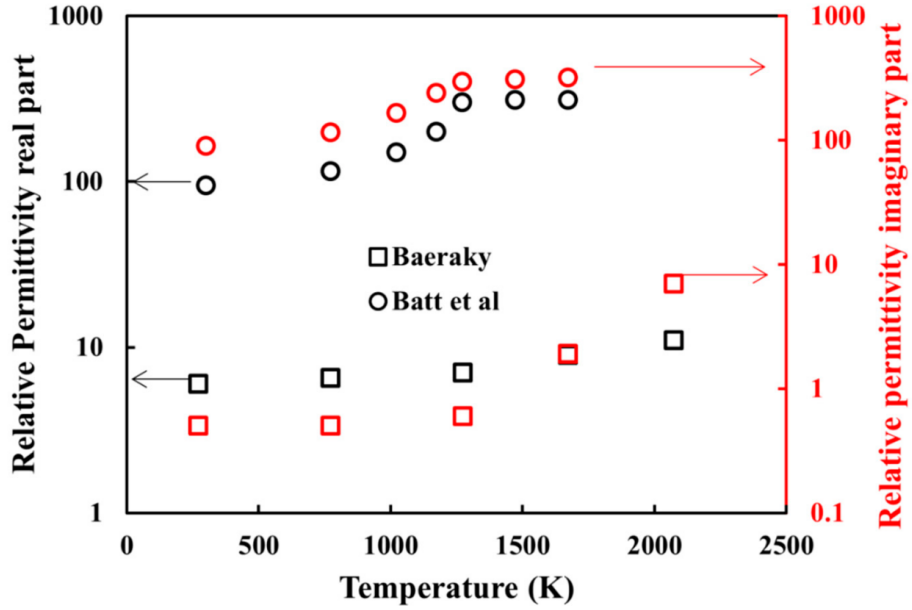


FIGURE 1.14 – Complex values [59] of relative permittivity of SiC from Baeraky [11] et Batt *et al* [13].

By analogy with the dielectric parameters, a material can heat under the action of a magnetic field. In this case, the magnetic permeability (μ^*) represents how a material dissipates the magnetic energy into heat. The magnetic permeability parameter is especially relevant for ferromagnetic materials. For most of non-magnetic materials these losses are negligible [58, 93, 97].

1.3.2.3 Relation between microwave heating and materials' physical properties

Heat source

The effect of the electromagnetic wave - materials interaction is described by the heat source term Q_{EM} (power density, $\text{W}\cdot\text{m}^{-3}$). The term Q_{EM} can be calculated from the integration of Poynting vector $\Pi(t) = \mathbf{E} \times \mathbf{H}$ across a closed surface S [40, 47]:

$$Q_{EM} = - \oint_S (\mathbf{E} \times \mathbf{H}) \cdot d\mathbf{S} \quad (1.12)$$

The average heat source obtained from Equation (1.12) is given as in [38] (the demonstration is given in Appendix A):

$$Q_{EM} = -\frac{1}{2} \oint_S \text{Re}(\tilde{\mathbf{E}} \times \bar{\tilde{\mathbf{H}}}) \cdot d\mathbf{S} \quad (1.13)$$

where $\tilde{\mathbf{E}}$ is the complex representation of the electric field and $\bar{\tilde{\mathbf{H}}}$ is the conjugate of the complex representation of the magnetic field.

The complex representation of the electric and magnetic fields can be written as:

$$\tilde{\mathbf{E}} = \tilde{\mathbf{E}}_m e^{j\omega t} = \tilde{\mathbf{E}}_m (\cos(\omega t) + j \sin(\omega t)) \quad (1.14)$$

$$\tilde{\mathbf{H}} = \tilde{\mathbf{H}}_m e^{j\omega t} = \tilde{\mathbf{H}}_m (\cos(\omega t) + j \sin(\omega t)) \quad (1.15)$$

where $\tilde{\mathbf{E}}_m$ and $\tilde{\mathbf{H}}_m$ contain the space dependence and the phase, ω is the angular frequency and j is the complex number such as $j^2 = -1$.

Using the divergence theorem, Maxwell's equations, and considering the electric field uniform throughout the volume, then the simplified equation for the absorbed power by the material per unit volume (*i.e.* the heat source) is given by Equation 1.16, whose demonstration can be found in Appendix B:

$$Q_{EM} = \frac{1}{2} \sigma_e \tilde{\mathbf{E}}_m^2 + \frac{\omega}{2} \epsilon_0 \epsilon_r'' \tilde{\mathbf{E}}_m^2 + \frac{\omega}{2} \mu_0 \mu_r'' \tilde{\mathbf{H}}_m^2 \quad (1.16)$$

The heat source Q_{EM} is the sum of three terms: the first one represents the heating by conduction loss, the second corresponds to the dielectric heating, whereas magnetic loss heating is described by the third term. However, for dielectric materials, the magnetic part of the heat source can be neglected [58, 93, 97], and Equation (1.16) can consequently be simplified as:

$$Q_{EM} = \frac{1}{2} (\sigma_e + \omega \epsilon_0 \epsilon_r'') \tilde{\mathbf{E}}_m^2 \quad (1.17)$$

Penetration depth

In addition, the penetration of the electric field in the material can be evaluated by a quantity, the penetration depth D_p , expressed with respect to the dielectric parameters as:

$$D_p = \frac{\lambda_0}{2\pi} \sqrt{\frac{1}{2\mu\epsilon_0\epsilon'}} \left[\sqrt{1 + \left(\frac{\epsilon_t''}{\epsilon'}\right)^2} - 1 \right]^{-1/2} \quad (1.18)$$

In the case of low loss dielectrics, $\epsilon_t'' \ll \epsilon'$, Equation 1.18 becomes [105, 66]:

$$D_p = \frac{\lambda_0 \sqrt{\epsilon'}}{2\pi \epsilon_t''} \quad (1.19)$$

Another simplification can be done in Equation 1.18. Depending on the dominate losses, two cases can be investigated:

- If the conduction losses dominate ($\epsilon'' \ll \frac{\sigma_e}{\omega}$), which corresponds to the skin depth approximation, the depth becomes:

$$D_p = \frac{2}{\sigma_e} \sqrt{\frac{\epsilon'}{\mu'}} \quad (1.20)$$

This expression explains the reflection of the electric field \mathbf{E} by metal materials: the penetration depth tends to zero when the electric conductivity σ_e is high.

- If the dielectric losses dominate ($\epsilon'' \gg \frac{\sigma_e}{\omega}$), Equation 1.18 becomes:

$$D_p = \frac{\lambda_0}{\pi \sqrt{\epsilon_r}} \frac{1}{\tan \delta} \quad (1.21)$$

In the case of low-loss insulating materials, this distance can be in the order of a centimetre. This centimetric value is close to the dimensions of the heated samples, and explains why microwave heating is often referred to as volume heating.

1.3.3 Direct versus hybrid microwave heating

Depending on the dielectric properties of the material, three types of behaviour can be distinguished at a given temperature, to describe the electric field - material interaction (see Figure 1.15):

- Opaque behaviour: the wave is totally reflected and does not penetrate into the material. A material with this behaviour is characterised by a high electric conductivity ($\sigma_e > 10^3 \text{ S.m}^{-1}$) and a penetration depth under 2.45 GHz microwaves excitation of the order of a micrometre [110, 49, 15, 39]. This is the case of conductive materials such as Silver (Ag) and Copper (Cu).
- Transparent behaviour: the wave penetrates the material without losing energy, *i.e.* is fully transmitted. A material with this behaviour is characterised, at the considered temperature, by a low electric conductivity ($\sigma_e < 10^{-4} \text{ S.m}^{-1}$), a loss factor lower than 0.01 [15], and a penetration depth under 2.45 GHz microwaves excitation of more than ten meters [39]. These materials are generally insulators at room temperature, such as Alumina (Al_2O_3) and Silica (SiO_2).
- Absorption behaviour: the wave is sufficiently absorbed by the material so that a part of its energy is dissipated as heat. A material with the behaviour is characterized by an electric conductivity $10^{-5} < \sigma_e < 10^2 \text{ S.m}^{-1}$, high dielectric losses with a loss factor greater than 0.1 [15]) and a penetration depth under 3 GHz microwaves excitation of the order of a centimetre [88]. This is the case of materials such as silicon carbide (SiC) and Zinc Oxide (ZnO).

To achieve microwave heating, the materials must be absorbent and dissipate sufficient energy. However, as mentioned above, this classification must be qualified because the dielectric parameters change with temperature. The energy absorption and dissipation capacity of the material can, above a certain temperature, increase sharply. These materials therefore suddenly become very absorbent and heat up quickly. This is particularly the case for zirconia, which is transparent at room temperature and whose properties increase rapidly after 500°C [26].

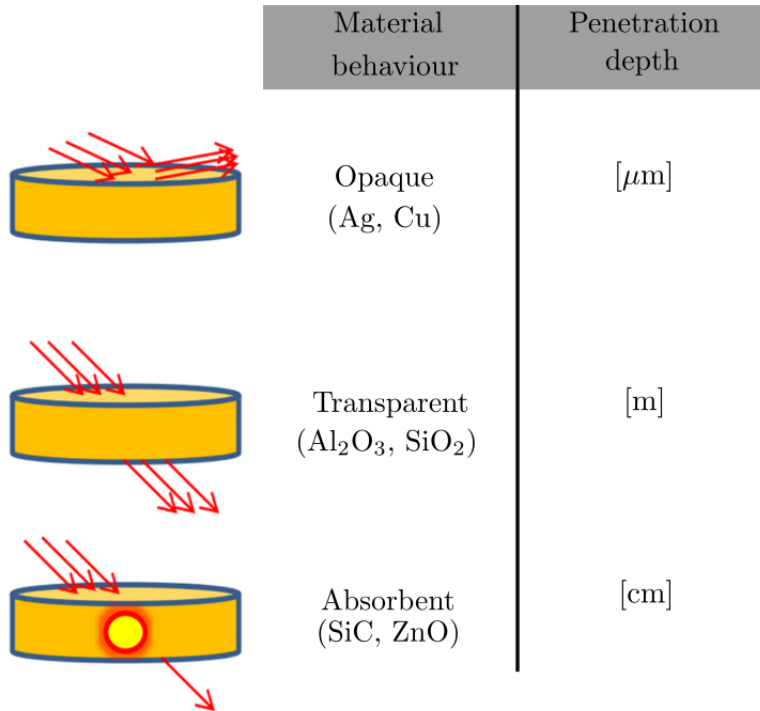


FIGURE 1.15 – Microwave - material interaction.

In this work, we are interested with heating/sintering alumina and silicon carbide which are respectively relatively transparent and absorbent materials. Figure 1.16 presents the evolution of the imaginary part of the relative dielectric permittivity with respect to the temperature for silicon carbide and alumina materials. These values are taken from literature [11, 56], and presented in polynominal form in Appendix C. The dielectric losses of the SiC is higher than that of Al₂O₃ for the range temperature 293K-1873K. The difference become higher after 1400K due to the contribution of the electrical conductivity.

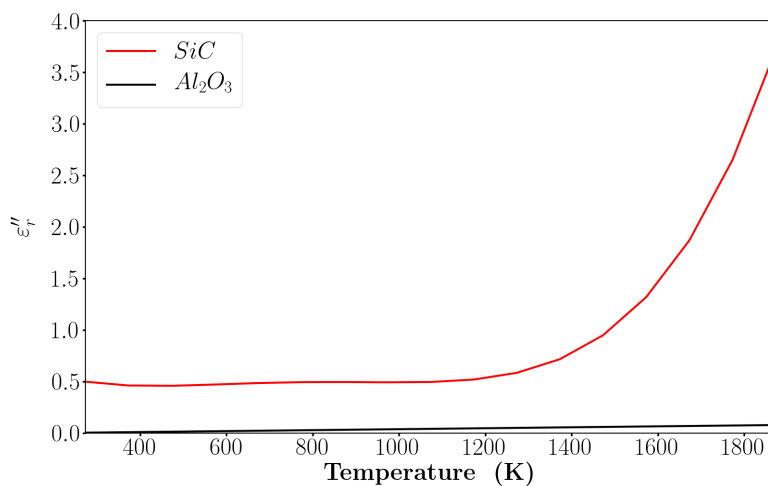


FIGURE 1.16 – Imaginary part of the dielectric permittivity versus temperature for silicon carbide and alumina materials [11, 56].

Figure 1.17 shows the difference between direct and hybrid (indirect) microwave heating. In fact for direct heating, only absorbent materials can couple directly with the electromagnetic field. Here the sample itself is the heat source (Figure 1.17 a)). However, for materials with low dielectric loss at least at room temperature (such as alumina), a hybrid configuration using a heating element named "susceptor", which is made of absorbent material (generally in SiC), will be used. The susceptor is used to initiate the process, heating the sample by infrared radiation (Figure 1.17 b)).

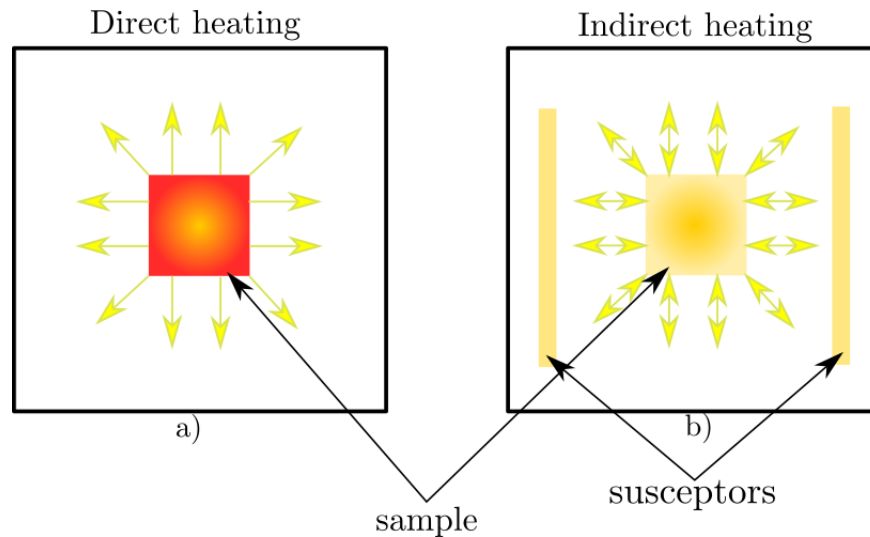


FIGURE 1.17 – Microwave heating: a) direct vs b) indirect.

Alford *et al* [6] study the effect of a susceptor for heating Si wafers and how the susceptor initiates the microwave heating. Figure 1.18 shows the evolution over time of the temperature at the Si surface for direct and hybrid microwave heating. The maximum of the temperature in direct heating is around 100°C, while in the hybrid configuration, the temperature reaches more than 700°C in less than 100 seconds.

Whatever the configuration (direct / hybrid) used, the sample is placed inside a cavity. However, microwave heating equipment are not only cavities, but also generators and waveguides. All these equipments are detailed in the next section.

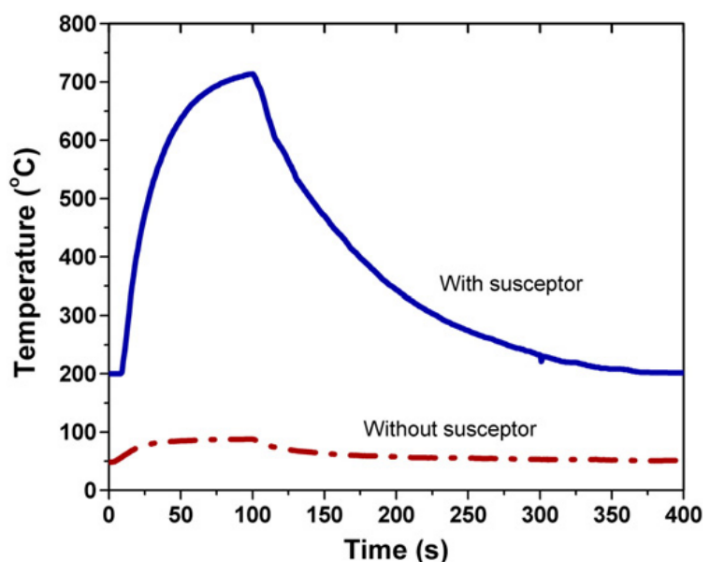


FIGURE 1.18 – Surface temperature versus time during direct (without susceptor) and hybrid (with susceptor) microwave heating [6].

1.4 Microwave heating equipment

1.4.1 Microwave generators

A generator is a source of microwaves. Depending on the application [25], several microwave generators can be distinguished:

- Magnetrons: generally used for frequencies between 1 and 30 GHz. Because of its low cost, this type of generator is the most used for microwaves.
- Klystrons: used for frequencies between 0.3 and 100 GHz. Because of their high price, their use is limited to modern radar and particle accelerators.
- Gyrotrons: used for frequencies between 30 and 300 GHz. They are characterized by high power up to 1 MW. This type of generator is used in nuclear fusion experiments in order to create plasma.
- Solid state generators: they consist of semiconductors (transistors) that emit a more precise frequency spectrum than that emitted by magnetrons.

Both solid state and magnetron generators will be used in this work. In order to clearly understand the difference between these two generators, a comparison in frequency distribution is presented in Figure 1.19. For magnetron generator, the frequency ranges from 2.25 GHz to 2.6 GHz, whereas, for solid state generator, the frequency is more precise with range of 2.45 ± 0.0025 GHz. Moreover a semiconductor generator has a compact size. Hence for the same power supply of 1 kW, the weight of a magnetron generator is 6 Kg, whereas it is 0.5 kg for a solid state generator. Figure 1.20 shows how a semiconductor generator is smaller compared to a magnetron generator. In addition to frequency distribution, size of generators, other comparisons are presented in Table 1.1. For example the lifetime of a magnetron generator (500 - 1000 hours) is very short compared to the solid state one (20 years). Note that the applied power for magnetron generator is from 30 W to kW, whereas this power is in the order of 3 kW.

1.4. Microwave heating equipment

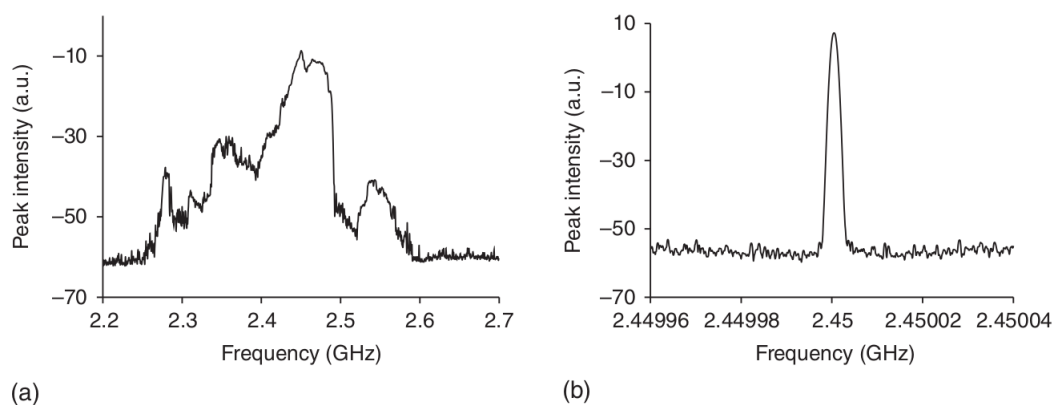


FIGURE 1.19 – Frequency spectral distribution of 2.45 GHz microwave radiation for a) magnetron generator and b) solid state (semi conductor) generator [45].

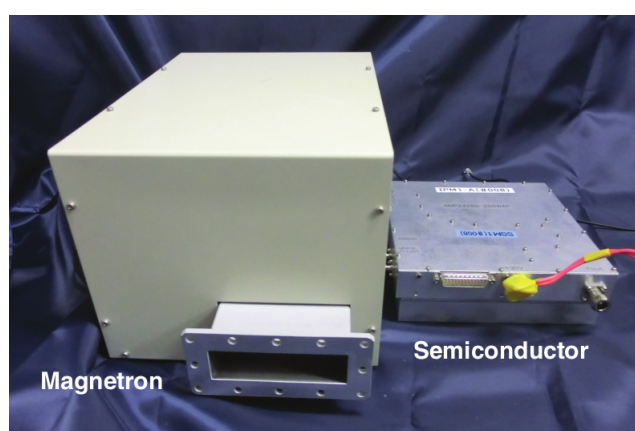


FIGURE 1.20 – Magnetron (left) and solid state (right) generators [45].

TABLE 1.1 – Relative comparison of magnetron and solid state generator characteristics [44].

	Magnetron generator	Solid State generator
Applied power	30 W to kW	~ 3 kW
Weight of the power supply	6 kg (for 1 kW)	0.5 kg (for 1 kW)
Applied voltage	1 kV (for 1 kW)	0.05 kV (for 1 kW)
Electric power conversion efficiency	70-80%	50-70%
Frequency control	No	Yes
lifetime	500-1000 h	20 years
Use environment	Weak in vibration	Weak for high temperature and reflected microwaves

1.4.2 Guided propagation

Waveguides are metal structures, allowing the conduction of the electromagnetic waves from the generator to the cavity in which the sample to be heated/sintered is placed. They can have several geometries: cylindrical, elliptical and rectangular. An air-filled rectangular waveguide will be used in the rest of this study.

Depending on the nature of the field perpendicular to the direction of propagation z , two basic modes of propagation can be distinguished (Figure 1.21):

- The transverse electric wave (TE): the electric field \mathbf{E} is perpendicular to the direction of propagation z , i.e. $E_z = 0$. The magnetic field \mathbf{H} is then in the plane perpendicular to \mathbf{E} , $H_z \neq 0$.
- The transverse magnetic wave (TM): the magnetic field \mathbf{H} is perpendicular to the direction of propagation z , i.e. $H_z = 0$. The electric field \mathbf{E} is in the plane perpendicular to \mathbf{H} , $E_z \neq 0$.

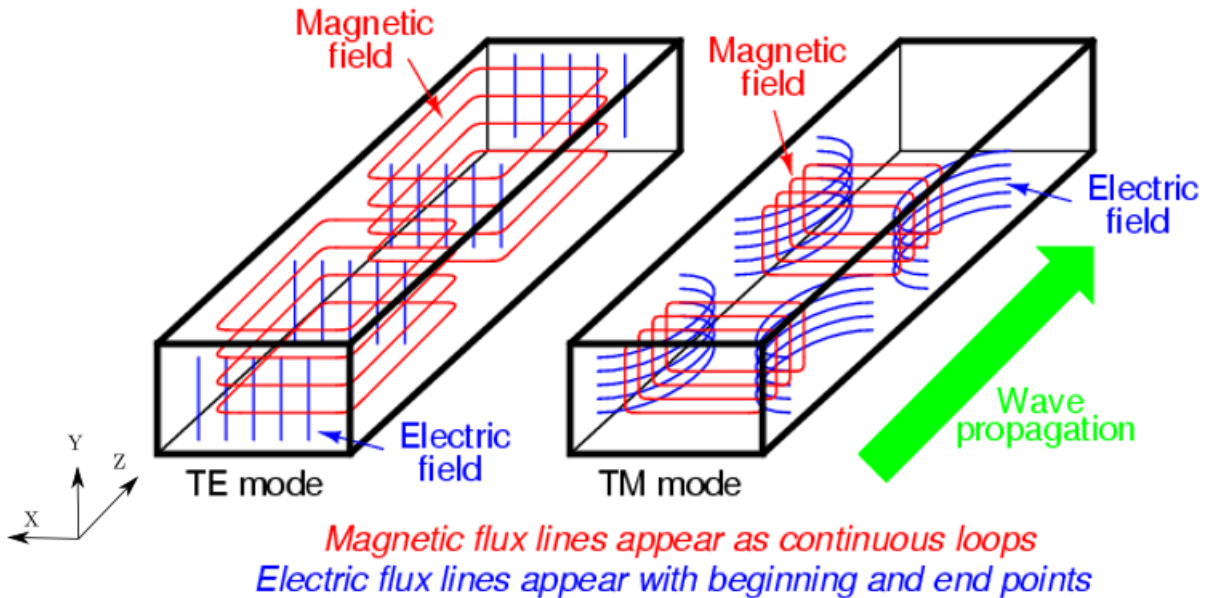


FIGURE 1.21 – Microwave distribution in rectangular waveguide for a transverse electric mode (TE) and a transverse magnetic mode (TM) [102].

For TE (resp. TM) waves, the electric (resp magnetic) field can have different configurations. Each field configuration, also called mode, is identified by two indexes m and n which indicate the number of maxima and minima in the x and y directions respectively. Figure 1.22 presents different modes for TE and TM waves.

Depending on the frequency and wanted modes, the size of the waveguide changes. Figure 1.23 a) shows three cavities with three different sizes corresponding, respectively, to frequencies of 915 MHz, 2.45 GHz and 5.8 GHz from the left to the right.

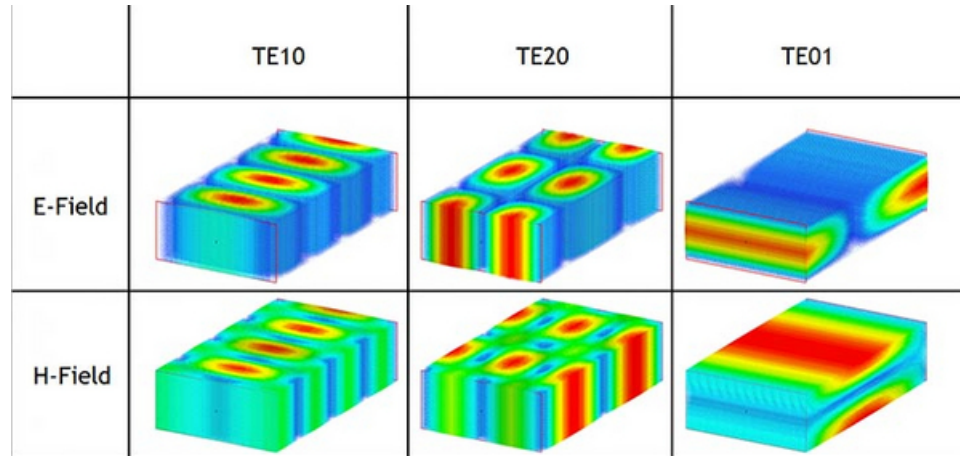


FIGURE 1.22 – E-Field and H-Field distributions in different modes in rectangular waveguides [30].

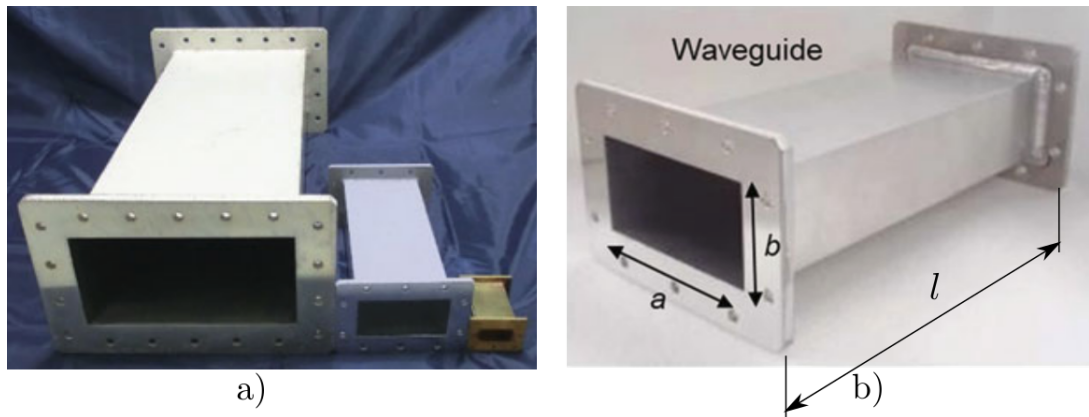


FIGURE 1.23 – Waveguide size: a) photograph of the different size of waveguides used for 915 MHz, 2.45 GHz and 5.8 GHz (from left to right) b) WR340 waveguide with dimensions [44].

A rectangular waveguide excited at 2.45 GHz with TE₁₀ mode will be used in this work. It corresponds to a WR340 waveguide with a rectangular section of dimension $a = 86.36$ mm and $b = 43.18$ mm [107] as shown in Figure 1.23 b). The wavelength corresponding to the frequency 2.45 GHz is 12.24 cm. However, the wavelength of the microwaves change inside the cavity. The new wavelength is called the guide wavelength λ_g and is given by [44]:

$$\lambda_g = \frac{\lambda}{\sqrt{1 - \left(\frac{\lambda_0}{2a}\right)^2}} \quad (1.22)$$

Depending on the geometry of the guide and the frequency used, there is a wavelength, called the cut-off wavelength λ_c , from which the waves cannot propagate in the waveguide. For a rectangular waveguide, the cut-off wavelength is given by:

$$\lambda_c = \frac{2}{\sqrt{\left(\frac{n}{a}\right)^2 + \left(\frac{m}{b}\right)^2}} \quad (1.23)$$

The relationship between the free space wavelength λ_0 , the guided wavelength λ_g and the cut-off wavelength λ_c is [65]:

$$\left(\frac{1}{\lambda_0}\right)^2 = \left(\frac{1}{\lambda_c}\right)^2 + \left(\frac{1}{\lambda_g}\right)^2 \quad (1.24)$$

1.4.3 Microwave cavities

The electromagnetic wave is transferred from the generator, passing through the waveguide, until arriving to the cavity where a sample is placed. Inside the cavity, the sample interacts with microwaves. Metal walls keep the microwave radiation inside the cavity.

Two types of cavities can be distinguished: single mode cavities where a single standing wave pattern is generated and multimode mode cavities in which a large number of resonant modes is supported.

- Single mode (called also mono-mode) cavity: this type of cavity is used for sintering/heating small samples (generally for fundamental research domain) for materials having medium or high dielectric losses (such as SiC). The geometry of this kind of cavity is designed to support only one resonant mode according to the Maxwell equations 1.1-1.4. Theoretically, the electromagnetic field distribution can be known in advance in order to place the product in a maximum of electric field. However, when a sample is placed in the single-mode cavity, this latter interacts with microwaves and the stationary wave (the incident and reflected waves are in phase) is perturbed (see Chapter 3). That's why shifting a short-circuit piston (short plunger), is necessary to keep the sample in a maximum of electric field (Figure 1.24). Since the electric permittivity changes with the temperature, this tuning must be performed all along the heating.

In this work, where a rectangular cavity excited at 2.45 GHz is used, the mode equation for the length of a perfect and empty cavity can be deduced from the expression of the resonant frequency ω_{nmp} (corresponding to a stationary wave):

$$\omega_{nmp} = c\sqrt{\left(\frac{n\pi}{a}\right)^2 + \left(\frac{m\pi}{b}\right)^2 + \left(\frac{p\pi}{l}\right)^2} \quad (1.25)$$

where c is the speed of light in vacuum, n , m , p are the mode coefficients, and a , b and l are the dimensions of the cavity (Figure 1.23 b)).

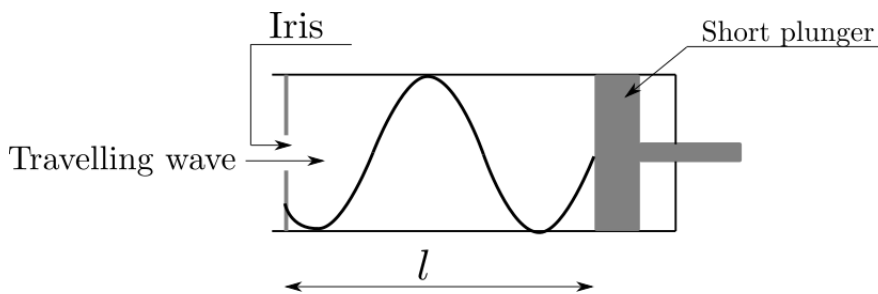


FIGURE 1.24 – Single mode cavity.

- Multimode cavity: this cavity is used for heating (or sintering) larger pieces. This is the domestic microwave ovens. Such cavity are used in both fundamental research and industry applications. For example, the Opti'waves startup works on the sintering of dental prosthesis made in zirconia with multimode cavities [78]. The multimode cavity is characterised by the propagation of waves in all directions of space, reflecting off the metal walls, thus leading to the superposition of incident and reflected waves in multiple modes. Although standing waves can be formed, the distribution of the field is inhomogeneous in the cavity. Figure 1.25 a) shows the distribution of the electric field intensity inside a multimode cavity obtained by simulation. To homogenize the heating (or, equivalently, the electric field distribution), a mixing paddle is used (Figure 1.25 b)).

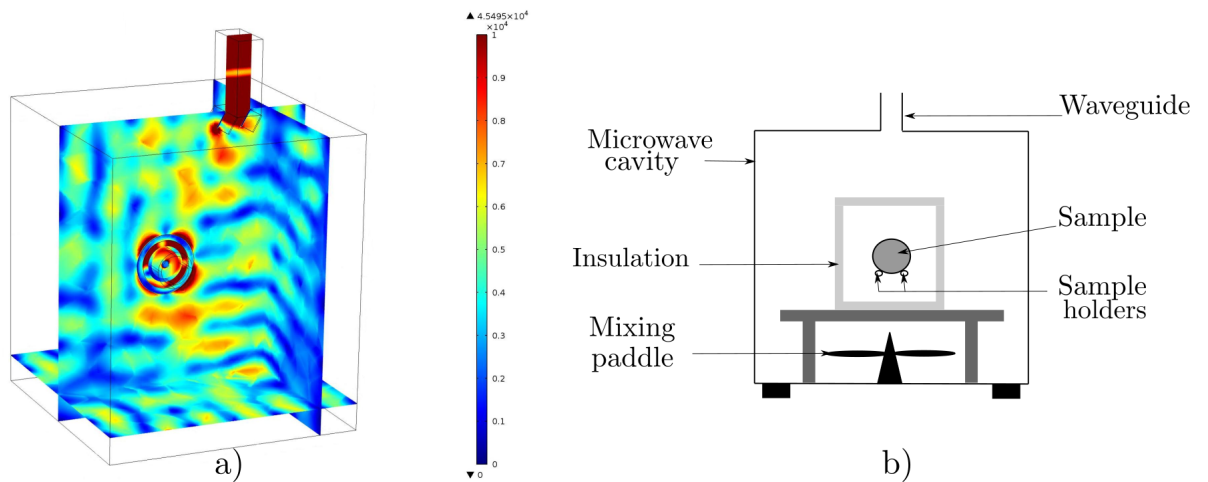


FIGURE 1.25 – Multimode cavity: a) electric field distribution inside the charged multimode cavity [26], b) schematic view of a multimode cavity.

Since only one mode of propagation is present in a single-mode cavity, this kind of cavity is more suitable for studying the electromagnetic field - material interaction, and for this reason is used in this work. Many difficulties arise in this context, such as how to place and to maintain the sample in a maximum of electric field, or how to monitor the temperature during the process. These key points are presented in the next Chapters.

1.5 Materials

In this work, we are interested to heat SiC and to sinter Al_2O_3 in single mode cavity excited to 2.45 GHz. These two materials are briefly presented below.

1.5.1 Alumina

Alumina, or aluminium oxide, is a compound of two atoms of aluminium Al (black circle in Figure 1.26) and three atoms oxygen O (blue circle in Figure 1.26), with a chemical formula Al_2O_3 . It is the most commonly used oxide in ceramics. Comparing to other ceramics, alumina has advantages such as hard wear-resistant, low thermal conductivity ($39 \text{ W}\cdot\text{m}^{-1}\cdot\text{K}^{-1}$), good electric insulation with electric strength $35 \text{ kV}\cdot\text{mm}^{-1}$ and a resistivity of

$10^{12} \Omega \cdot \text{m}$ at 20°C . These advantages make it possible to use alumina in many industrial applications such as firebrick, abrasives and integrated circuit (IC) packages [98]. Alumina can exist from four defined forms: gibbsite, boehmite, bayerite and diaspore. The most used alumina is produced through the Bayer process, which consists in the dissolution of the alumina contained in the bauxite by means of caustic soda to precipitate the alumina hydrate. The alumina hydrate thus obtained is then calcined.

Figure 1.27 shows the four paths of alumina during heating treatment process, starting from the four different forms (gibbsite, boehmite, bayerite and diaspore), passing by different crystalline phases (χ , κ , γ , δ , θ , η) to arrive to the most stable one, the α phase, which is obtained by calcination.

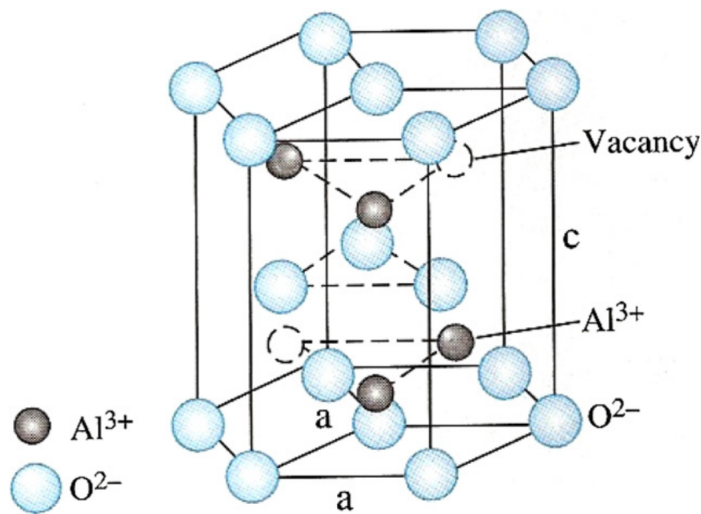


FIGURE 1.26 – α -alumina structure: blue circles represent the O^{2-} anions, small black circles represent Al^{3+} cations and small empty circles vacant octahedral interstices [28].

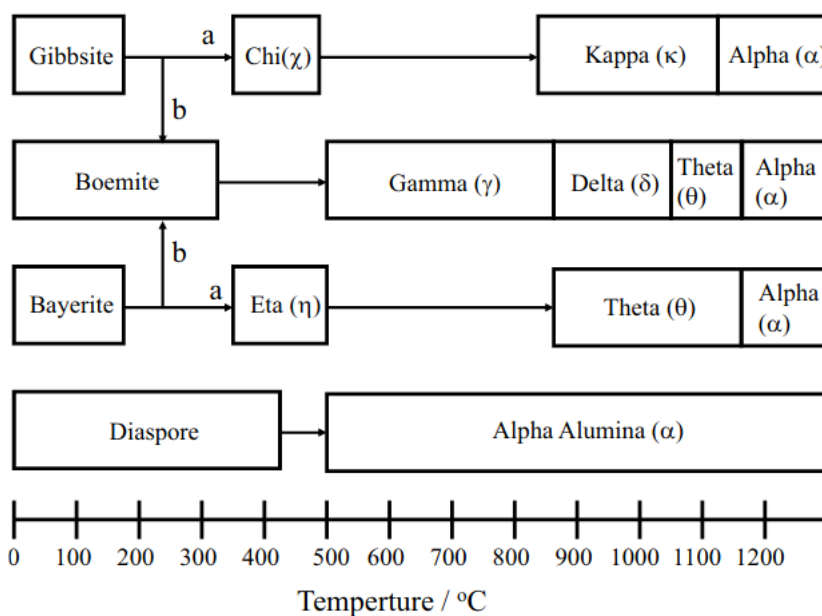


FIGURE 1.27 – Structure transformation of alumina [98].

In this work, we used α -alumina whose structure is described by a hexagonal mesh with parameters (lattice dimensions and angles):

$$a = 4.759 \text{ \AA}, c = 12.991 \text{ \AA}, \alpha = \beta = 90^\circ \text{ and } \gamma = 120^\circ$$

As said before, for alumina material, the relative permittivity parameters is low at ambient temperature (see Appendix C). The use of microwave sintering of alumina requires the use of susceptor to initiate the heating. The susceptor is generally in Silicon Carbide (SiC).

1.5.2 Silicon Carbide

Silicon Carbide is a compound of Silicon Si (yellow spheres in Figure 1.28) and carbon C (black spheres in Figure 1.28), with a chemical formula SiC. Several interesting properties can be noticed, as a high thermal conductivity ($350 \text{ W}\cdot\text{m}^{-1}\cdot\text{K}^{-1}$), high hardness, good resistance to thermal shock and very high melting point [69], which make it possible to use SiC in electronic components such as light emitting diodes, in vehicle equipment such as brake discs, or as cutting tools.

The silicon carbide can exist in different structures, including crystalline structures called polytypes. They consist in layers of the same chemical compound, identical in two dimensions, but stacked in different sequences. The atoms of those layers can be arranged in three configurations A, B, C to achieve closest packing as described in Figure 1.28.

Silicon carbide occurs in different stacking sequences, and each unique one can generate a different polytype, for example Cubic (C), Hexagonal (H) and Rhombohedral (R). Depending on the structure, two categories of SiC exist: Beta β -SiC for cubic structure and alpha α -SiC for hexagonal and rhombohedral structures. Alpha Silicon carbide (α -SiC) is stable for high temperatures (higher than 1700°C), contrary to the Beta silicon carbide (β -SiC) which is formed at temperatures below 1700°C [1].

To date, more than 200 SiC polytypes are known [64]. However, the most common polytypes are 3C, 4H and 6H (the number here refers to the number of layers). Figure 1.28 shows the stacking sequences of the crystal structure of 3C-SiC, 4H-SiC and 6H-SiC. For 3C-SiC, the stacking sequence is ABC/ABC. For hexagonal structures, stacking sequences are ABCB/ABCB and ABCACB/ABCACB for 4H-SiC and 6H-SiC respectively.

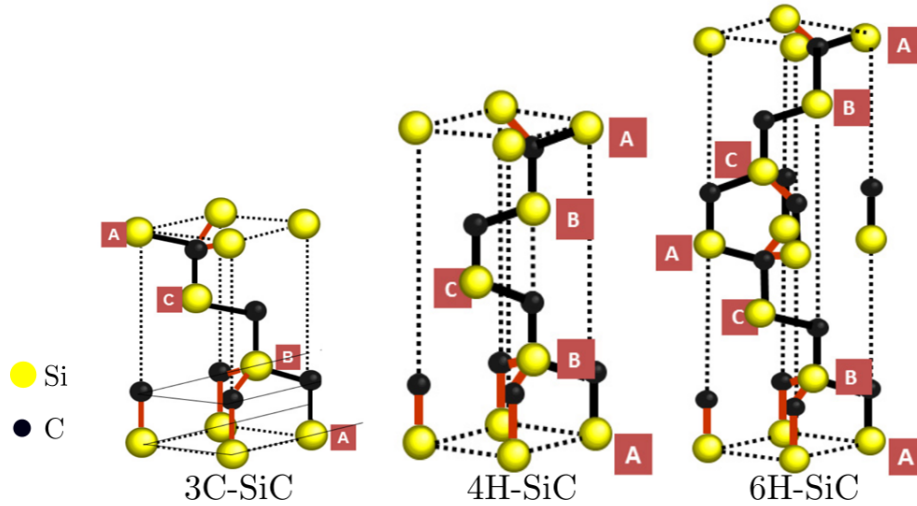


FIGURE 1.28 – Stacking sequences of the crystal structure of 3C-SiC, 4H-SiC and 6H-SiC. The chain structures that define the stacking sequence are in dark color while selected Si-C bonds are in red color [64].

Moissanite is the natural form of silicon carbide. This very rare mineral on Earth, consists mainly of SiC polytype 6H, or α -SiC, although other polymorphs are also present. However, the most encountered SiC is thus man made, using Acheson process, where under a graphite electric resistance furnace, a mixture reaction between silica and coke leads to the formation of Silicon Carbide. This reaction is presented by the equation [31]:



1.6 Conclusion

This introduction chapter has first presented the different stages of the sintering process and the associated diffusion paths. Traditionally, sintering of ceramics is carried out in conventional furnace. However, in last decades, new technologies have been developed. Among them, microwave sintering, that interests us in this work. In order to model and simulate this process, physics of electromagnetic wave propagation (Maxwell's equations), and constitutive laws describing the wave - material interaction, have been introduced. When focusing on ceramics, as in this work, the dielectric permittivity ϵ^* is the key parameter which controls the heating of the material by microwaves. Depending on the value of the dielectric permittivity at ambient or low temperature, two configurations of microwave heating are considered: direct heating which will be study in Chapters 3 and 4, and hybrid heating which will be study in Chapter 5.

The microwave heating system is composed of a generator, a waveguide and a cavity. All these equipments were presented in the fourth section of this chapter. In this work, we are interest to heat/sinter a sample in a single mode cavity. In order to have an efficient heating, it is essential to place the material in a maximum of the electric field. However, the heated material interacts with microwaves and then perturbe the electric field. To keep the sample in a maximum of the electric field, it is necessary to vary the dimensions of the waveguide by shifting a short-circuit piston. The sample used in this work is made

1.6. Conclusion

of silicon carbide in Chapter 3 and alumina in Chapter 4. Consequently, a short description of these materials was presented in the last section of this chapter.

Résumé en Français :

Ce chapitre d'introduction a d'abord présenté les différentes étapes du processus de frittage et les chemins de diffusion associées. Traditionnellement, le frittage des céramiques est effectué dans un four conventionnel. Cependant, au cours des dernières décennies, de nouvelles technologies ont été développées. Parmi elles, le frittage par micro-ondes, qui nous intéresse dans ce travail. Afin de modéliser et de simuler ce processus, la physique de la propagation des ondes électromagnétiques (équations de Maxwell) et les lois constitutives décrivant l'interaction onde - matériau ont été introduites. Lorsqu'on se concentre sur les céramiques, comme dans ce travail, la permittivité diélectrique ϵ^* est le paramètre clé pour comprendre cette interaction et comment le matériau peut être chauffé par les micro-ondes. En fonction de la valeur de la permittivité diélectrique à température ambiante ou basse, deux configurations de chauffage par micro-ondes sont envisagées : le chauffage direct qui sera étudié dans les Chapitres 3 et 4, et le chauffage hybride qui sera étudié dans le Chapitre 5.

Le système de chauffage par micro-ondes est composé d'un générateur, d'un guide d'ondes et d'une cavité. Tous ces équipements ont été présentés dans la quatrième section de ce Chapitre. Dans ce travail, nous nous intéressons au chauffage/frittage d'un échantillon dans une cavité monomode. Afin d'avoir un chauffage efficace, il est essentiel de placer le matériau dans un maximum du champ électrique. Cependant, le matériau chauffé interagit avec les micro-ondes et perturbe alors le champ électrique. Pour maintenir l'échantillon dans un maximum de champ électrique, il est nécessaire de faire varier les dimensions du guide d'onde en déplaçant un piston court-circuit. L'échantillon utilisé dans ce travail est constitué de carbure de silicone dans le Chapitre 3 et d'alumine dans le Chapitre 4. Par conséquent, une brève description de ces matériaux a été présentée dans la dernière section de ce chapitre.

Chapter 2

Method

Contents

2.1 Introduction	38
2.2 Experimental procedure	38
2.2.1 Temperature measurement	38
2.2.2 Emissivity measurement	42
2.2.3 Microwave set-up	46
2.3 Numerical procedure	48
2.3.1 Modelling of microwave heating and sintering	48
2.3.2 Computational domain and boundary conditions	53
2.3.3 Mesh sensibility analysis	54
2.4 Conclusion	56

2.1 Introduction

This chapter details the experimental procedure and the numerical set-up used in the following chapters of this PhD work to study the microwave heating of SiC (Chapter 3) and Al₂O₃ (Chapter 4) samples.

2.2 Experimental procedure

2.2.1 Temperature measurement

2.2.1.1 Thermocouple

A thermocouple is a device measuring the temperature, composed of two electrical conductors (A and B in Figure 2.1) forming an electrical junction at T_1 (hot connection) and insulated from each other. The second extremity T_2 (cold connection) of each conductor is kept at constant reference temperature. Due to the Seebeck effect [43], the thermocouple generates a potential difference proportional to the gradient of temperature between T_2 and T_1 . Hence, temperature T_1 can be determined, provided T_2 is known.

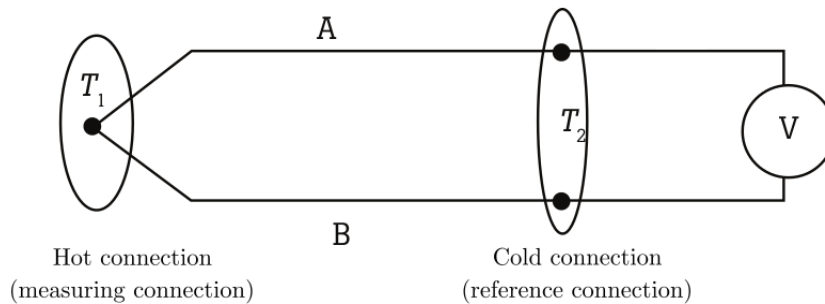


FIGURE 2.1 – Working principle of a thermocouple [103].

There are different types of thermocouples, each corresponding to different temperature ranges. Their properties may also depend on the type of insulation used for the wires. According to international norm [8, 96], thermocouples can be classified in:

- **Base Metal Thermocouples:** these thermocouples are composed of common, inexpensive metals as nickel, iron and copper. Table 2.1 gives temperature ranges of some of these thermocouples, called of types E, J, K, N, T.

TABLE 2.1 – Base Metal Thermocouples temperature ranges [96].

Type	Temperature ranges
E	-200°C to 900°C
J	0°C to 750°C
K	-200°C to 1250°C
N	-270°C to 1300°C
T	-200°C to 350°C

- Noble Metal Thermocouples: as mentioned in the denomination, these thermocouples are made of noble metal wire (platinum, rhodium) [96]. They include R, S, B types, the temperature ranges of which are presented in Table 2.2.

TABLE 2.2 – Noble Metal Thermocouples temperature ranges [96].

Type	Temperature ranges
R	0°C to 1450°C
S	0°C to 1450°C
B	0°C to 1700°C

As shown in Table 2.2, the temperature ranges of thermocouples type R and S are the same. However, the difference between these two types is in the percentage of rhodium.

- Refractory Metal Thermocouples: the wire of this kind is made from the exotic metals tungsten and rhenium. These metals are expensive, difficult to manufacture. Wire made with these metals are very brittle. This kind of thermocouples includes type C, with a temperature range of 0°C to 2320°C.

In this work, two types of thermocouples will be used: type K for the emissivity measurement (see Section 2.2.2), where the maximum temperature considered is 900°C, and type B for the dilatometry (see Section 4.2.1), with a maximum of temperature of 1600°C.

2.2.1.2 Pyrometer

Contrary to the thermocouple measurement, pyrometry is a non-contact temperature measurement technique. It allows non-contact determination of the temperature at a distance of a few centimetres from the surface. This measuring device is important for our study because it allows measurement by avoiding metal- microwave interactions. Its working principle will be detailed in the following.

First of all, it is important to define the concept of black body. A black body is an object which absorbs all incident radiation regardless of its wavelength and angle of incidence and re-emits all of its energy at all wavelengths. The spectral distribution of the energy emitted by a black body heated to a temperature T is defined by the Planck's law [60]:

$$L_{\lambda}^{cn}(T) = \frac{C_1 \lambda^{-5}}{e^{\frac{C_2}{\lambda T}} - 1} \quad (2.1)$$

where L_{λ}^{cn} is the spectral luminance at the wavelength λ of a black body ($\text{W.m}^{-3}.\text{sr}^{-1}$), $C_1 = 2hc^2 = 1.19 \times 10^{-16}$ ($\text{W.m}^{-3}.\text{sr}^{-1}$) and $C_2 = \frac{hc}{k} \times 1.44 \times 10$ (m.K) are two constants, h is the Planck constant, k is the Boltzmann constant, c is the speed of light, λ is the wavelength (μm) and T is the temperature.

Figure 2.2 shows the spectral luminance of a black body for different temperatures. For each temperature there is a maximum at a given wavelength λ_{max} , which shifts to shorter wavelengths as the temperature rises. This shift of the maximum emission peak

as a function of temperature is generalized by Wien's law [60]:

$$\lambda_{max} = \frac{2898}{T} \quad (2.2)$$

When $C_2 / \lambda T \gg 1$, Planck's relation can be approximated by Wien's relation:

$$L_{\lambda}^{cn}(T) = C_1 \lambda^{-5} e^{-\frac{C_2}{\lambda T}} \quad (2.3)$$

These laws are only valid in the case of a black body. However, the majority of real objects re-emit some incident radiation. To describe this amount of radiation, we introduce the emissivity, noted ϵ_{λ} . This quantity is defined as the ratio of the luminance of an object at the temperature T and the luminance emitted by the black body at the same temperature for a given wavelength [14]:

$$\epsilon_{\lambda} = \frac{L_{\lambda}(T)}{L_{\lambda}^{cn}(T)} \quad (2.4)$$

The value of the emissivity is then between 0 and 1, and depends on the surface state [51] of the material as well as the temperature. Therefore the knowledge of emissivity is essential and requires a calibration, as described in Section 2.2.2.

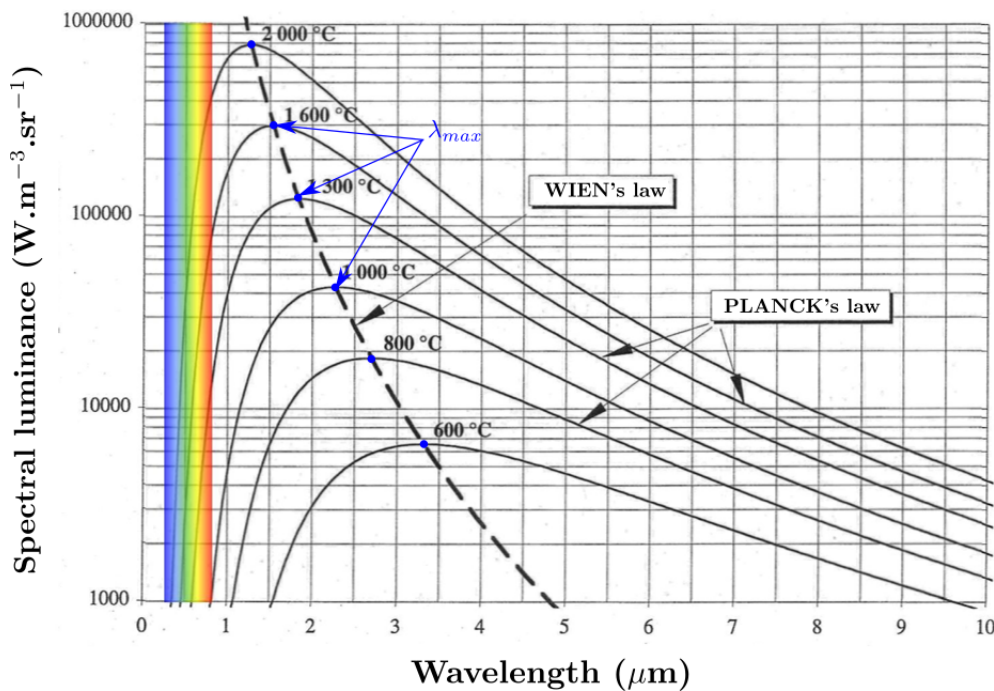


FIGURE 2.2 – Spectral luminance as function of the wavelength for a black body, at different temperatures [26].

There are several types of pyrometers, the most common being the following.

- Monochromatic pyrometers: they measure the luminous flux (luminance) emitted by an object at a single wavelength and use the laws of thermal radiation to deduce the temperature T . Using Wien's approximation (Equation (2.3)), the temperature

T is given by:

$$\frac{1}{T_\lambda} - \frac{1}{T} = -\frac{\lambda}{C_2} \ln(\epsilon_\lambda) \quad (2.5)$$

where T_λ is the black body temperature at the wavelength λ and ϵ_λ is the light source emissivity.

The advantage of this type of pyrometer is that the emissivity of the material only needs to be known for the pyrometer wavelength.

- Bichromatic pyrometers: they measure the luminous flux (luminance) emitted by an object at two wavelengths λ_1 and λ_2 . As for the monochromatic pyrometer, the expression of the temperature T is based on Wien's approximation (Equation (2.3)) but the measurement is made from the ratio of the two luminance at two wavelengths λ_1 and λ_2 :

$$\frac{1}{T_\lambda} - \frac{1}{T} = -\frac{\lambda_1 \lambda_2}{C_2(\lambda_1 - \lambda_2)} \left(\frac{\epsilon_{\lambda_1}}{\epsilon_{\lambda_2}} \right) \quad (2.6)$$

A bichromatic pyrometer generally measures temperatures above 400°C. However, in this work, we are interested in temperatures below this threshold. Consequently, monochromatic pyrometers will be used. The pyrometer Fluke [33] will be used to measure the apparent emissivity and study microwave heating in Chapters 3 and 4. Another monochromatic pyrometer, the IRCON [68] 5G-2024, is employed for the alumina sintering experiments (carried out in collaboration with CRISMAT laboratory, Caen), since in this case the maximum temperature is 1600°C. The wavelength λ , the temperature ranges and the acquisition time of these monochromatic pyrometers are presented in the Table 2.3.

TABLE 2.3 – Characteristics of the monochromatic pyrometers used for the microwave heating and sintering.

Model	λ (μm)	Temperature range ($^\circ\text{C}$)	Acquisition (ms)
Fluke [33] E3ML-F1-V-0-0	2.4	50-1000	20
IRCON [68] 5G-2024	1.6	350-2000	6.6

2.2.1.3 Infrared camera

The infrared camera has the same operating principle as a monochromatic pyrometer. The difference is that for the infrared camera, the light emitted by an object is recorded in the form of a matrix. In this way, the light collected by an optical system on the matrix creates an image of the object and makes it possible to measure a temperature field at the surface. This is an advantage over the pyrometer if the observed phenomenon has spatial gradients. However, as with the pyrometer, the infrared camera requires an emissivity measurement. In Chapter 5, an infrared camera is used to measure the sample and the susceptors temperatures. The characteristics of this camera are presented in Table 2.4.

TABLE 2.4 – Characteristics of the thermal camera used for the microwave sintering.

Model	λ (μm)	Temperature range ($^{\circ}\text{C}$)	Resolution
FLIR [32] A655sc	8.1	300-2000	640 × 480

2.2.2 Emissivity measurement

2.2.2.1 Literature on emissivity measurement

Calibrating the pyrometer requires the measurement of the apparent emissivity. In the literature, various methods are used for this purpose. They can be divided into two types, depending on whether one is working in a microwave furnace or not. In the latter case, a thermocouple can be used, whereas in the former, a calibration material has to be considered.

In microwave furnace, the calibration method, presented in Figure 2.3, involves placing a small amount of calibration material ($\sim 1 \text{ mm}^3$) with a known melting point on a surface of the sample whose apparent emissivity is to be measured. The pyrometer spot is positioned close to the calibration material ($\sim 1\text{-}2 \text{ mm}$). The sample and the calibration material are viewed in real time by a CCD camera placed in a horizontal position to avoid disturbance from heated air. When the calibration material melts, the known temperature is imposed on the pyrometer. Thanks to a dedicated software, this value will be converted into an emissivity value. This emissivity is called apparent, since it takes into account the microwave context.

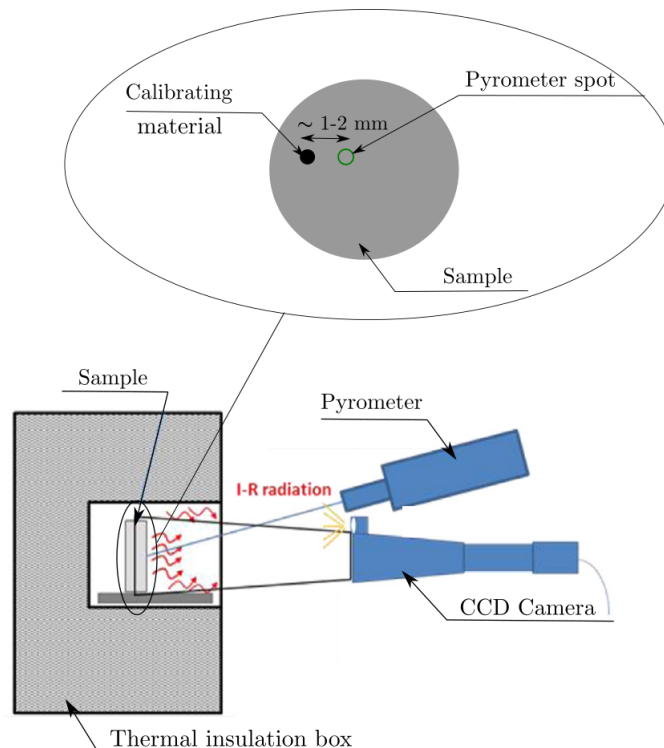


FIGURE 2.3 – Schematic of the pyrometer calibration by fusion of a calibration material [53].

2.2. Experimental procedure

The calibration material must be chosen with care. The melting temperature must be within the temperature range of the sintering process (*i.e.* the temperature at which sintering occurs, typically between 1000 °C and 1550 °C). In addition, the calibration material must be chemically stable within this range. Finally, this method assumes that the calibration material and the sample are at the same temperature. Therefore, they must have the same behaviour under microwave irradiation.

This method was employed by Zymelka *et al* [112], using germanium as a calibration material in the microwave furnace, with a hybrid configuration (see 1.3.3). However, the limitation of this study is that the temperature dependence of the apparent emissivity is not investigated by the authors. To overcome this limitation, Macaigne *et al* [53] developed a new technique consisting in measuring the emissivity of a MgAl_2O_3 sample using four different calibration materials with consequently four different melting points: GeO_2 at 1115 °C, CuO at 1326 °C, FeO at 1377 °C and Nb_2O_5 at 1520 °C.

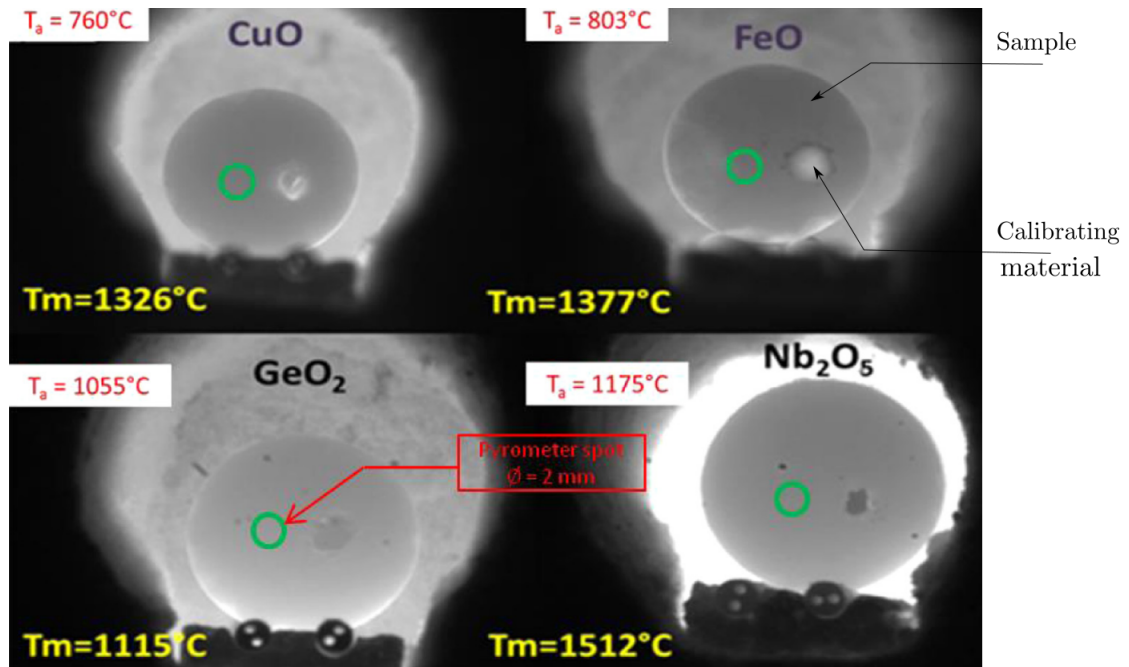


FIGURE 2.4 – Photographs of the sample at T_a (temperature before melting point) with the four different calibration materials [53].

Figure 2.4 shows, for the four calibration materials, a photograph of the sample at a temperature T_a below the melting temperature T_m . In this figure, it can be noted that the sample and the calibration material exhibit different behaviours under microwave irradiation in the CuO and FeO case: these calibration materials glow more than the sample. This means that the temperature of the calibration material is higher than that of the sample, making the calibration not possible. This is because CuO and FeO are both semi-conducting materials and therefore interact more strongly with microwaves.

On the contrary, as shown in Figure 2.4, GeO_2 and Nb_2O_5 present similar absorption to the sample. Thus, the emissivity obtained with these materials, at 1115 °C and 1512 °C, is considered relevant. In reference [53], the emissivity is subsequently assumed to be linear between these two temperatures.

Finally, these temperature values are corrected using Equation (2.7) which describes the temperature dependence of the apparent emissivity, and Wien's approximation (2.5):

$$\frac{1}{T_{cor}} = \frac{1}{T_{mes}} + \frac{\lambda}{C_2} \ln \left(\frac{\epsilon_{cal}}{\epsilon_{exp}} \right) \quad (2.7)$$

where T_{cor} is the corrected temperature, T_{mes} is the measured temperature, λ is the wavelength of the pyrometer, C_2 is the radiation Planck's constant (1.44×10^{-2} [m K]), ϵ_{cal} is the calculated emissivity using the linearisation form and ϵ_{exp} is a fixed emissivity corresponding to emissivity for the high temperature.

In addition to the choice of calibration materials, another difficulty with this approach is that the melting point of the calibration material must be known with accuracy. Moreover, the time at which the material changes state is not easy to determine. This adds uncertainty to the results obtained. To overcome these different issues, a second approach can be found in literature, based on the use of a thermocouple. More precisely, the emissivity value is adjusted to obtain the same temperature with pyrometer as measured with the thermocouple. Note that, unlike the first approach, here the emissivity measurement cannot be performed in a microwave furnace, since the thermocouple interacts with the electromagnetic wave. For example, measures are made in a conventional furnace in [112], or in an electromagnetic induction furnace in [27].

Many studies in the literature are based on this method. Among them, Zymelka *et al* [112] proposes to place the sample in a crucible with a susceptor. However, certain difficulties arising during the heating make it impossible to obtain an accurate value of emissivity, which was found to be equal to 1. The temperature of the pyrometer is then largely overestimated compared to that of the thermocouple. The decision was made to heat the system to 1000°C and then turn off the furnace. The emissivity is evaluated during the subsequent cooling, and the radiation from the furnace resistor is eliminated. Croquesel *et al* [27] also used this technique for the calibration step, but with electromagnetic induction heating. A metal was placed in contact with the sample leading to conductive heating from the metal to the sample. In this case, the temperature measurement is not disturbed by the metal because it is placed under the sample.

To sum up, the two methods presented for determining apparent emissivity have advantages and drawbacks. The first method allows the emissivity to be determined in the environment of interest in our study, the microwave furnace. However, the calibration material must be chosen carefully. Furthermore, the melting point and time increase the uncertainty of the value obtained. With the second method, the emissivity is determined in a non-microwave furnace: the temperature is expected to be more homogeneous, and can be accurately measured with a thermocouple, leading to "confident" values of emissivity. However, this is not the apparent emissivity corresponding to the microwave environment. In this work, the measurement of emissivity will be carried out in a conventional furnace but using a third approach described below, consisting in recovering a black body condition. In this way, it can be expected that the measured emissivity does not depend on the measure environment.

2.2.2.2 Principle of the used calibration technique

The measurement of the emissivity ϵ in this calibration technique, is performed by focusing the infrared pyrometer (Fluke® Process instrument, see Table 2.3) on the sample placed in a conventional furnace under black body conditions [100], and measuring the temperature of the sample using a K-type thermocouple connected to a data acquisition centre, as shown in Figure 2.5a). The pyrometer is connected to the *Data Temp Multidrop DTMD* software with which the emissivity is then determined. More specifically, the sample is positioned in a hollow cylinder of height L , inner diameter d_{int} , satisfying the criterion of the black body condition, $L/d_{int} > 4$. Indeed, according to Sparrow *et al.* [100], such a hollow cylinder can be assimilated to a black body with an accuracy better than 99%. The sample is then placed at the bottom of the cylinder, at a distance d_{focal} (the focal distance) from the pyrometer, see Figure 2.5a). The choice of d_{focal} determines the size of the pyrometer spot, equal to $d_{focal}/100$, and consequently must satisfy $d_{focal}/100 < d_{int}$.

The system (hollow cylinder and sample) is positioned at the centre of a conventional furnace, programmed with a heating rate 5 K/min and a temperature step of 30 minutes for each 100 K from ambient temperature to 1173 K, see Figure 2.5b). The emissivity measurement is limited to 1173 K due to furnace limitations ($T_{max} = 1000^\circ\text{C} = 1273\text{ K}$). The temperature is measured at the surface of the sample at the end of each step, when a convergence between the three values of temperature (furnace, thermocouple, pyrometer) is reached, as shown in Figure 2.5b).

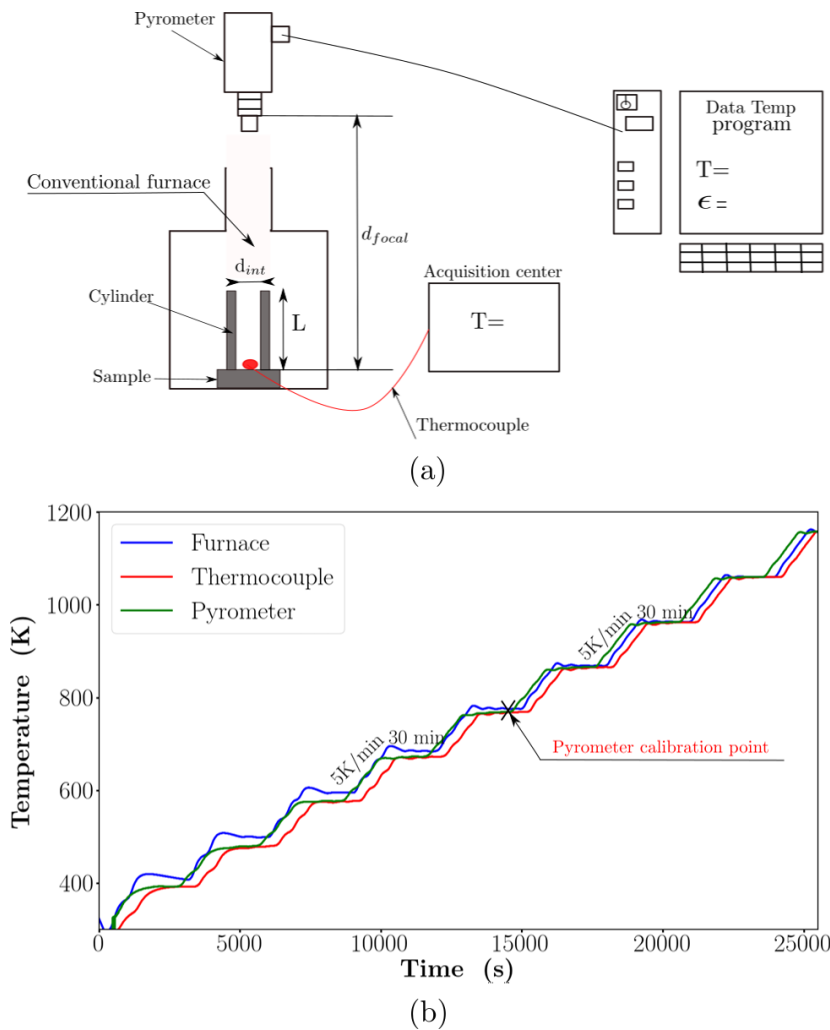


FIGURE 2.5 – Pyrometer calibration: (a) method used [37], (b) thermal cycle.

Finally, note that emissivity is not only required to calibrate the pyrometer, but is also involved in the expression of the radiative flux of the thermal problem, see Equation (2.25).

2.2.3 Microwave set-up

Figure 2.6 presents the single-mode microwave device used to study the microwave heating of SiC and Al₂O₃ samples in Chapters 3 and 4 respectively. This device is composed of a microwave generator (Sairem GMSP10, Solid State) delivering a continuous wave with variable power of up to 900 W at frequencies ranging from 2.4 GHz to 2.5 GHz [92], a WR 340 waveguide, a rectangular cavity bounded on one side by an iris, on the other by a manual short-circuit piston, and having two cylindrical chimneys.

Using a single mode cavity excited at 2.45 GHz, SiC/Al₂O₃ a sample is placed on an insulating support. The thermal insulating used in this study is a commercial material called Altraform® from RATH company [24] (this material is called © RATH in the next). This alumina-silicate fibrous material, composed of 80% alumina and 20% silica, is chosen because it meets all the criteria imposed by the use of high-temperature microwave radiations: low thermal conductivity, good resistance to thermal shock and a high melting point allowing temperatures up to 1800°C. The geometry of this support, presented

2.2. Experimental procedure

in Figure 2.6a), was designed to minimise the contact area with the sample. The © RATH material parameters used in our simulations are given in Appendix C.

As described in Chapter 1, Section 1.4.3, an efficient heating is achieved when the sample (and insulating support) is in a maximum of the electric field. In an ideal, empty waveguide, the electric field is determined by its length l . However, the presence of the system, sample plus support, disturbs the field. In addition, the iris and the chimneys add further perturbations. That is why, prior to any heating, *i.e.* at room temperature, this length l is adjusted by shifting manually the short-circuit piston until the reflected power P_r is minimised, defined as the difference between the incident power and the absorbed power: $P_r = P_{in} - P_{abs}$. Once this resonant length is found, heating can begin, and the temperature is measured through the chimney by the Fluke® calibrated pyrometer, as shown in Figure 2.6b). Of course, the dielectric properties of the sample, as well as those of the support, are temperature dependent. Consequently, the length l of the waveguide should be continuously adjusted during heating to maintain the system in a maximum of the electric field. However, in order to limit the number of parameters that vary during heating, in particular to avoid additional uncertainties when comparing numerical and experimental result, the length of the waveguide is not varied during the heating: it is kept equal to the resonant length found at room temperature.

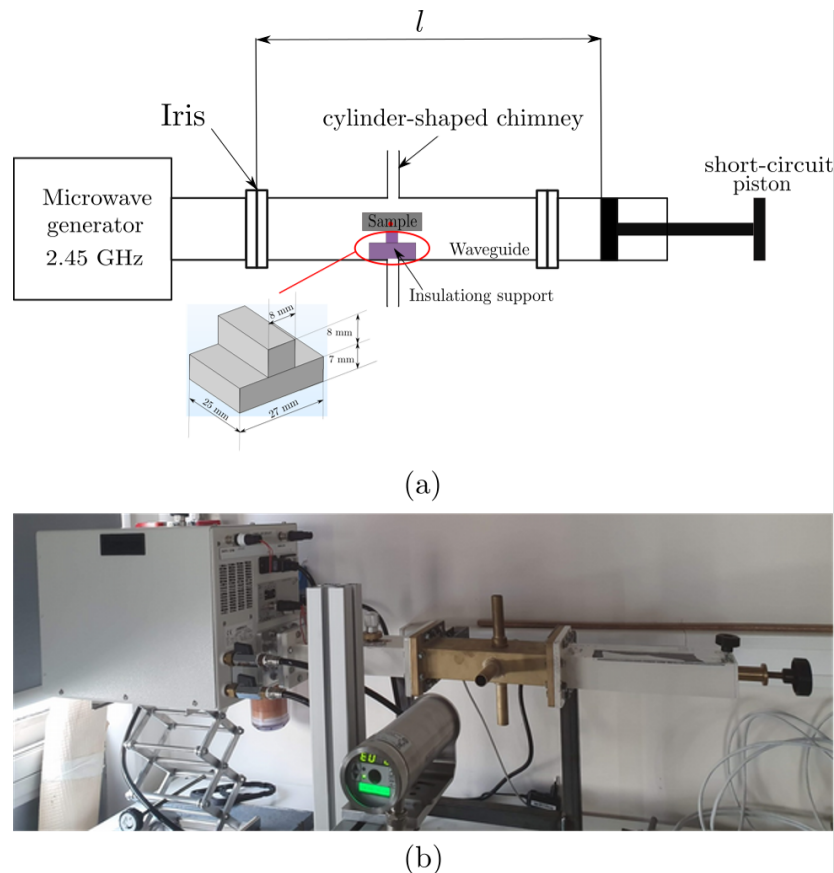


FIGURE 2.6 – Schematics (a) and photograph (b) of single-mode microwave device [37].

The results of the experimental study of microwave heating on SiC and Al₂O₃ will be

presented in Chapters 3 and 4 respectively. The following section introduces the numerical counterpart of the experimental set-up just presented, with a view to performing microwave heating simulations and comparing their results with the experiments.

2.3 Numerical procedure

It was shown in Chapter 1 that the modelling of microwave heating requires the coupling of two “physics”: electromagnetism (Maxwell’s equations) and the thermal problem (heat equation). In addition, modelling the sintering process itself involves modelling the shrinkage of the material, which is in the domain of mechanics. In the literature, sintering has been modelled and simulated at three scales: microscopic [20, 75, 82, 85, 104], mesoscopic [17, 77] and macroscopic [55, 57, 57, 58, 59]. In this work, we interested in the simulation of microwave heating and sintering at the macroscopic scale. At this scale, the powder is described as a continuous medium [72, 97]. The macroscopic behaviour of the material is then the result from processes involved at the microscopic and atomistic levels. Consequently, the dielectric, thermal and mechanical parameters of the material depend, of course, on the temperature, but also on the porosity as it will be seen in Chapter 4.

This section first presents the equations associated with each physics and how they are coupled together. In Chapters 3, 4 and 5, this set of equations will be solved using the finite element method via the *COMSOL multiphysics*® software [23]. Here, the geometry of the computational domain, an idealisation of the microwave cavity, is described, and the boundary conditions of each equation are introduced. Finally, a mesh sensibility analysis is performed. Note that, although the equations describing the shrinkage are presented here, the main part of this work is devoted to the study of the heating stage. Sintering and the associated shrinkage will only be briefly discussed in Chapter 5.

2.3.1 Modelling of microwave heating and sintering

2.3.1.1 Electromagnetic problem: wave equation and boundary conditions

Maxwell’s equations cover all the aspects of electromagnetism. In order to describe the propagation of an electromagnetic wave, it is sufficient to combine Maxwell equations (Equations (1.1)-(1.4)) and the wave/matter interaction equations (Equations (1.5)-(1.7)). The electromagnetic wave propagation equation, demonstrated in Appendix D is written as:

$$\nabla \times ((\mu_r^*)^{-1}) \nabla \times \tilde{\mathbf{E}}_m = k_0^2 \left(\epsilon_r^* - \frac{j\sigma_e}{\omega\epsilon_0} \right) \tilde{\mathbf{E}}_m \quad (2.8)$$

where μ_r^* is the complex relative permeability, ϵ_r^* the complex relative permittivity, σ_e the electric conductivity, ω the microwave angular frequency, ϵ_0 the vacuum permittivity, and $k_0^2 = \omega^2 \mu_0 \epsilon_0$ the vacuum wave number, with μ_0 the vacuum permeability.

Depending on the medium of propagation, two boundary conditions can be considered:

- At the interface with a perfect conductor, the boundary conditions are given as [84, 89]:

$$E_t = 0, \quad H_n = 0 \quad (2.9)$$

where E_t is the tangential component of the electric field \mathbf{E} , and H_n is the normal component of the magnetic field \mathbf{H} .

- At the interface between two different dielectric materials labelled 1 and 2, the boundary conditions are given as [10, 79, 89]:

$$E_{t1} = E_{t2}, \quad H_{t1} = H_{t2}, \quad D_{n1} = D_{n2}, \quad B_{n1} = B_{n2} \quad (2.10)$$

2.3.1.2 Thermal problem

The heat transfer is modelled using the heat equation:

$$\bar{\rho} C_p \frac{dT}{dt} + \nabla \cdot (-\kappa \nabla T) = Q_{EM} \quad (2.11)$$

where T is the temperature field, $\bar{\rho}$ is the density, C_p is the specific heat, and κ is the thermal conductivity. The term Q_{EM} corresponds to the heat source expressing the coupling between the electromagnetic field and the thermal problem. This term is given in Equation (1.16) in Section 1.3.2.3.

2.3.1.3 Mechanics

Sintering (in solid phase) allows the transformation of a pulverulent compact into a densified compact. The mechanical state of the material during sintering is described by the momentum conservation equation. Neglecting inertia effects and gravity, it writes:

$$\nabla \cdot \boldsymbol{\sigma} = 0 \quad (2.12)$$

where $\boldsymbol{\sigma}$ is the Cauchy stress tensor. In accordance with the continuous sintering theory [72], the material being sintered is subject to elastic, plastic, viscous and thermal deformations. The stress tensor can then be expressed as

$$\boldsymbol{\sigma} = \frac{\sigma_{eq}}{\dot{\epsilon}_{eq}} (\varphi(\theta) \dot{\boldsymbol{\epsilon}} + (\psi(\theta) - \frac{1}{3} \varphi(\theta)) \text{tr}(\dot{\boldsymbol{\epsilon}}) \mathbf{I}) + Pl \mathbf{I} \quad (2.13)$$

where σ_{eq} and $\dot{\epsilon}_{eq}$ are the equivalent stress and strain rate respectively, $\dot{\boldsymbol{\epsilon}}$ is the strain rate tensor, \mathbf{I} is the identity tensor, Pl is the sintering stress, φ and ψ are the shear and mass modulus defined as a function of porosity θ :

$$\varphi = (1 - \theta)^2 \quad (2.14)$$

and

$$\psi = \frac{2(1 - \theta)^3}{3\theta} \quad (2.15)$$

The sintering stress Pl is written as a function of the average particle radius r_0 , porosity θ and surface energy α [77]:

$$Pl = \frac{3\alpha}{r_0}(1-\theta)^2 \quad (2.16)$$

The equivalent strain rate $\dot{\epsilon}_{eq}$ is written in terms of rate of change of volume $\dot{\epsilon}$ and shape $\dot{\gamma}$:

$$\dot{\epsilon}_{eq} = \frac{1}{\sqrt{1-\theta}} \sqrt{\varphi\dot{\gamma}^2 + \psi\dot{\epsilon}^2} \quad (2.17)$$

and

$$\dot{\epsilon} = \dot{\epsilon}_x + \dot{\epsilon}_y + \dot{\epsilon}_z \quad (2.18)$$

$$\dot{\gamma} = \sqrt{2(\dot{\epsilon}_{xy}^2 + \dot{\epsilon}_{xz}^2 + \dot{\epsilon}_{yz}^2) + \frac{2}{3}(\dot{\epsilon}_x^2 + \dot{\epsilon}_y^2 + \dot{\epsilon}_z^2) - \frac{2}{3}(\dot{\epsilon}_x\dot{\epsilon}_y + \dot{\epsilon}_x\dot{\epsilon}_z + \dot{\epsilon}_y\dot{\epsilon}_z)} \quad (2.19)$$

The equivalent stress and strain rate are related by a power law creep equation [57, 71]:

$$\dot{\epsilon}_{eq} = A(T)\sigma_{eq}^n \quad (2.20)$$

where A is a parameter defining the decrease in the resistance of the material to deformation with temperature and the stress exponent n defines the non-linearity of the material's behaviour [57, 71].

All the material parameters involved in Equations (2.8)-(2.13) depend on the microstructure of the material through, to first order, the porosity θ or, equivalently, the relative density $D = 1 - \theta$. Let V be the total volume of the porous material, and V_{pores} the pore volume ($V_{pores} = 0$ when $\theta = 0$). Porosity and relative density are then defined as :

$$\theta = \frac{V_{pores}}{V} = 1 - D = 1 - \frac{\bar{\rho}}{\bar{\rho}_{th}} \quad (2.21)$$

and

$$D = 1 - \frac{V_{pores}}{V} = \frac{\bar{\rho}}{\bar{\rho}_{th}} \quad (2.22)$$

where the theoretical density $\bar{\rho}_{th}$ is defined as

$$\bar{\rho}_{th} = \frac{m}{V - V_{pores}} \quad (2.23)$$

while the density $\bar{\rho}$ is

$$\bar{\rho} = \frac{m}{V} \quad (2.24)$$

with m the mass of the material.

When modelling or simulating not only the heating of the material but also the sintering step, that is the shrinkage of the material during the thermal cycle, the evolution of the θ porosity has to be explained. This can be done, for example, by an evolution equation based on assumptions about grain morphology. In Chapter 5, we prefer to express θ as a function of temperature from experimental dilatometry curves.

2.3.1.4 Multi-physics coupling and numerical resolution

Understanding microwave sintering requires understanding the multiphysics coupling between electromagnetism, heat transfer and mechanics as presented in Figure 2.7. In particular:

- Electromagnetic and thermal problems are coupled, in one direction, by the electric field, solution of wave propagation equation (2.8), whose energy dissipated in the material gives rise to a source term Q_{EM} in the heat equation (2.11). In the other direction, the dielectric parameters ε^* (Equation (1.8)) depend on the temperature T .
- Thermal and mechanical problems are coupled by the dependence of the heat capacity C_p and the thermal conductivity κ (heat Equation (2.11)), on the density $\bar{\rho}$. In turn, the density depends on the temperature.
- Mechanical and electromagnetic problems are coupled by the fact that, in addition to the temperature T , the dielectric parameters ε^* (Equation (1.8)) depend also on the density $\bar{\rho}$.

The temperature dependence of the various SiC and Al₂O₃ material parameters is presented in Appendix C. Moreover, the temperature and density dependence of some alumina parameters will be presented in Chapter 4.

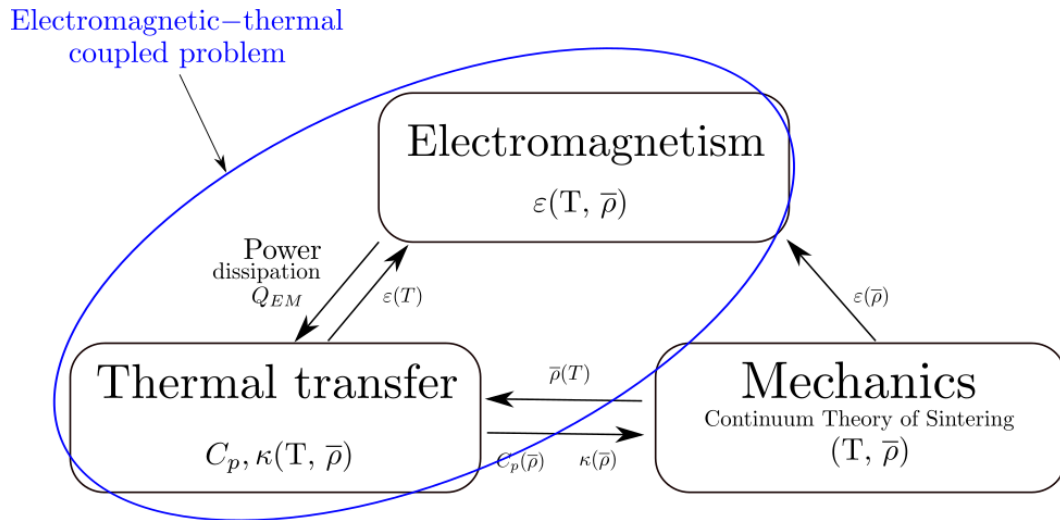


FIGURE 2.7 – Multiphysics couplings.

The general simulation procedure of microwave sintering, carried out with the *COM-SOL multiphysics*® software [23] software, is presented in Figure 2.8. First of all, temperature, density, material parameters and boundary conditions are initialised. Next, the staggered procedure consists at each time increment in the following sequence. The wave propagation equation (Equation (2.8)) is solved, in order to obtain the electromagnetic field. Using Equation (1.17), the dissipated electromagnetic power Q_{EM} is post-calculated and is introduced into the right hand side of the heat equation (Equation (2.11)). Solving

this equation provides the temperature field in the sample and the support. The porosity θ and density $\bar{\rho}$ are updated with this new temperature, and the mechanical problem is solved. Finally, the porosity/density is updated, as well as the different quantities depending on the temperature and density ($C_p, \kappa, \varepsilon^*$), and the time is incremented.

The simulations presented in Chapters 3 and 4 are dedicated to the study of microwave heating, where only the electromagnetic-thermal coupled problem is considered (blue box in Figure 2.7 and Figure 2.8). These simulations are performed for SiC and Al₂O₃ materials. The sintering of alumina with a SiC susceptor is treated experimentally in Chapter 5. This Chapter presents in addition first results concerning the simulation of sintering which requires solving the whole (electromagnetic-thermal-mechanic) problem with the procedure presented in Figure 2.8.

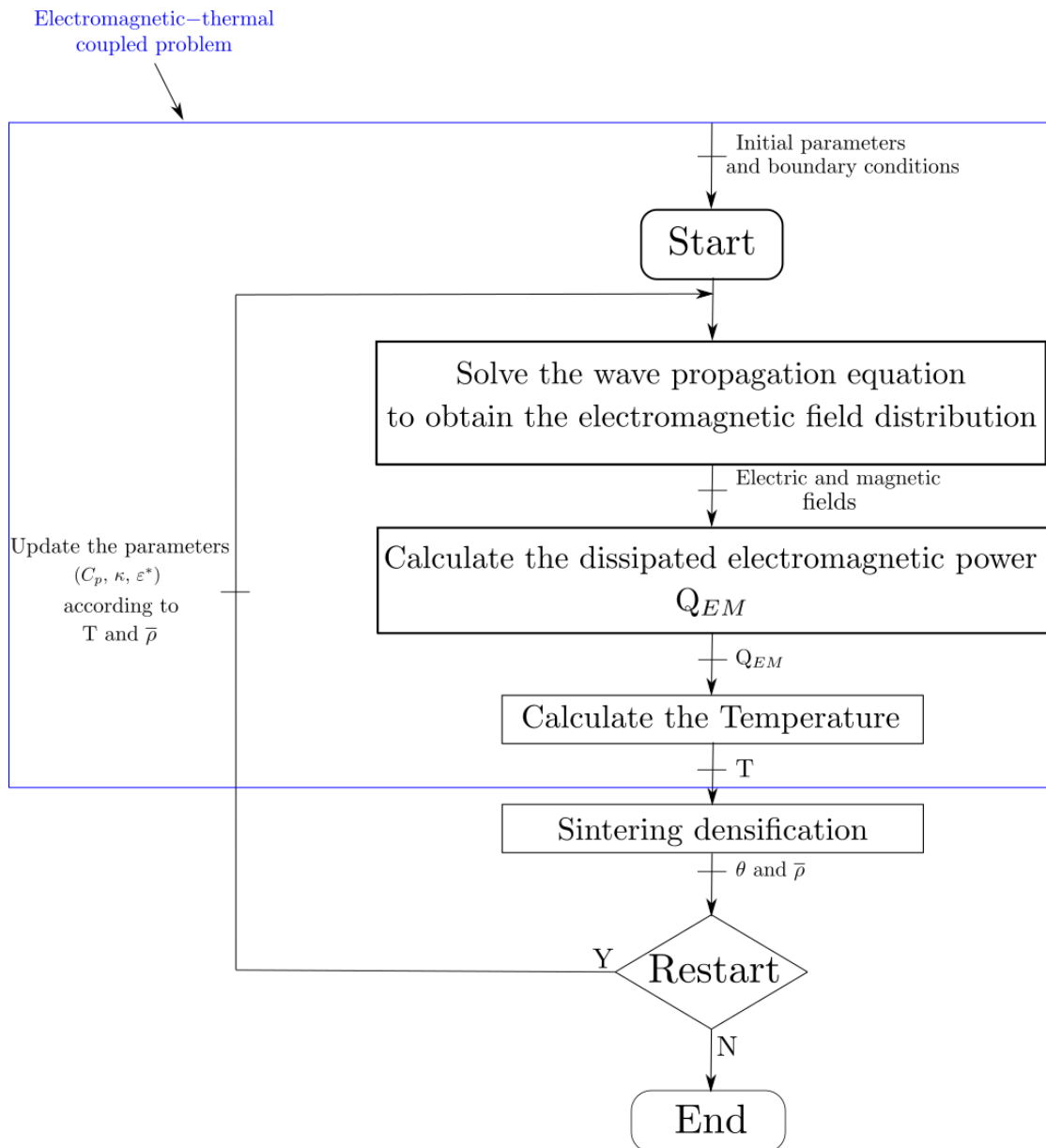


FIGURE 2.8 – General simulation procedure of microwave sintering.

Before heating and sintering simulations can be performed, the geometry of the computational domain must be designed to approximate the microwave cavity with sufficient

accuracy. Boundary and interface conditions must be considered and applied in order to complete and close the above equations. This is the purpose of the next section.

2.3.2 Computational domain and boundary conditions

Figure 2.9 shows the computational domain used for the simulations. As in the experimental setup (Figure 2.6), a sample is positioned on an insulating support. This heated system is placed inside a cavity limited by an iris on one side and a short-circuit piston on the other side. However, unlike experimental device, the chimneys are not taken into account in the cavity geometry. This modification reduces the computation cost.

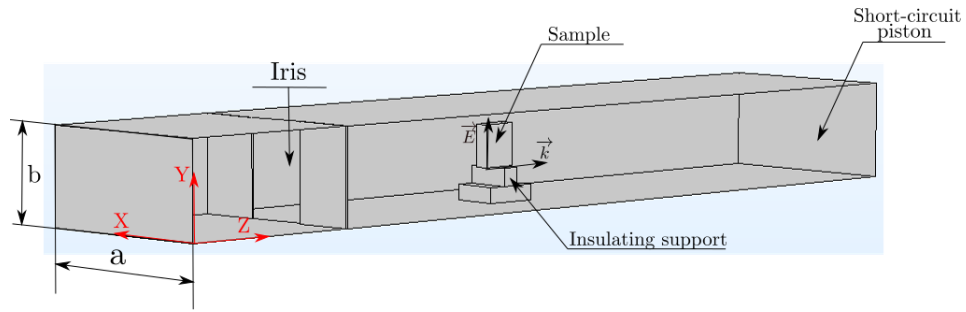


FIGURE 2.9 – 3D geometry of the microwave cavity [37].

Figure 2.10 presents a 2D schematic of microwave cavity with the different domains where the electromagnetic-thermal coupled problem (Figure 2.7 and Figure 2.8) is solved. The electromagnetic (EM) problem (Equation (2.8)) is solved by a frequency approach, in the whole domain $\Omega = \Omega_{waveguide} \cup \Omega_{sample} \cup \Omega_{support}$. The thermal problem (Equation (2.11)) is solved by using a linear finite element (FE) approximation in space combining with an implicit time discretisation. The thermal problem is solved only in the heated system $\Omega_{sample} \cup \Omega_{support}$. The thermal and dielectric parameters of the air, the sample (SiC and Al_2O_3), and the insulating support are presented in Appendix C.

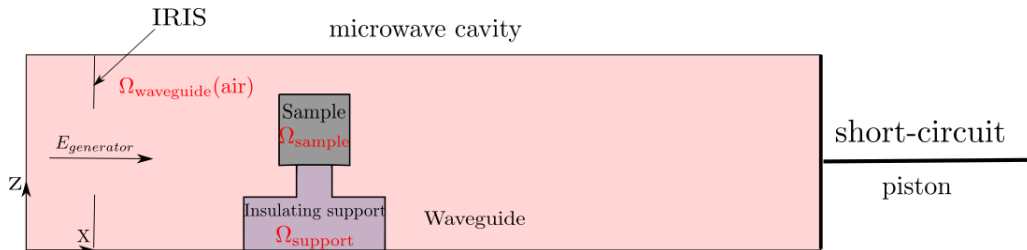


FIGURE 2.10 – Microwave cavity with the different physical domains [37].

The boundary conditions used to solve the electromagnetic problem (Equation (2.8)) are presented in Figure 2.11a. As described in 1.3.1, microwaves are reflected on a metal surface. That is why, the cavity walls are considered as perfect electric conductors which means that the wave is totally reflected by the internal surface of the cavity, *i.e.* $\mathbf{n} \times \mathbf{E} = \mathbf{0}$ on this surface, where \mathbf{n} is the unit vector orthogonal to the cavity wall. The second boundary condition for the EM problem is rectangular port in *COMSOL multiphysics*® software [23] denomination. This condition consists in defining the value of the incident power and the mode of propagation (transverse electric TE_{10p} in Figure 2.11a). Concerning the

thermal problem, the boundary conditions are presented in Figure 2.11b. Both radiative and convective fluxes, Φ_r and Φ_c , are considered at the surface Γ_{r-c} of the sample. These fluxes are given, respectively, by:

$$\Phi_r = \sigma_B \epsilon (T^4 - T_{amb}^4) \quad (2.25)$$

and

$$\Phi_c = h (T - T_{amb}) \quad (2.26)$$

where σ_B is the Stefan-Boltzmann's constant, ϵ the emissivity, T_{amb} is the ambient temperature and h is the convection exchange coefficient ($h = 5 \text{ W.m}^{-2}.\text{K}^{-1}$ in our simulations). At the sample/insulating support interface Γ_{cond} (in blue in Figure 2.11b), the thermal conductivity is the average of sample and support conductivities. The boundaries of the support are assumed to be adiabatic.

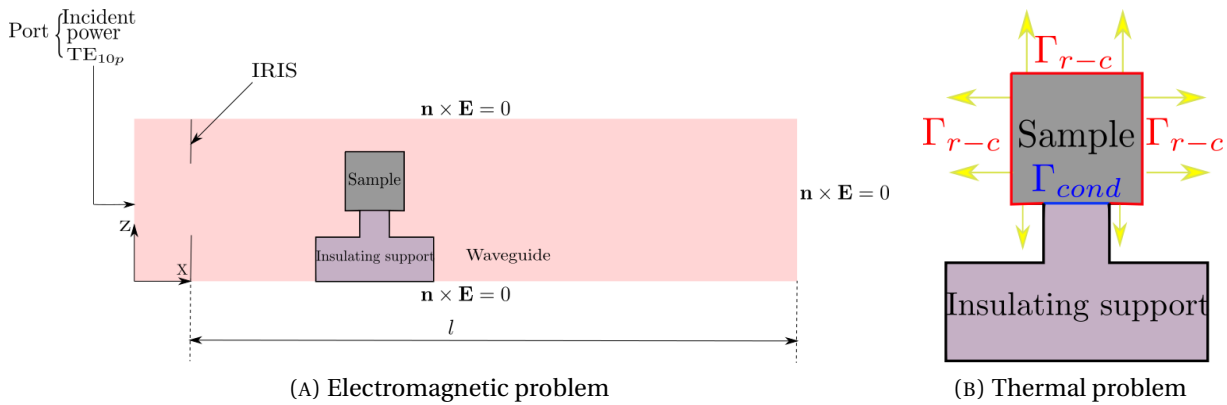


FIGURE 2.11 – Boundary conditions for the microwave heating [37].

2.3.3 Mesh sensibility analysis

To conclude the chapter, a mesh sensibility analysis is carried out in order to evaluate which mesh size can be chosen to limit the computation cost while having an acceptable discretisation error. This analysis is conducted by considering three different meshes, made up of linear tetrahedral elements, and referred to as coarse, fine and very fine meshes. The characteristic length of the elements discretising the cavity, as well as that of element discretising the heated system (sample and insulating support), are presented in Table 2.5 for the three meshes. With the exception of the mesh size, all the three simulations are performed under the same conditions (same cavity length, same material parameters, etc.), with a constant incident power equal to 50W. The properties of the SiC sample, together with those of the support, are given as a function of temperature in Appendix C. Figure 2.12 shows the temperature obtained in the three cases, plotted against time at a given position of the sample surface. Comparing the three curves, a difference of 60 K is found between the coarse and fine mesh. However, no significant difference is found between the fine and very fine mesh.

TABLE 2.5 – Characteristic lengths of elements of cavity, sample and insulating support for coarse, fine and very fine meshes.

Characteristic lengths (mm)	Coarse mesh	Fine mesh	Very fine mesh
Cavity	[7.6 - 42.3]	[4 - 7]	[2 - 3.5]
Sample & support	$[8.45 \times 10^{-2} - 8.4]$	2	[0.1 - 1]

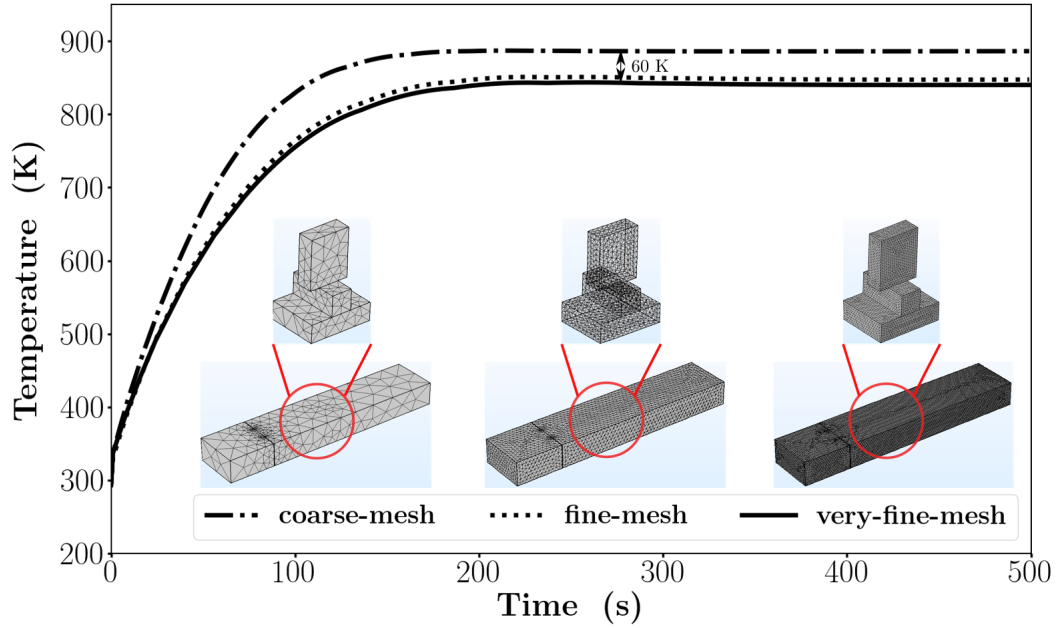


FIGURE 2.12 – Mesh sensibility for coarse, fine and very fine meshes [37].

Table 2.6, presents the number of degrees of freedom (DOF) for the coupled problem (EM and thermal) and the computation time (on 12 cores of an Intel Xeon Gold 6128 bi-processor at 3.4 GHz) obtained for the three different meshes after 500 time increments. The computation time for the very fine mesh is shown to be 10 times higher than for the fine mesh, without any significant improvement of the results. Therefore, the fine mesh will be used in the rest of this work.

TABLE 2.6 – Mesh sensitivity analysis: number of DOF and computation time (on 12 cores of an Intel Xeon Gold 6128 bi-processor at 3.4 GHz) for three different meshes.

	Coarse mesh	Fine mesh	Very fine mesh
DOF	4.3×10^4	6.7×10^5	5.1×10^6
Computation time (s)	1.3×10^2	1.5×10^3	1.3×10^4

2.4 Conclusion

Throughout this chapter, temperature has emerged as a key element in understanding and controlling the microwave sintering process. From an experimental point of view, a conventional temperature measuring device, such as thermocouples, which usually provide accurate temperature information, cannot be used in a microwave cavity due to interactions with the electromagnetic field. In this work, two instruments are used to measure the temperature: a pyrometer to determine the temperature at a specific point on the surface of the heated sample, and an infrared camera, to determine a surface temperature field. However, both instruments have to be calibrated to the material being heated. This calibration requires measuring the emissivity of the material in the temperature range of interest for sintering. Among the different methods presented in the literature, we have chosen a method consisting in carrying out this measurement in black body condition in a conventional furnace. In this way, the emissivity value is assumed to be independent of the environment, the use of calibration materials is avoided and temperature can be measured by a thermocouple.

The numerical simulation of microwave heating and sintering is based on solving three coupled problems: the electric field propagation equation, the heat equation and the solid mechanics momentum balance to describe the shrinkage associated with sintering. Again, the temperature is a key element, since all the material parameters are temperature dependent. The density (or alternatively porosity) is, for the same reason, the other key factor. A simulation provides several insights. First of all, the comparison of the results of the simulation and the experiment in very specific and simple situations, allows to decorrelate the phenomena, to validate or not the model used to describe them, and thus to evaluate our "theoretical" knowledge of the microwave heating/sintering process. This type of comparison will be made in the next two chapters.

Résumé en Français :

Tout au long de ce chapitre, la température est apparue comme un élément clé pour comprendre et contrôler le processus de frittage par micro-ondes. D'un point de vue expérimental, un dispositif conventionnel de mesure de la température, tel que les thermocouples, qui fournissent généralement des informations précises sur la température, ne peut pas être utilisé dans une cavité micro-ondes en raison des interactions avec le champ électromagnétique. Dans ce travail, deux instruments sont utilisés pour mesurer la température : un pyromètre pour déterminer la température en un point spécifique de la surface de l'échantillon chauffé, et une caméra infrarouge, pour déterminer un champ de température en surface. Cependant, les deux instruments doivent être calibrés en fonction du matériau chauffé. Ce calibrage nécessite de mesurer l'émissivité du matériau dans la plage de température d'intérêt pour le frittage. Parmi les différentes méthodes présentées dans la littérature, nous avons choisi une méthode consistant à effectuer cette mesure en corps noir dans un four conventionnel. De cette manière, la valeur de l'émissivité est supposée indépendante de l'environnement, l'utilisation de matériaux de calibration est évitée et la température peut être mesurée par un thermocouple.

La simulation numérique du chauffage et du frittage par micro-ondes est basée sur la résolution de trois problèmes couplés : l'équation de propagation du champ électrique, l'équation de la chaleur et le bilan de quantité de mouvement en mécanique des solides pour décrire le retrait associé au frittage. Là encore, la température est un élément clé, puisque tous les paramètres matériaux dépendent de la température. La densité (ou alternativement la porosité) est, pour la même raison, l'autre facteur clé. Une simulation fournit plusieurs informations. La comparaison des résultats de la simulation et de l'expérience dans des situations très spécifiques et simples, permet de décorréliser les phénomènes, de valider ou non le modèle utilisé pour les décrire, et donc d'évaluer nos connaissances " théoriques " du procédé de chauffage/frittage par micro-ondes. Ce type de comparaison sera effectué dans les deux prochains Chapitres.

Chapter 3

Numerical and experimental thermal analysis for direct microwave heating of Silicon Carbide SiC

Contents

3.1 Introduction	60
3.2 Experimental procedure	60
3.2.1 Emissivity measurement	60
3.2.2 Microwave heating	61
3.3 Numerical simulation	63
3.3.1 Numerical results	63
3.3.2 Discussion	66
3.3.3 Sensitivity analysis	67
3.3.4 Effect of the insulating support	72
3.4 Conclusion	74

3.1 Introduction

This chapter presents experimental and numerical results of the thermal analysis for direct microwave heating of silicon carbide (SiC). Using the methods presented in Chapter 2, the apparent emissivity evolution with temperature of a SiC sample is measured. Then the results of microwave heating are presented for four different sample orientations. These results are published in Ghorbel *et al* [37]. The third part is dedicated to the study of sensitivity to the microwave heating of the material parameters. For these simulations, the insulating support is considered as transparent to microwaves. This assumption is then discussed. For this purpose, a comparison between an insulating support considered as microwave transparent (Hyp 1) or not (Hyp 2) is conducted.

3.2 Experimental procedure

3.2.1 Emissivity measurement

The emissivity of SiC sample is evaluated using the method presented in Section 2.2.2.2. In this study, a parallelepipedic sample made of 99% grade SiC (SCERAM Advanced Ceramics [95] supplier) with dimensions 15.7 mm × 6.3 mm × 19 mm is used. The hollow cylinder used to recover black body conditions, is also made of SiC material. As mentioned in Section 2.2.2.2, the value of the emissivity is evaluated at the end of different temperature stages (pyrometer calibration point in Figure 2.5b).

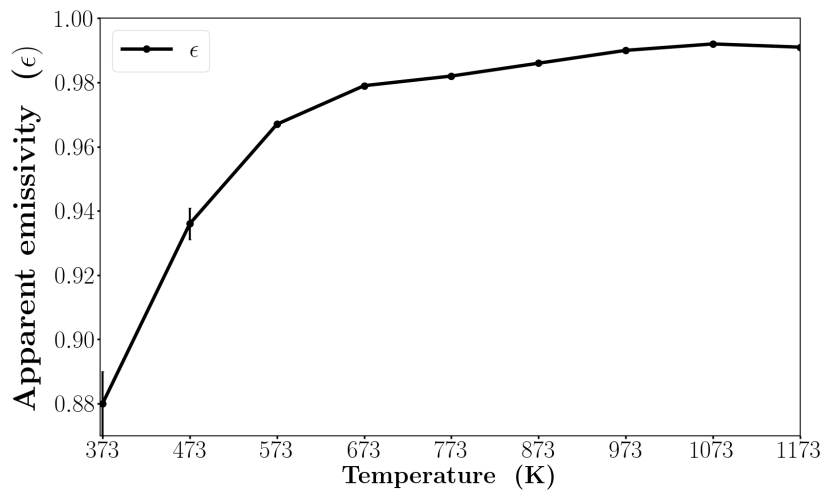


FIGURE 3.1 – Apparent emissivity evolution in range of the temperature [373 K - 1173 K] (published in [37]).

Figure 3.1 shows experimental results of the apparent emissivity, obtained in the range of the temperature [373 K- 1173 K]. In this range, the apparent emissivity evolves from 0.88 to 0.98. This results are in agreement with the value of 0.9 used by Manière *et al.* in [56, 57] and with data in the material emissivity table found in the literature [61].

3.2.2 Microwave heating

After calibrating the emissivity, the SiC sample is placed in the single mode cavity, in different orientations. Figure 3.2 shows these orientations where the dimensions of each case are given along X, Y and Z directions. The red dot figuring on the sample surface corresponds to the place where the pyrometer is focused.

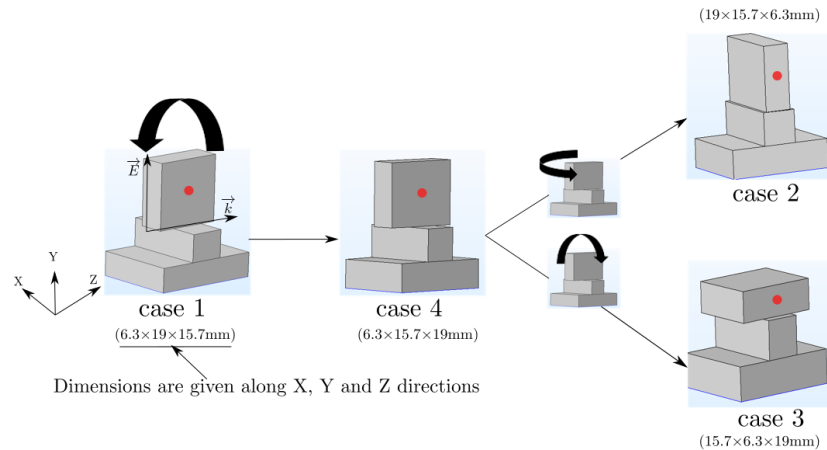


FIGURE 3.2 – Different orientations studied for microwave heating of a SiC sample [37]. The red point presents the measurement point of the temperature.

As described in the microwave set-up (Section 3.2.2), and after reaching the resonance of the cavity, the SiC sample is heated for the four orientations (Figure 3.2). Figure 3.3 presents the change over time of the reflected power P_r for the studied orientations when the incident power is set to 50 W. The reflected power increases until reaching a steady state, which depends on the orientation of the sample, and ranges between 1 W (case 1) and 11 W (case 3).

The cavity length for case 1 - 4 is 334 mm, 337.5 mm, 345.8 mm and 338.7 mm respectively. These lengths are presented by star markers in the following results (Figure 3.6) and remain fixed during microwave heating.

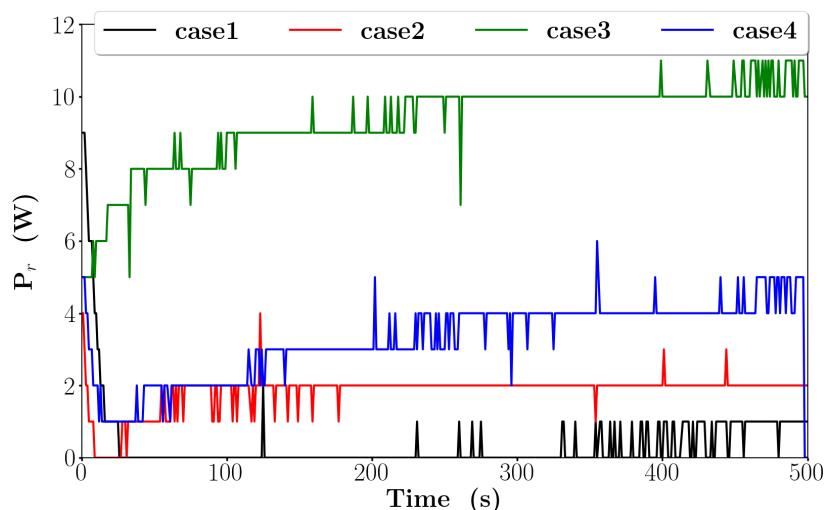


FIGURE 3.3 – Reflected power P_r for the studied cases with an incident power $P_{in} = 50$ W [37].

Figure 3.4 presents the temperature change over time at the measurement point for the four orientations. Note that, small disruptions on temperature evolutions are due to the change of emissivity value done during heating. In each situation, the temperature increases until reaching a constant value after 200 seconds. The steady temperature is 900 K, 860 K, 720 K and 820 K for cases 1 - 4 respectively. The final temperature is correlated to the reflected power presented in Figure 3.3, the lower the steady reflected power P_r , the higher the temperature.

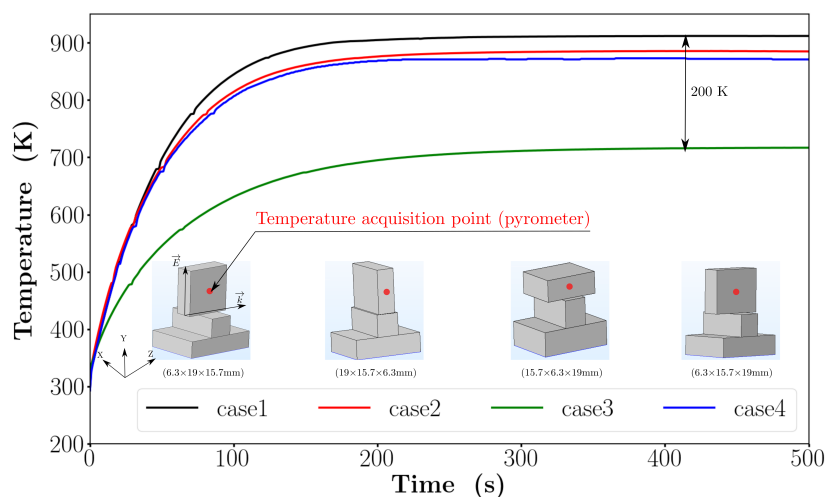


FIGURE 3.4 – Temperature evolution at the temperature measurement point for the four cases [37].

3.3 Numerical simulation

3.3.1 Numerical results

Using the 3D geometry of the microwave cavity presented in Figure 2.9, the boundary conditions (EM and thermal) described in Figure 2.11, and considering the mesh sensitivity analysis (Section 2.3.3), the fine mesh will be used in the following. Before simulating the microwave heating, the resonance of the cavity has to be set by adjusting the length l of waveguide with the short circuit piston. This setting allows the existence of a stationary wave: the incident and reflected waves are in phase, their maxima add therefore together, and a constructive interference occurs. At room temperature, the length is chosen such as a TE_{104} mode appears, it corresponds to an empty cavity length equal to 342 mm. This value differs from the theoretical one. This theoretical length given by Equation 1.25 using $a = 86.36$ mm, $b = 43.18$ mm, $n = 1$, $m = 0$, $p = 4$ and $\omega = 2\pi f$ with $f = 2.45$ GHz is of 345.44 mm. The experimental one is 350 mm¹. The gap between numerical, experimental and theoretical values comes from the geometry approximations, the presence of an iris and the absence of the cylindrical chimney (Figure 2.6) in the simulations. Cavity walls are also considered to be perfectly electrically conductive and the insulating support is transparent to microwaves (Hyp 1).

Figure 3.5 a) shows the intensity of the computed electric field in the empty cavity at room temperature, represented in YZ plan. As expected, the electric field has four maxima since a TE_{104} excitation has been prescribed. The maximum intensity in this case is 6.49×10^4 V/m. When the sample and the insulating support are placed in the cavity, the electric field is modified. Figure 3.5 b) presents the computed electric field for the orientation corresponding to case 1 (Figure 3.2). It is observed that the incident and reflected waves are no longer in phase. Four maxima are still detected but with a lower intensity equal to 1.39×10^4 V/m. As in experiments, the resonance is recovered by adjusting the length of the waveguide with the short-circuit piston until maximizing the electric field intensity, or alternatively, minimizing the reflected power P_r . Thus, the maximum of the electric field \mathbf{E} turns to 9.31×10^4 V/m which corresponds to a cavity length of 336.5 mm. The isovalues of this electric field are represented in Figure 3.5 c). It can be noted that the highest magnitude is not inside the sample, but outside it. This is due to the high value of the real part of the SiC permittivity ($\epsilon_r = 6.1 + 0.5j$ at T_{amb} , see Appendix C) compared to that of the air in Ω_{cavity} ($\epsilon_r = 1$) and combined with the continuity of the electric displacement field \mathbf{D} .

1. measurement was realized using Vector Network Analyzer

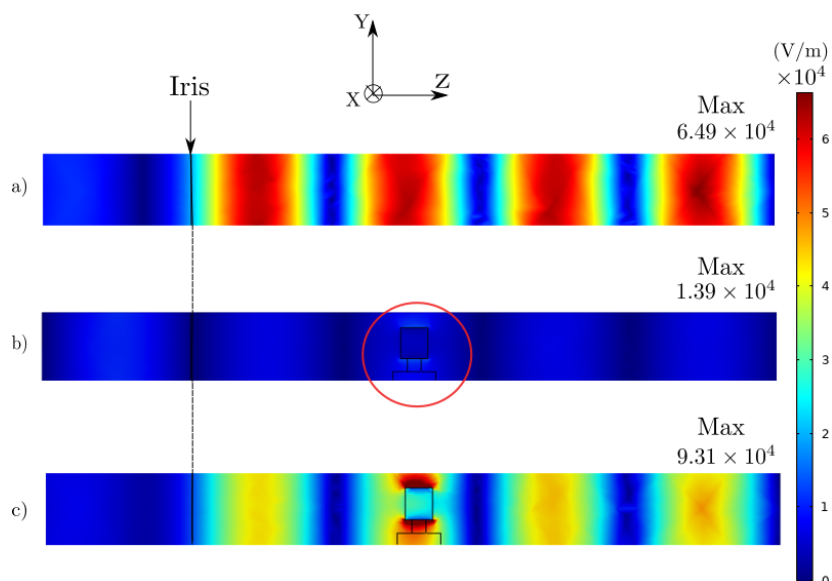


FIGURE 3.5 – Computed electric field a) empty cavity b) cavity, sample and insulating support before resonance, c) cavity, sample and insulating support after resonance for case 1 [37].

For each orientation, the cavity length is set at room temperature, where the average of the electric field intensity over the whole domain is maximum at the resonance. These average values are plotted with respect to the cavity length in Figure 3.6 for the four orientations. The resonate cavity length corresponds to the maximum of the average intensity. The cavity lengths are 336.5 mm, 337.2 mm, 339.5 mm and 337.2 mm for case 1 - 4 respectively. The numerical cavity lengths are different from that measured experimentally, which are described by star markers in Figure 3.6. This difference varies from 0.36 mm for case 2 to 6.3 mm for case 3, and comes from the assumptions made in simulations : simplified geometry (without description of the chimney), cavity walls considered to be perfectly electrically conductive and insulating support transparent to microwaves (Hyp 1).

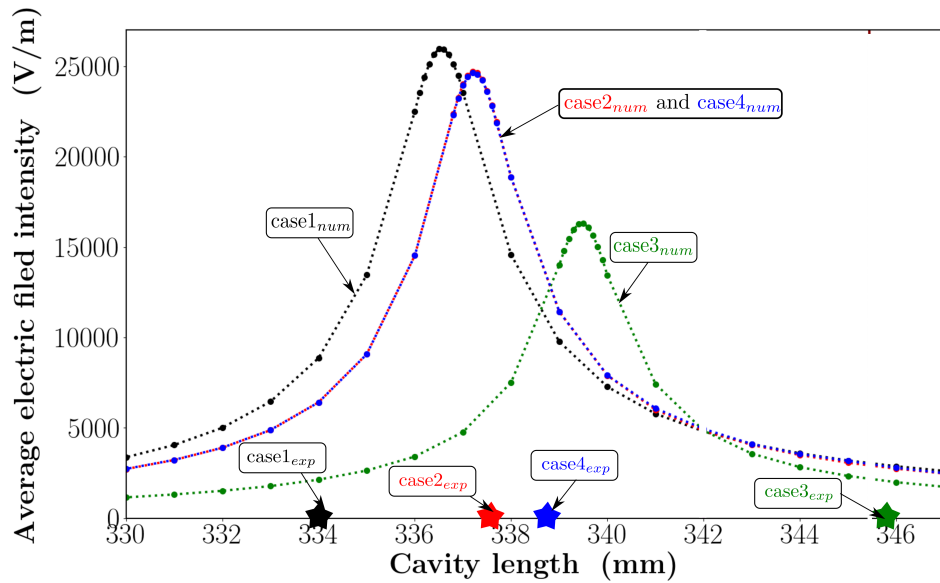


FIGURE 3.6 – Average intensity of the electric field obtained by simulation for different cavity lengths in the four investigated cases. Star markers correspond to the cavity lengths measured experimentally [37].

Using a constant power of 50 W, the microwave heating of the SiC sample is now investigated. The experimental and numerical temperatures, measured at the sample surface, are plotted as functions of time in Figure 3.7 for the four cases studied. These simulations are performed using the materials parameters presented in Appendix C and considering the insulating support as transparent to microwaves (Hyp 1 in Appendix C). A good agreement between the simulation and the experimental results is observed for all four cases. Despite slightly lower kinetics to reach equilibrium in the numerical description, the temperature difference at steady state is 2 K for case 1 and in the order of 20 K for the other cases. These results indicate that the approximations done are not so restrictive to reproduce the experimental results (insulating support holder considered to be transparent to microwaves (Hyp 1 in Appendix C), cavity walls considered as perfect conductors, no description of the chimney) and that the material parameters used are reliable.

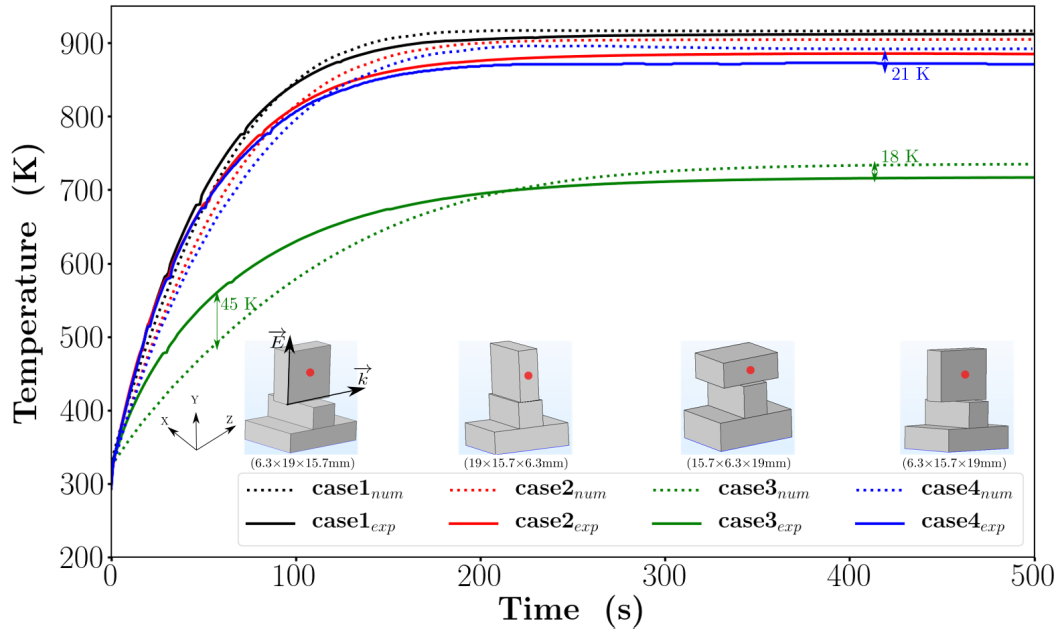


FIGURE 3.7 – Numerically and experimentally temperature evolution at the temperature measurement point (red point) for the four cases [37].

3.3.2 Discussion

The effect of sample orientation has a huge impact on the heating, as highlighted in Figure 3.7. The maximum temperature at steady state is obtained for case 1 ($T = 916$ K), followed by case 2 ($T = 905$ K), case 4 ($T = 892$ K), and case 3 ($T = 735$ K), respectively. This result is related to the polarization field (described in Section 1.3.2.1) which is higher when the sample is oriented along the electric field. In such situations, the dipolar losses are higher leading to a better heating, as more energy is absorbed and converted into heat. The simulations nicely recover this effect since the correspondence between the equilibrium temperature and the height of the sample in the direction of the electric field direction is respected. Note that the equilibrium temperature is correlated with the maximum values of average electric field intensity presented in Figure 3.6. The slight difference between case 2 and case 4 may result from the difference of the surface area in contact between the sample and the insulating support.

As mentioned previously in Section 3.2.2, the heating is very sensitive to the length of the waveguide, which must be adjusted to maximize the stationarity of the waves. Figure 3.8 presents the equilibrium temperature at the sample surface as a function of the length of the waveguide, for the different sample orientations. These curves show that the length of the cavity has to be set with accuracy to produce optimal heating of the sample. A deviation of one millimeter from the resonance length can lead to a drastic drop in the equilibrium temperature. In the simulations, a precision of one-tenth of a millimeter on the length of the cavity is required to optimize the heating. It can be noted that the resonance length also correlates with the orientation of the sample with the same trend obtained for the equilibrium temperature. Thus, the shortest cavity length corresponds to case 1 where the highest dimension of the sample is aligned with the electric field.

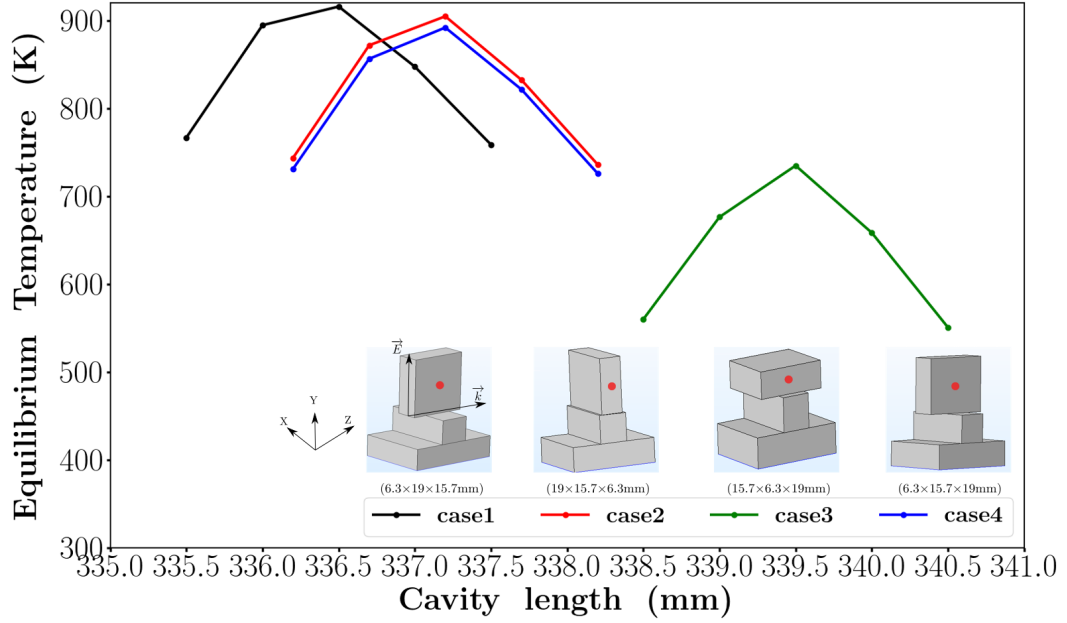


FIGURE 3.8 – Equilibrium temperature measured at red point, as a function of the cavity length for the different sample orientations [37].

3.3.3 Sensitivity analysis

The aims of this section is to study the sensitivity of the heating to the material parameters and more precisely, the real part and the imaginary part of the relative permittivity (ϵ'_r and ϵ''_r) for dielectric parameters, the specific heat (C_p) and the thermal conductivity (κ) for thermal parameters. This study is performed using the case 1 orientation, with a constant incident power $P_{in} = 50$ W and a fixed cavity length equal to 336.5 mm (the resonant length at ambient temperature for case 1). A sensitivity analysis to a given parameter, consists of carrying out two simulations with, respectively, a minimum and a maximum value of this parameter, chosen as fixed during heating, while the other quantities are free to evolve with the temperature. Table 3.1 presents the values of SiC parameters used for the sensitivity study where $F(T)$ refers to a polynomial form as function of temperature (presented in polynomial form in the appendix C). Results of this study of sensitivity are presented below.

	ϵ'	ϵ''	C_p [J.kg ⁻¹ .K ⁻¹]	κ [W.m ⁻¹ .K ⁻¹]
max	7.3			
min	6.0	F(T)	F(T)	F(T)
max		0.58		
min	F(T)	0.46	F(T)	F(T)
max			1286	
min	F(T)	F(T)	635	F(T)
max				120
min	F(T)	F(T)	F(T)	60

TABLE 3.1 – Values of material parameters for the study of sensitivity.

3.3.3.1 Real part of the relative permittivity

Figure 3.9a) describes the real part of the relative permittivity ϵ'_r as function of the temperature. Using the polynomial expression presented in Appendix C for the temperature range [273 K - 1273 K], ϵ'_r evolves from $\epsilon'_{r,min} = 6$ to $\epsilon'_{r,max} = 7.3$. Both extreme values ($\epsilon'_{r,min}$ and $\epsilon'_{r,max}$) are used to simulate the sensitivity of the heating to the real part of the relative permittivity.

Figure 3.9b) presents the temperature change over time for both values of ϵ'_r . It is observed that the simulated temperature using $\epsilon'_{r,min}$ is 150 K higher than with $\epsilon'_{r,max}$ after 150s of heating. This temperature difference decreases to 100 K at steady state.

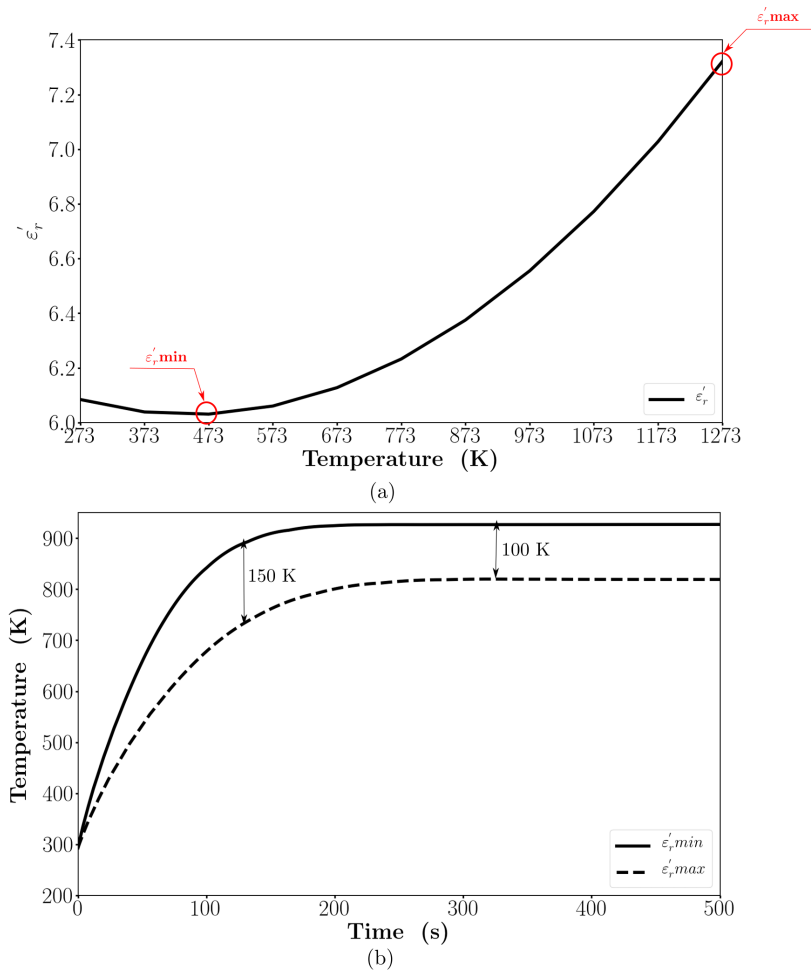


FIGURE 3.9 – (a) ϵ'_r evolution as function on temperature and (b) temperature evolution at the surface of a SiC sample in case 1 orientation for $\epsilon'_{r,min}$ and $\epsilon'_{r,max}$ values.

The real part of the relative permittivity ϵ'_r is the capacity of a material to store the potential energy of the field. Thus, the norm of the electric field during the simulation is plotted in Figure 3.10. This norm of the electric field is in the order of 26000 V/m for $\epsilon'_{r,min}$. However, using $\epsilon'_{r,max}$, this value is lower and of the order of 20500 V/m. This result is due to the resonant cavity which is determined with $\epsilon'_r = 6.1$ which is closed to $\epsilon'_{r,min}$. Since the heat source Q_{EM} is a function of E^2 , the heat source with $\epsilon'_{r,min}$ leads to higher temperatures.

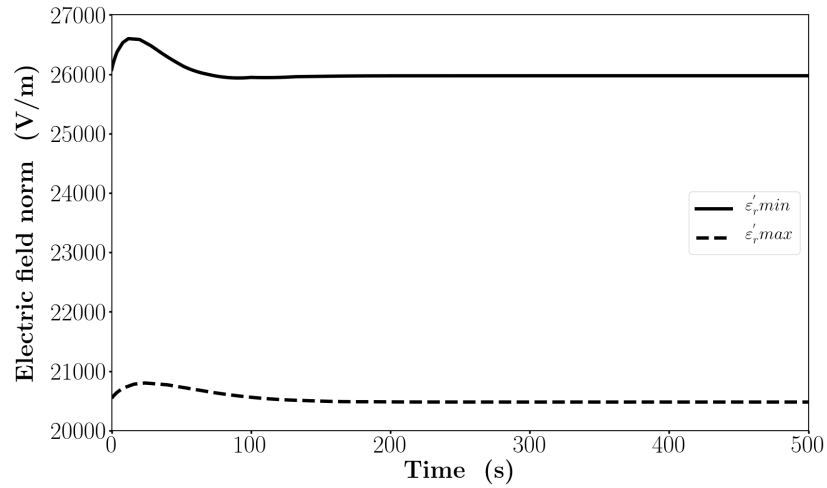


FIGURE 3.10 – Norm of the electric field during microwave heating for ϵ'_r min and ϵ'_r max.

3.3.3.2 Imaginary part of the relative permittivity

As for the real part of the relative permittivity ϵ'_r , the sensitivity of the heating to the imaginary part of the relative permittivity ϵ''_r is studied in this section. First, the evolution of ϵ''_r as a function of temperature is plotted using the polynomial expression presented in Appendix C. Figure 3.11a) presents this evolution for the temperature range [273 K - 1273 K] for which a minimum is reached at 473 K. This minimum value ϵ''_r min is equal to 0.46. A maximum value ϵ''_r max equal to 0.58 is reached for 1273 K.

Both extreme values (ϵ''_r min and ϵ''_r max) are used to simulate the sensitivity of the heating to the imaginary part of the relative permittivity. Figure 3.11b) presents the change of temperature over time during microwave heating for ϵ''_r min and ϵ''_r max parameters where the other parameters (the real part of the permittivity, the specific heat and the thermal conductivity) are function on temperature (polynomial form presented in Appendix C) and the cavity length $l = 336.5$ mm. Figure 3.11b) shows that the temperature dependence of ϵ''_r has very limited influence on the heating of the SiC sample.

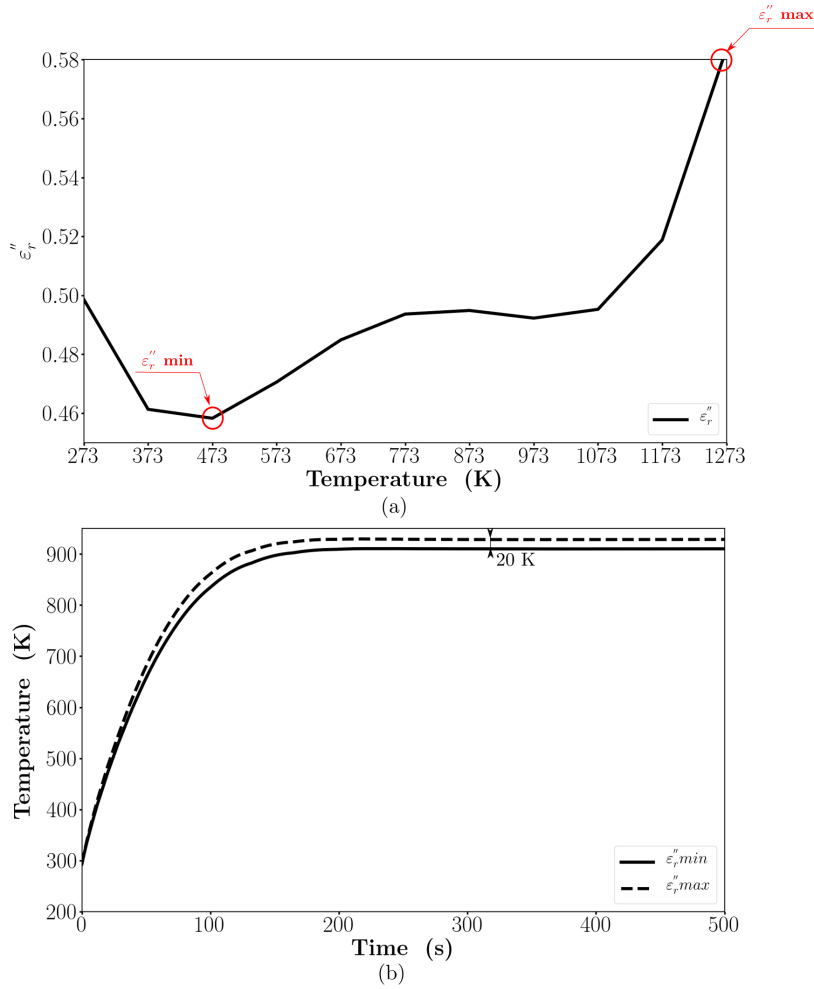


FIGURE 3.11 – ϵ_r'' sensitivity : (a) ϵ_r'' evolution as function on temperature (b) Temperature evolution at a surface of a SiC sample in case 1 orientation for $\epsilon_r'' \text{ min}$ and $\epsilon_r'' \text{ max}$ values.

3.3.3.3 Specific heat

After studying the dielectric parameters (ϵ_r' , ϵ_r''), this section is dedicated to a study of the sensitivity of the microwave heating to the thermal parameters. Specific heat C_p is the first parameter studied. The methodology is the same as for the study of dielectric parameters. The evolution of the specific heat as a function of temperature is plotted in Figure 3.12a) from the polynomial expression given in Appendix C. The value of the specific heat increases from $635 \text{ J.K}^{-1}.\text{kg}^{-1}$ ($C_p \text{ min}$) at 273 K to $1286 \text{ J.K}^{-1}.\text{kg}^{-1}$ ($C_p \text{ max}$) at 1273 K. Both extreme values ($C_p \text{ min}$ and $C_p \text{ max}$) are used to simulate the sensitivity of the microwave heating to the specific heat. Figure 3.12b) presents the temperature change over time during the microwave heating for $C_p \text{ min}$ and $C_p \text{ max}$. The temperature difference between the two simulations (with $C_p \text{ min}$ and $C_p \text{ max}$) reaches 200 K around 80s before vanishing once steady state is achieved. The specific heat corresponds to the capacity of a material to accumulate energy, which leads to a delay on the heating kinetics for high C_p values. Since C_p is a factor of the time derivative in the heat equation, this parameter no longer has any effect in the steady state where this derivative is zero.

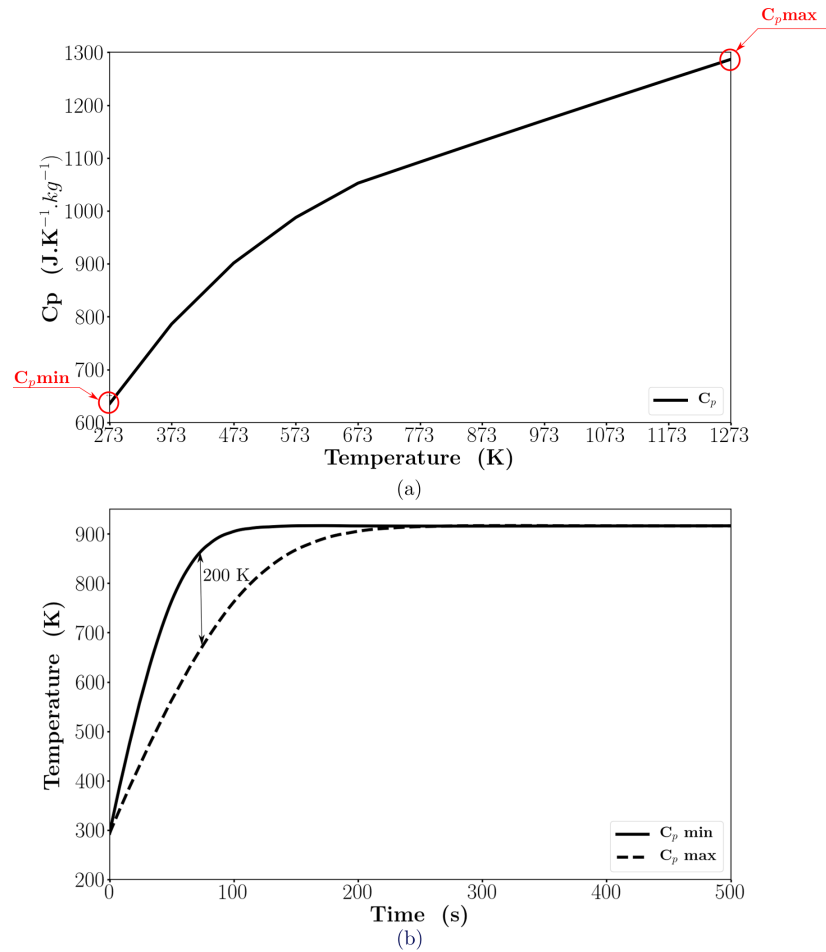


FIGURE 3.12 – (a) C_p change over temperature, and (b) temperature change over time at a surface of a SiC sample in case 1 orientation for C_p min and C_p max values.

3.3.3.4 Thermal conductivity

The second thermal parameter studied after C_p is the thermal conductivity κ . As for the other parameters, the thermal conductivity evolution as function of the temperature is plotted in Figure 3.13a). It can be noted that the thermal conductivity decreases from $120 \text{ W.m}^{-1}.\text{K}^{-1}$ at 273 K ($\kappa \text{ max}$) to $60 \text{ W.m}^{-1}.\text{K}^{-1}$ at 1273 K ($\kappa \text{ min}$). Both extreme values are used ($\kappa \text{ min}$ and $\kappa \text{ max}$) are used to study the sensitivity to the microwave heating of the thermal conductivity. Figure 3.13b) presents the temperature change over time during simulations of microwave heating. This result shows that during the heating of SiC, the diffusive flux is negligible in the heat equation compared to the contribution of the electromagnetic wave. It may be added that even multiplying $\kappa \text{ max}$ arbitrarily by 10 gives a steady state temperature that is only 25K higher, while dividing $\kappa \text{ min}$ by 10 gives a temperature that is 13K lower.

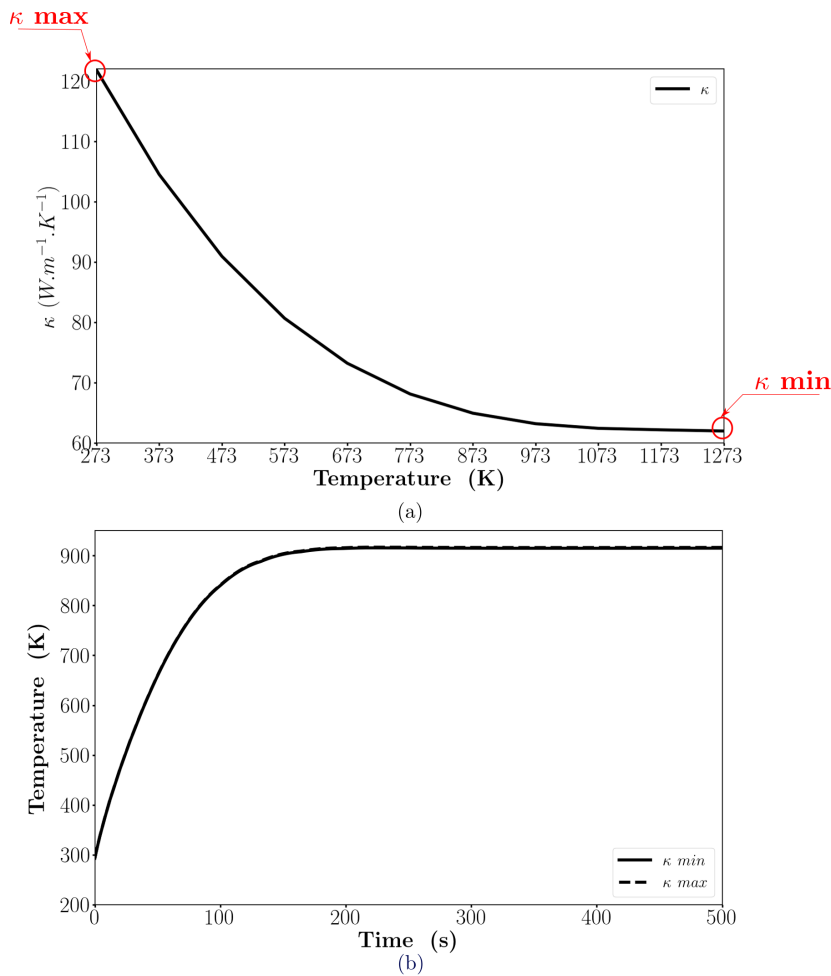


FIGURE 3.13 – (a) κ change over temperature and, (b) temperature change over time at a surface of the SiC sample in case 1 orientation for κ_{min} and κ_{max} values.

3.3.4 Effect of the insulating support

In previous simulations, the insulating support was assumed to be transparent to microwaves in comparison to SiC which is absorber material. The relative permittivity has been set to that of the air ($\epsilon_r = 1$). This hypothesis is noted Hyp 1 in Appendix C. If we consider that the insulating support is not transparent to microwaves. In this case (hyp 2), the values of its permittivity (real part and imaginary part) can be found in Appendix C. Since ϵ_r is not equal to 1, the resonant cavity length has to be determined once again. Figure 3.14 presents the average electric field intensity as function of the cavity length using case 1 orientation. It can be noted that the resonant length for Hyp 2 is equal to 334.2 mm which is shorter than for Hyp 1 as ϵ'_r is higher.

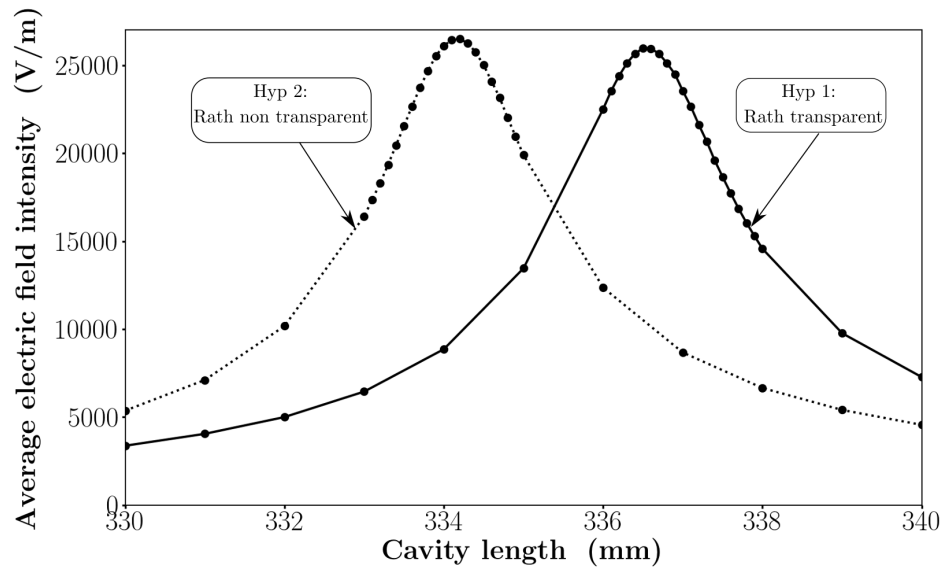


FIGURE 3.14 – Average electric field intensity for Hyp 1 and Hyp 2 for case 1.

Once the resonant cavity length determined for both assumptions ($l = 336.5$ mm for Hyp 1 and $l = 334.2$ mm for Hyp 2), the microwave heating is investigated for the case 1 orientation. Figure 3.15 presents the temperature change over time during microwave heating for the two hypothesis. No significant difference is noted between hypothesis 1 and 2. However, this result is true when considering the heating of SiC which has a high permittivity and therefore couples well with microwaves. The observation can be more nuanced for the heating of alumina.

In the rest of this work, hypothesis 2 will be used to simulate the microwave heating and the sintering of alumina.

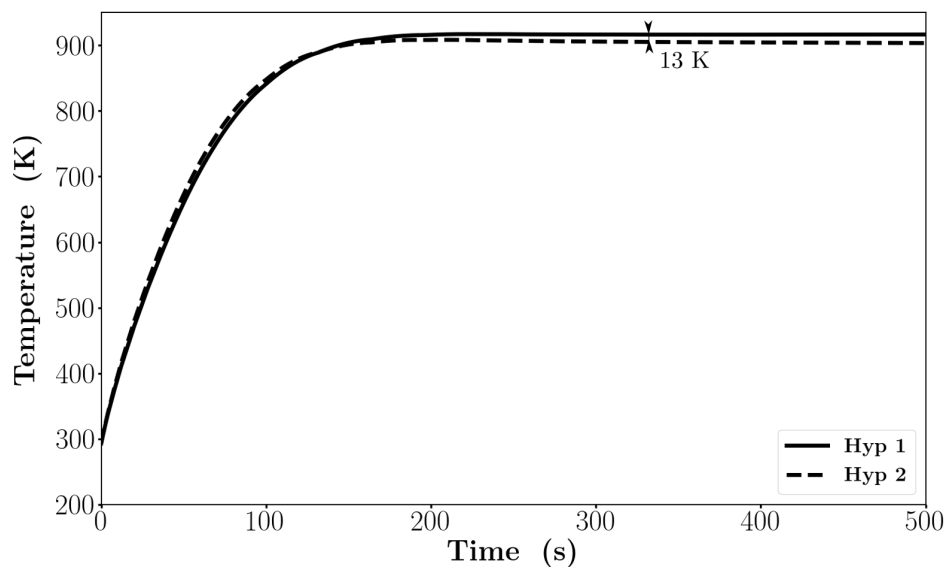


FIGURE 3.15 – Temperature evolution during microwave heating for Hyp 1 and Hyp 2 using case 1.

3.4 Conclusion

This chapter presented the experimental and the numerical results of microwave heating on a parallelepipedic sample in silicon carbide (SiC), a material with a high dielectric loss at room temperature. The SiC emissivity is first measured in black body condition, following the procedure described in Chapter 2. The sample is then placed in a 2.45-GHz single-mode cavity. Four different orientations are considered. After adjusting the length of the cavity to the resonant length at room temperature, the sample is heated with a constant power of 50 W. The numerical simulations, performed using the finite element software *COMSOL multiphysics*® [23], consisted in solving an electromagnetic-thermal problem (Chapter 2) under the same conditions as in the experimental procedure. Despite the approximations made in the numerical modelling (insulating support considered transparent to microwaves, cavity wall considered to be a perfect conductor, no description of the chimney), a good agreement between the simulations and the experimental results is found for all four cases. In particular, the most efficient heating is obtained when the sample is oriented along the electric field. The sensitivity of the electric field, and thus of the microwave heating, to the material parameters (dielectric and thermal parameters) was also highlighted. The assumption of an insulating support transparent to microwaves (Hyp 1) is then discussed. Although very little difference was found in the heating of SiC with a microwave transparent or non-transparent support, the simulations in the next two chapters will consider the support as not fully transparent. This may have an impact on the direct heating of alumina, which couples less than SiC.

Résumé en Français :

Ce chapitre présente les résultats expérimentaux et numériques du chauffage par micro-ondes d'un échantillon parallélépipédique en carbure de silicium (SiC), un matériau à forte perte diélectrique à température ambiante. L'émissivité du SiC est d'abord mesurée en condition de corps noir, en suivant la procédure décrite dans le Chapitre 2. L'échantillon est ensuite placé dans une cavité monomode de 2,45 GHz. Quatre orientations différentes sont considérées. Après avoir ajusté la longueur de la cavité à la longueur de résonance à température ambiante, l'échantillon est chauffé avec une puissance constante de 50 W. Les simulations numériques, réalisées à l'aide du logiciel éléments finis *COMSOL multiphysics*® [23], ont consisté à résoudre un problème électromagnétique-thermique dans les mêmes conditions que dans la procédure expérimentale. Malgré les approximations faites dans la modélisation numérique (support isolant considéré comme transparent aux micro-ondes, paroi de la cavité considérée comme un conducteur parfait, pas de description de la cheminée), un bon accord entre les simulations et les résultats expérimentaux est trouvé pour les quatre orientations de l'échantillon. Les résultats montrent en particulier que le chauffage le plus efficace est obtenu lorsque l'échantillon est orienté le long du champ électrique. La sensibilité des résultats en fonction des paramètres matériaux a également été abordée. L'hypothèse d'un support isolant transparent aux micro-ondes (Hyp 1) est ensuite discutée. Bien que très peu de différence ait été trouvée dans le chauffage du SiC avec un support transparent ou non aux micro-ondes, les simulations des deux prochains chapitres considéreront que le support n'est pas totalement transparent. Cela peut avoir un impact sur le chauffage direct de l'alumine, qui couple moins par rapport au SiC.

Chapter 4

Microwave heating of alumina: influence of density

Contents

4.1 Introduction	78
4.2 Material and methods : Experimental	78
4.2.1 Dilatometric tests	78
4.2.2 Calibration of the pyrometer	81
4.3 Experimental results	82
4.4 Modelization of microwave heating of alumina at different density . . .	85
4.4.1 Density dependence of material parameters	86
4.4.2 Boundary conditions	89
4.4.3 Numerical results	89
4.5 Discussion	90
4.6 Conclusion	96

4.1 Introduction

This chapter presents the microwave heating study of pure alumina for different density level. The first part is dedicated to an experimental work. After presentation of samples preparation, pyrometer calibration and the experimental procedure, the direct microwave heating is introduced. Then, modelling using *COMSOL multiphysics*® [23] is performed assuming in a first approach that the evolution of physical parameters as function of temperature and density follows Effective Medium Approximation (EMA) [18]. Numerical simulations are also performed using the evolution of physical parameters from experimental data to compare simulation results with those of the EMA hypothesis and experiments.

4.2 Material and methods : Experimental

Two set of samples were prepared using a high purity alumina powder from BAIKOWSKI® [12] using conventional heating. First, cylinders are prepared to perform dilatometer tests during a sintering cycle, and hence to establish the density evolution as a function of temperature. Second, parallelepipeds with different densities are prepared to study microwave heating. The size of the latter samples is in the range of SiC samples studied in the previous chapter.

4.2.1 Dilatometric tests

Dilatometric tests allows us to measure the sample shrinkage and to evaluate the starting temperature of sintering during a thermal cycle. A Setaram dilatometer (Setsys 16/18) is used. This test is essential to define a thermal cycle in order to control the density level of a sample. Figure 4.1 presents the working principle of this dilatometer which is included in a conventional oven. The sample is laid down in an alumina support and an alumina feeler is brought into contact with the upper side of the sample. During a controlled thermal cycle, the feeler tracks the deformation of the sample which characterizes the sample evolution. It includes the shrinkage due to sintering and the thermal dilatation of the sample. Temperature is measured using a B type thermocouple ($T_{max}=1700$ °C) positioned below the sample. Dilatometric tests are preceded by a blank recording which allows to remove the thermal dilatation of all the equipment (feeler and support) on the measurements.

The dilatometric tests are performed on 8 mm diameter cylindrical samples. The samples are shaped in compacting the alumina powder into a cylindrical matrix using uni-axial press and in applying 100 MPa pressure. Before dilatometric measurements, a debinding thermal cycle is applied to the samples in order to eliminate the organic elements binding the powder. The debinding thermal cycle consists in a temperature increase at 1°C/min heating rate up to 600°C, this temperature is maintained for 60 min and it is followed by a cooling at 1°C/min cooling rate.

From dilatometric measurement, the evolution of the relative density of the sample can be derived, which needs the evaluation of densities before and after the thermal cycle.

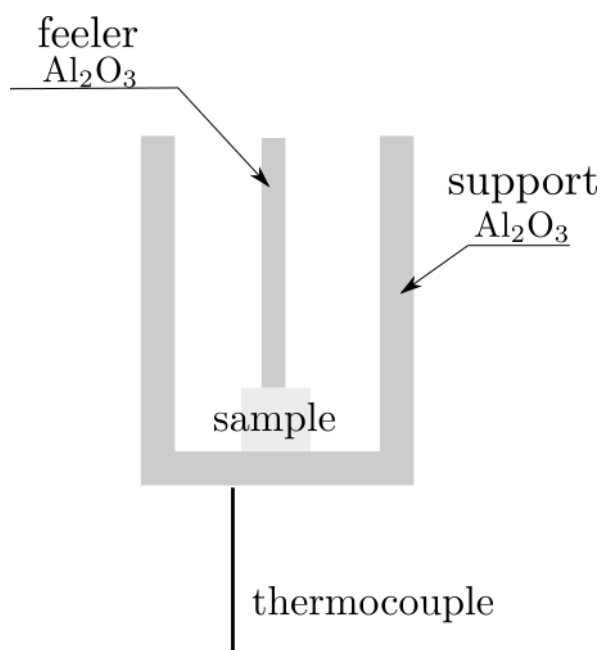


FIGURE 4.1 – Working principle of dilatometer.

4.2.1.1 Evaluation of the relative density

The relative density of a sample can be derived by either geometric method or Archimedes' principle.

- Geometric method

The relative density D is derived from the density $\bar{\rho}$ basically by measuring the mass (m) and evaluating of the volume (V) of the sample:

$$\bar{\rho} = \frac{m}{V} \quad (4.1)$$

The relative density refers to a perfectly densified sample of theoretical density $\bar{\rho}_{th}$. For alpha-alumina, the reference value is $\bar{\rho}_{th} = 3.987 \text{ g/cm}^3$. The relative density D is thus;

$$D(\%) = \frac{\bar{\rho}}{\bar{\rho}_{th}} \times 100. \quad (4.2)$$

The accuracy of the density depends mainly on the accuracy of the calculation of the sample volume, and thus on the description of its geometry. Indeed, the sample may presents some irregularities. In our case, the precision obtained on the relative density is estimated to be in the order of $\pm 1 \%$.

To minimize this inaccuracy, a method based on the Archimedes' principle is preferred for non powdery material as it does not necessitate evaluation of the volume.

- Archimedes' method

This method is based on the triple weighing of the sample. The mass is measured in the air, when the sample is immersed in a liquid (absolute ethanol here) and again in

the air but when the sample is impregnated with the liquid. The relative density can be expressed by the following relationship :

$$D(\%) = \frac{m_s}{m_h - m_i} \times \frac{\bar{\rho}_{ethanol}}{\bar{\rho}_{th}} \times 100 \quad (4.3)$$

where m_s is the mass of the sample weighted in the air, m_i is the mass weighted in the liquid and m_h the mass of the sample impregnated with ethanol weighted in the air.

Relative density accuracy obtained with the Archimedes' method depends on the porosity of the sample. For high porosity level, the accuracy is about $\pm 1\%$. Indeed, measurement of the impregnated mass depends on the drying of the sample after the immersed measurement. For low porosity level (densified material), the accuracy is in the order of $\pm 0.5\%$.

In the rest of this work, for low densities samples, the relative density is measured by the geometric method while the relative density of the sintered sample is measured using Archimedes' method.

4.2.1.2 Dilatometry results

Dilatometric tests were realized with the following thermal cycle: a temperature increase at $5^\circ\text{C} / \text{min}$ heating rate, a dwell time at 1600°C for 5 min followed by a cooling at $20^\circ\text{C} / \text{min}$. The relative density of the sample evaluated before and after the thermal cycle is 43.8 % and 97 %, respectively. From the dimension changes, we evaluated an anisotropic coefficient α [50] to take into account anisotropic effect on the evaluation of the density during the thermal cycle. The anisotropic coefficient is defined as followed:

$$\alpha = \frac{d_f - d_0}{d_0} \times \frac{h_f - h_0}{h_0} \quad (4.4)$$

where d_0 , d_f are the initial and the final diameters, h_0 and h_f are the initial and the final heights. The relative density during the thermal cycle can then be written as [50]:

$$D(t) = \frac{\left(1 + \frac{h_f - h_0}{h_0}\right) \times \left(1 + \frac{d_f - d_0}{d_0}\right)^2}{\left(1 + \frac{h(t) - h_0}{h_0}\right) \times \left(1 + \alpha \times \frac{h(t) - h_0}{h_0}\right)^2} \times \frac{\bar{\rho}_f}{\bar{\rho}_{th}} \quad (4.5)$$

where $\bar{\rho}_f$ is the final density.

Figure 4.2 presents the relative density as function of the temperature during the applied thermal cycle. It's shown that the sintering starts at 1373 K (1100°C), and the relative density increases from 43.8% (called green sample) to 97% (called sintered sample).

This dilatometric curve allows to define the thermal cycles in order to design samples with target densities. To study the density dependence of the microwave heating, parallelepipedic samples with a relative density of 43.8% (green sample), 55% and 97% were prepared. The samples are first shaped in compacting 5.28 g of alumina powder into a rectangular matrix of size $25 \times 9.1 \text{ mm}^2$ using uni-axial press and applying 50 MPa pressure. A conventional oven is then used to apply the thermal cycles.

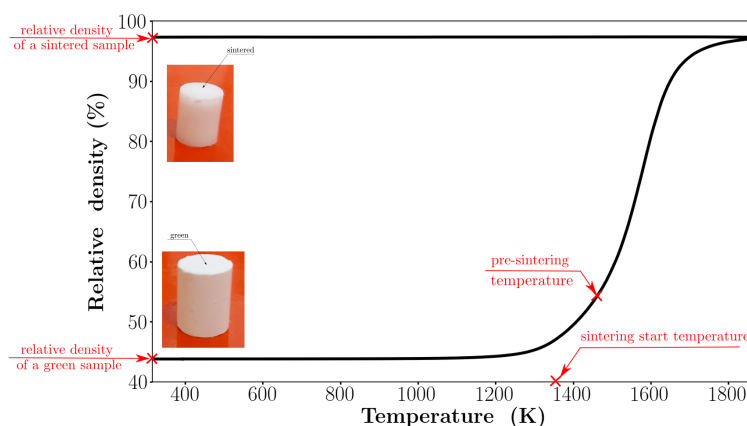


FIGURE 4.2 – Relative density evolution as a function of the temperature for alumina sample during thermal cycle.

- For 55% samples, the applied thermal cycle is composed of a heating at 5°C/min heating rate until 1200 °C followed by a cooling at room temperature.
- For 97% samples, the thermal cycle is composed by a heating at 5°C/min heating rate until 1600°C, a dwell time for 2 hours and a cooling at 5° C/min cooling rate.

To characterize the effect of the density and to avoid the effect of the sample size during microwave heating, the 43.8% and 55% samples, which have not the same size (see Figure 4.3), are rectified to correspond to the 97% sample size. Dimensions of the samples are then 9.5 mm × 7.5 mm × 19 mm.

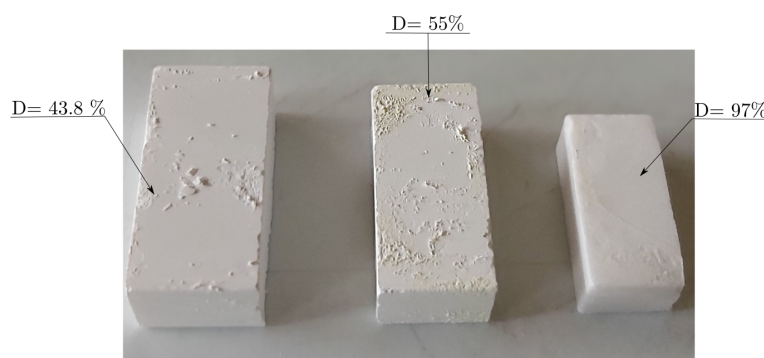


FIGURE 4.3 – Parallelepipedic samples with 43.8 % (left), 55 % (middle) and 97 % (right) relative density

4.2.2 Calibration of the pyrometer

Using the method presented in Section 2.2.2.2, the pyrometer is calibrated by determining the apparent emissivity of the alumina samples for the three different densities. Black body conditions are ensured by using alumina hollow cylinder with a height more than four time larger than its inner diameter. Figure 4.4 presents the apparent emissivity evolution of the three alumina samples in the temperature range [373 K - 1173 K].

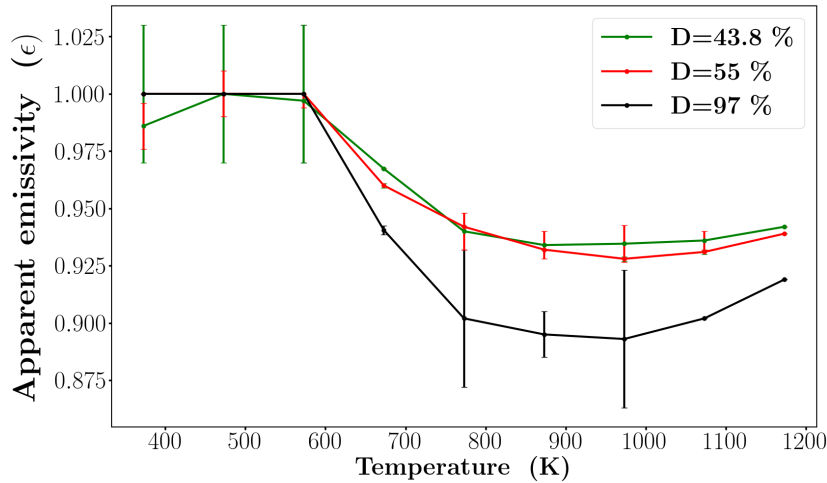


FIGURE 4.4 – Apparent emissivity of alumina samples with 43.8 %, 55 % and 97 % relative densities in the temperature range [373 K - 1173 K].

It is shown that the apparent emissivity is not very sensitive on the sample density. Its value is close to 1 at temperatures lower than 600 K and close to 0.92 at the highest temperatures.

Sensitivity to the apparent emissivity was tested during its determination. It appears that a shift of 0.05 in the apparent emissivity value implies a temperature deviation of 7 K. In the following, the pyrometer apparent emissivity is set to 0.95.

4.3 Experimental results

Microwave heating is performed using the same experimental set-up as presented in the previous chapter where 2.45 GHz TE₁₀₄ single mode cavity is used (Figure 2.6). During experiments, the sample is laid on the same insulating support used in the previous chapter to protect the cavity. Both are placed in a maximum of the electric field \mathbf{E} and the sample is orientated along the electric field direction (case 1 in the previous Chapter 3.2). We used the same procedure as in Chapter 3.

First, the resonant length of the cavity is determined manually at room temperature by minimizing the reflected power, adjusting the position of the short-circuit piston. Once this cavity length is found, the incident power is shutdown for the sample recovers ambient temperature. The cavity lengths for 43.8%, 55% and 97% relative densities samples are 344 mm, 343 mm and 341 mm, respectively.

Then, the heating experiment consists in applying a constant microwave power, keeping fixed the cavity length. During an experiment, the sample temperature and the reflected power are acquired.

In comparison to the SiC heating realized in the same conditions, a very different and more complex behavior is observed. Figure 4.5 presents the temperature evolution and the corresponding reflected power during the heating of a 55% relative density sample for 50 W power supplied. The experiment is repeated three times, taking care to wait a sufficient long time to recover the same initial state. This result shows that it is difficult

to have replicable experiments. However, the same tendency is observed on the three experiments and the temperature evolution is clearly correlated to the reflected power.

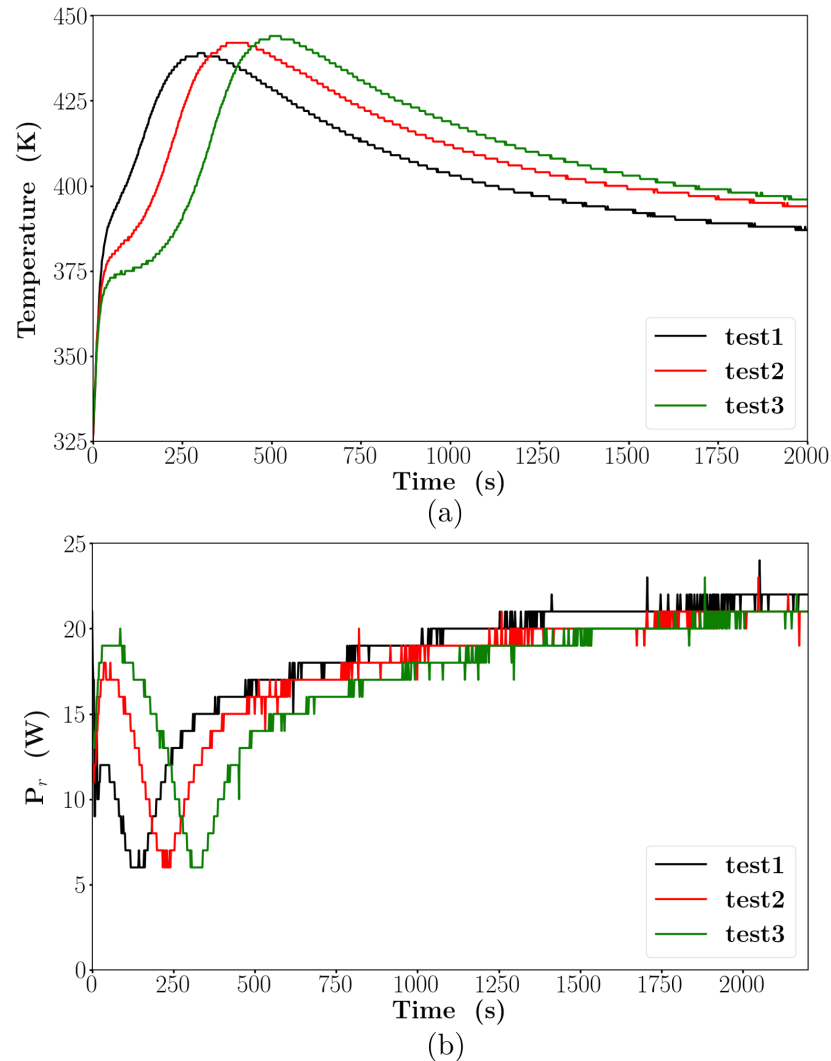


FIGURE 4.5 – (a) Temperature evolution and (b) the corresponding reflected power during the heating of a 55% relative density sample for 50 W power supplied.

The temperature evolution is characterized by a first fast increase of the temperature in the first moments of the heating, followed by a slowdown of the temperature increase to reach a temperature stage. Then, a second fast temperature increase is observed to reach a maximum before a slow cooling of the sample. A maximum temperature of 440 ± 5 K is reached in the range of 250s to 500s.

The reflected power is correlated to this temperature evolution and more particularly to the heating rate. It increases until a maximum which correspond to the slowdown of the temperature increase. Then, the reflected power decreases to reach a minimum during the second temperature increase. Finally, the reflected power increases again following a monotonous behavior that corresponds to the achievement of a maximum temperature and the slow cooling of the sample.

Figure 4.6(a) presents the comparison of the temperature evolution and the corresponding reflected power for 55% sample when applying 50 W and 100 W power supplied.

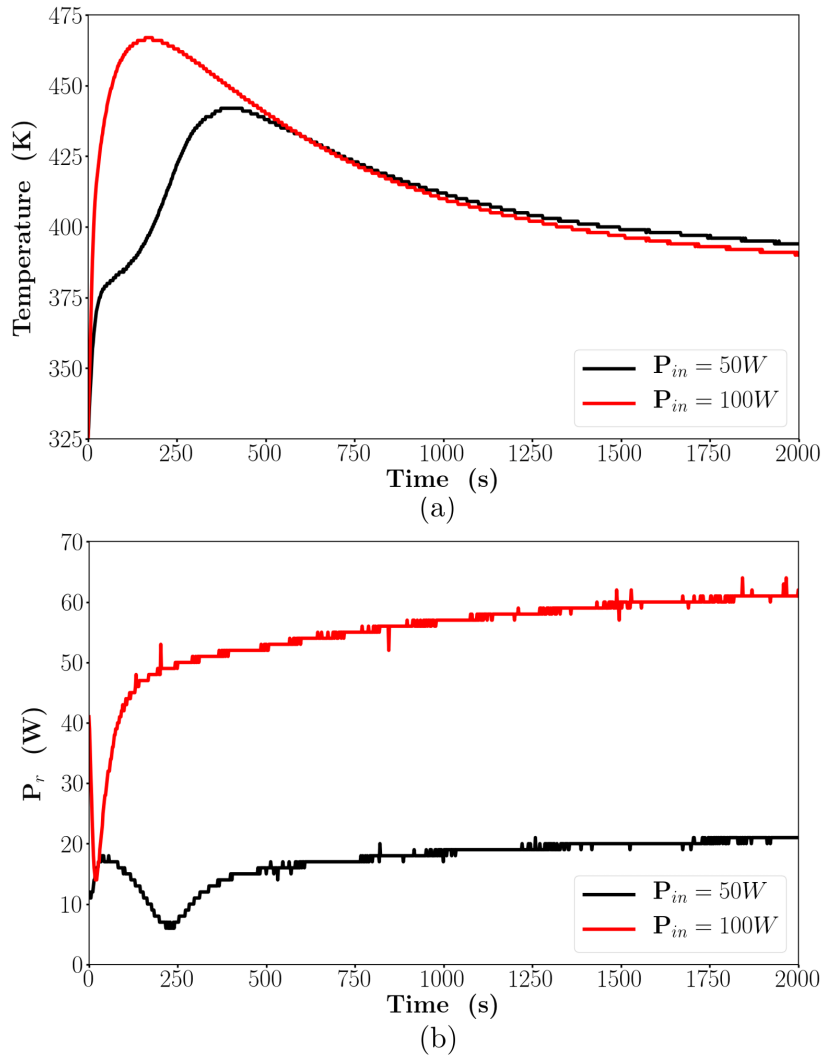


FIGURE 4.6 – (a) Temperature evolution of 55 % sample for 50 W and 100 W power supplied and (b) the corresponding reflected power.

For 100 W power supplied, a fastest and highest heating is produced and the same trend is observed on the reflected power evolution. The maximum temperature is also reached in two steps. The maximum temperature reached is 442 K at 400s and 467 K at 175s for 50 W and 100 W, respectively. It can be noted that no significant temperature gain is obtained by doubling the power supplied. The result is in accordance with the dielectric properties of alumina which is a low coupling material. Indeed, in comparison with SiC study where the final reflected power is in the range 1 to 20%, the final reflected power is in the order of 40-50 % in the case of alumina sample.

The temperature evolution for sample with 43.8 %, 55 % and 97 % relative densities and the corresponding reflected power for 50 W and 100 W power applied is presented in figures 4.7(a) to 4.7(d). For 50 W power applied (figure 4.7a), the maximum temperature reached is 480 K, 440 K and 325 K for 43.8%, 55% and 97% relative density samples, respectively. Note that the curve of the 97 % sample is not present and only peaks appear due to the available temperature range of the pyrometer.

Temperature and reflected power evolutions correspond to the previously observations except for 97% density. Indeed, the reflected power evolution is different as it shows

a monotonous behavior and its final value is significantly higher. In this case, it appears that the maximum temperature is reached at a shorter time compared to the other densities. This systematical effect at 50 W is not observed for 100 W power applied. The 50 W result clearly shows that the heating depends on the alumina density. The lower the density is the higher microwave heating efficiency is.

Figures 4.7b) and 4.7d) present the results for 100 W power applied where higher temperatures are reached in shorter times. The maximum temperature reached is 540 K, 467 K and 445 K for 43.8%, 55% and 97% samples, respectively. In each case, the reflected power increases at the beginning to reach a first maximum, then it decreases to reach a minimum before continuously increasing until the end of the experiment. Results with 100 W power applied confirm the dependence to the density of the heating efficiency. A better heating is observed for alumina samples with the lowest density.

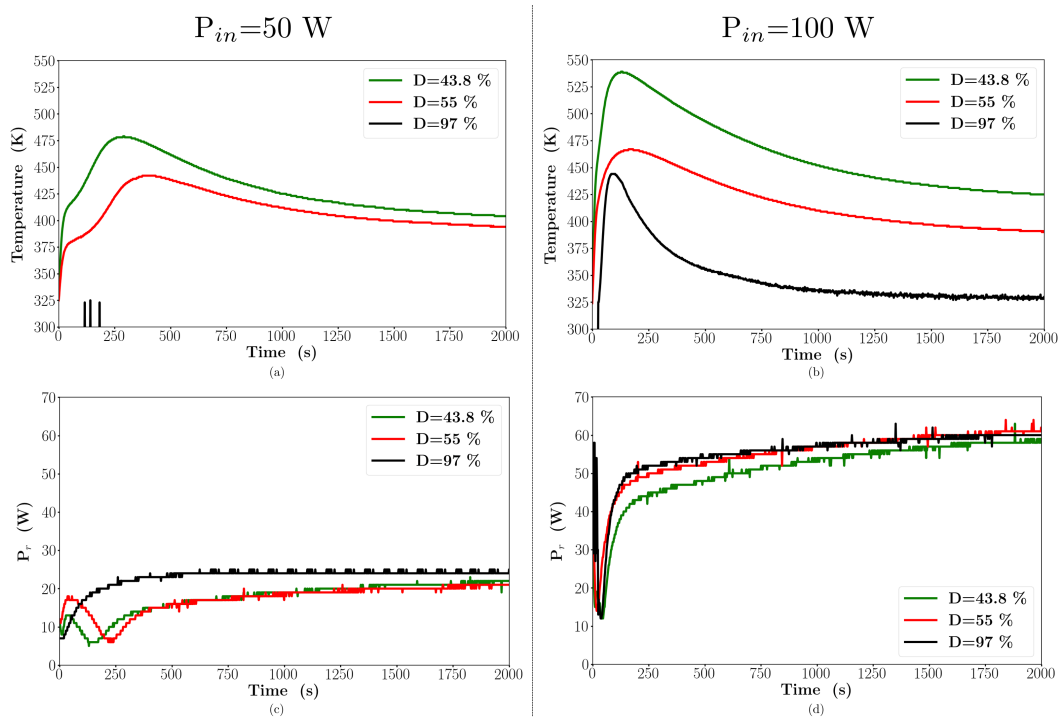


FIGURE 4.7 – Sample temperature and microwave reflected power during microwave heat for 50 W (left) and 100 W (right) power supplied of 43.8%, 55% and 97% samples.

The complex evolution of the sample temperature, correlated with the reflected power, is not understood at this stage. In the following, modelling is then used to explain the general trend of the observed temperature evolution.

4.4 Modelization of microwave heating of alumina at different density

This part is dedicated to the modelling of microwave heating of alumina with different relative densities. The aim of this work is to bring some answers on the experimental observations presented in the previous part. For that a 3D geometry using TE₁₀₄ single-mode cavity excited at 2.45 GHz is modelled (Figure 2.9).

4.4.1 Density dependence of material parameters

The physical properties of alumina as function of temperature can be found in the literature. However, it is much more difficult to find the evolution of properties as function of the density. First, we propose to derive the unknown physical parameters as a function of the density using the effective medium approximation (EMA). After showing the limits of this model, a second approach based on EMA parameters and experimental data is applied.

The temperature dependence of alumina physical properties can be found in the literature, the dielectric properties in the work of Marinel *et al* [59] and the thermal properties in [7]. The thermal properties and the dielectric properties of the insulating support (© RATH) are derived from the work of Manière *et al* [57, 56]. Note that the insulating support is not considered any more as transparent to microwaves in this part. Indeed, the insulating support material¹ is composed of a porous Al₂O₃ / SiO₂ mixture which has dielectric properties close to alumina. All material physical properties used are resumed in Appendix C.

4.4.1.1 Effective medium approximation

To deduce the alumina parameters as function of the density or relative density, we assume that the porous alumina is a composite material and the average properties depend on the volume fractions of each components. Here, the medium is made up of a volume fraction of solid phase (pure dense alumina) and a volume fraction of gas phase (air). The density dependence on a parameter is then deduced by applying a suitable mixing law. For heat capacity, a single volume mixing law is sufficient. Physical properties like the dielectric properties or the thermal conductivity are more difficult to treat [91].

Different algebraic mixing laws can be used to describe the dielectric properties as function of the relative density [36]. The effective medium approximation (EMA) originally proposed by Bruggeman [18] is used in this work. This approximation was used by Manière *et al.* to describe the 3Y-ZrO₂ [57, 58] and Ti-6Al-4V [56] (metal powder) dielectric permittivity as function of the relative density (D).

The principle of this approximation is to consider the medium composed of spherical inclusions with different properties (ε_i , $\overline{\rho}_i$, ...). Figure 4.8 presents an illustration of a medium within the EMA approximation. In this illustration, the effective medium (in grey) consists of two kinds of inclusions (black and white disks), the properties of the effective medium are deduced by solving the following relationship [91]:

$$\sum_i C_i \frac{\varepsilon_i - \varepsilon_{eff}}{\varepsilon_i + 2\varepsilon_{eff}} = 0 \quad (4.6)$$

where ε_i is the i th dielectric permittivity, ε_{eff} is the effective complex dielectric permittivity of the effective medium to be found and C_i is the volume fraction of the i th component, where the sum of all C_i is unity.

In the case of porous alumina, we assume the presence of two kinds of inclusions composed of gas (air in pores) and dense alumina. The effective dielectric parameters are

1. © RATH Altraform - <https://www.rath-group.com/>

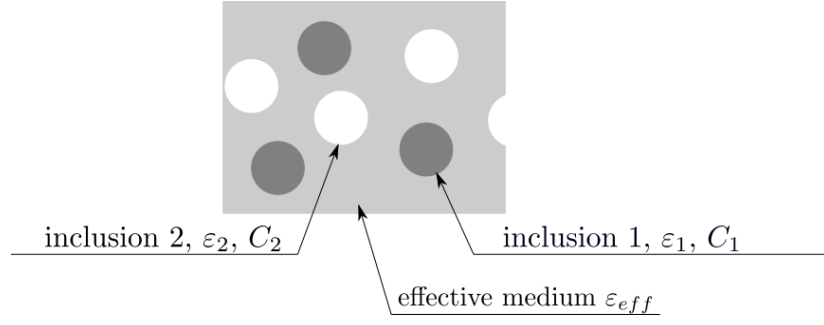


FIGURE 4.8 – Effective medium illustration [91].

thus given by the following relationship :

$$C_{Al_2O_3} \left(\frac{\epsilon_{Al_2O_3} - \epsilon_{eff}}{\epsilon_{Al_2O_3} + 2\epsilon_{eff}} \right) + C_{gas} \left(\frac{\epsilon_{gas} - \epsilon_{eff}}{\epsilon_{gas} + 2\epsilon_{eff}} \right) = 0 \quad (4.7)$$

where $\epsilon_{Al_2O_3}$ is the alumina complex dielectric permittivity, ϵ_{gas} is the gas complex dielectric permittivity, equal to 1, $C_{Al_2O_3}$ is the volume fraction of alumina and C_{gas} is the volume fraction of gas.

Note that the volume fraction of gas C_{gas} corresponds to the porosity and it refers to the relative density by the following relationship :

$$C_{gas} = \frac{V_{gas}}{V_{tot}} = 1 - D \quad (4.8)$$

where V_{gas} is the volume of gas present in the sample, V_{tot} is the total sample volume and D is the relative density.

The solution of the Equation (4.7), is solved for the relative density ranging from 0.4 to 1 and temperatures ranging from 300 K to 1800 K (see Appendix E for the demonstration). Figure 4.9 presents the real and the imaginary parts of the alumina relative permittivity as function of both temperature and relative density.

Within the EMA approximation, the real and the imaginary parts of the relative permittivity of alumina material increase from 3 at ($T=273$ K, $D=0.43$) to 10.8 at ($T=1873$ K, $D=1$) and from 5×10^{-4} at ($T=273$ K, $D=0.43$) to 0.08 at ($T=1873$ K, $D=1$), respectively.

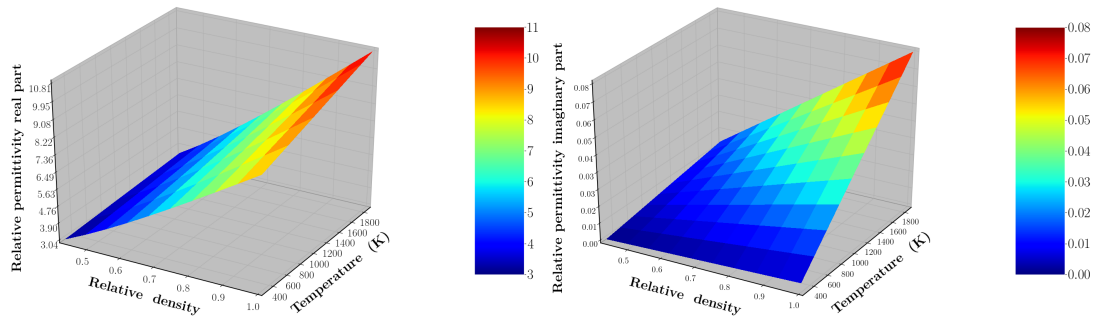


FIGURE 4.9 – Alumina relative permittivity as function of both temperature and relative density calculated by the EMA approximation (left) real part (right) imaginary part.

The thermal conductivity of porous alumina is also approximated by the effective medium approximation [91] by assuming that the thermal conductivity of pores is negligible ($\kappa_{air} = 0.025 \text{ W.m}^{-1}.\text{K}^{-1}$) in comparison to alumina matrix ($\kappa_{Al_2O_3} = 35 \text{ W.m}^{-1}.\text{K}^{-1}$). The density dependence of the thermal conductivity is then written as:

$$\kappa = \left(\frac{3}{2}D - \frac{1}{2} \right) \kappa_0 \quad (4.9)$$

where κ_0 is the thermal conductivity of the full-density material. Note that this relation is not valid for porous alumina with a low values of D , for instance relative density $D \leq 1/3$, the value of the thermal conductivity will be negative.

Neglecting the specific heat capacity of air in the pores [91], the specific heat of porous alumina writes as [91]:

$$C_p = DC_{p0} \quad (4.10)$$

where C_{p0} is the specific heat of the full-density material.

The different alumina parameters are represented as functions of the temperature in Figures 4.10 a)-d) for the densities of interest. To highlight the orders of magnitude of the different parameters, minimum and maximum values are presented in Table 4.1 for temperatures ranging from 300 K to 1500 K.

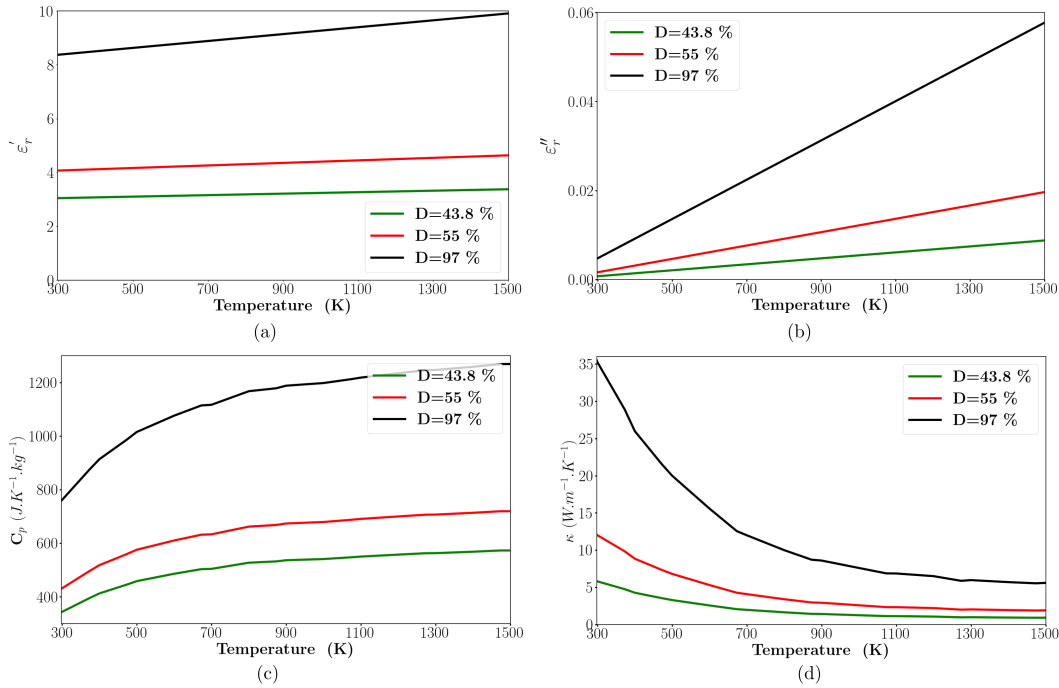


FIGURE 4.10 – Alumina parameter plotted as functions of temperature for three densities ($D=43.8\%$, $D=55\%$, $D=97\%$) in the range of the temperature [300 K - 1500 K] (a) relative permittivity real part, (b) relative permittivity imaginary part, (c) specific heat and (d) thermal conductivity.

TABLE 4.1 – Alumina parameter evolution for three densities ($D=43.8\%$, $D=55\%$, $D=97\%$) in the range of the temperature [300 K-1500 K].

	$D= 43.8 \%$	$D= 55 \%$	$D= 97 \%$
ε'	3-3.8	4.08-4.6	8.3-9.9
ε''	$6 \times 10^{-4} - 8 \times 10^{-3}$	$1.5 \times 10^{-3} - 1.9 \times 10^{-2}$	$4.7 \times 10^{-3} - 0.057$
C_p (J.kg $^{-1}$.K $^{-1}$)	343-573	431-720	761.5-1270
κ (W.m $^{-1}$.K $^{-1}$)	5.8-0.9	12-1.9	35-5.6

4.4.2 Boundary conditions

The same boundary conditions used for the SiC study presented in the previous chapter are prescribed for the EM problem. These boundary conditions are represented in Figure 2.11a. As mentioned before, alumina is a poor microwave absorber which has dielectric properties close to those of the insulating support. Consequently, the thermal transfer in both sample and in support has be carefully defined. The radiative and convective fluxes (Equations 2.25 and 2.26) are also considered at the insulating support boundaries.

Figure 4.11 presents the thermal boundary conditions for both Al_2O_3 sample and insulating support. At the sample/insulating support interface Γ_{cond} (blue line in Figure 4.11), the thermal conductivity is considered as the average of sample and insulating support conductivities.

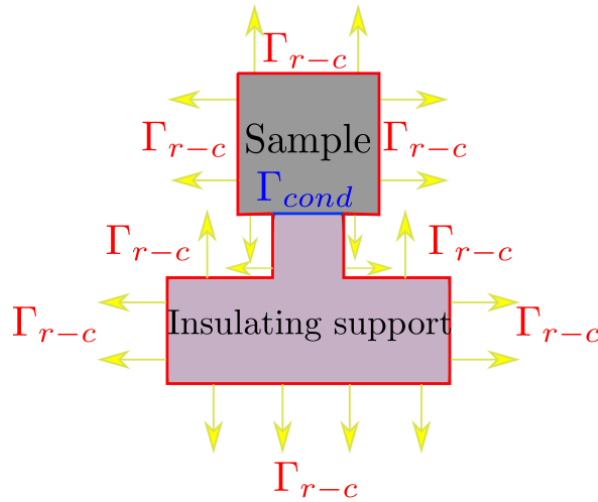


FIGURE 4.11 – Boundary conditions of the thermal problem used for Alumina microwave heating.

As in the previous chapter, the same mesh size (fine mesh) is used to solve the thermal and the EM problems with *COMSOL multiphysics*® [23]. Numerical results are presented in the next section.

4.4.3 Numerical results

In order to have a resonant system for each sample density, the length of the cavity is adjusted at room temperature to maximize the average electric field intensity in the sample. The simulation are done using 50 W applied power without considering the thermal

problem. Figure 4.12 presents the average intensity of the electric field in the alumina samples for the three densities ($D=43.8\%$, $D=55\%$ and $D=97\%$). At the maximum intensity, the system is considered to be resonant. The resonance is obtained for cavity lengths of 337.6 mm, 336.7 mm and 334.3 mm for $D=43.8\%$, $D=55\%$ and $D=97\%$ relative density, respectively.

The numerical results of the cavity length at resonance are smaller than the ones obtained experimentally (stars markers in Figure 4.12). Indeed, the experimental resonant cavity lengths are 344 mm, 343 mm and 341 mm for 43.8%, 55% and 97% relative densities, respectively. The density dependence is however respected as the more dense is the sample the more short is the length of the cavity. The observed differences are certainly due to the assumptions made in simulations: geometry (without description of the chimney), cavity walls considered as perfect electrical conductors.

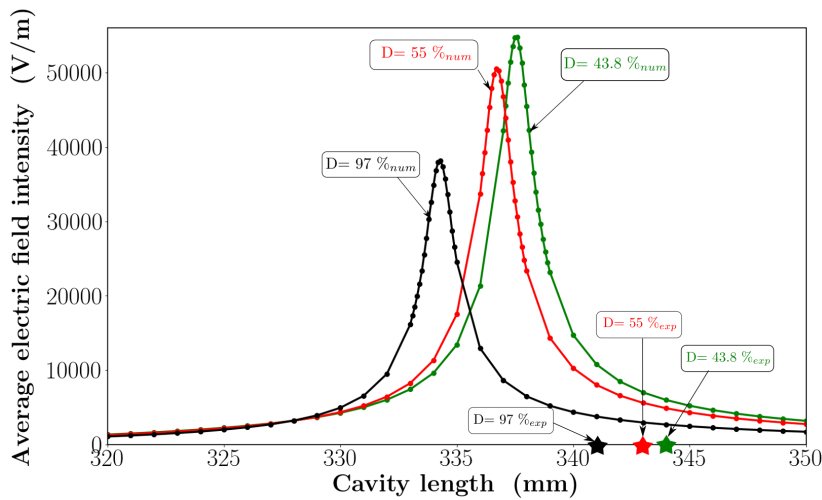


FIGURE 4.12 – Average intensity of the electric field obtained by simulation for different cavity lengths for the three densities ($D=43.8\%$, $D=55\%$ and $D=97\%$). Star markers correspond to the cavity lengths measured experimentally .

The heating of the different samples is simulated using 50 W applied power and a fixed cavity length. Figure 4.13 presents the evolution of the simulated temperature at the surface of the sample for the three relative densities. For each density, the temperature first increases continuously, until reaching a steady state. The maximum temperature is then 320 K at 260s, 350 K at 500s and 395 K at 2000s for the 43.8%, 55% and 97% samples respectively. This result is significantly different than the experimental observations. Indeed, the temperature increase in two steps is not observed, a reverse order in the density dependence of the heating efficiency is obtained and the temperature decrease at longer time is not described.

4.5 Discussion

- EMA approximation

The most remarkable discordance with experimental results concerns the heating efficiency order where a better heating is obtained for 97 % alumina. This is due to inability of

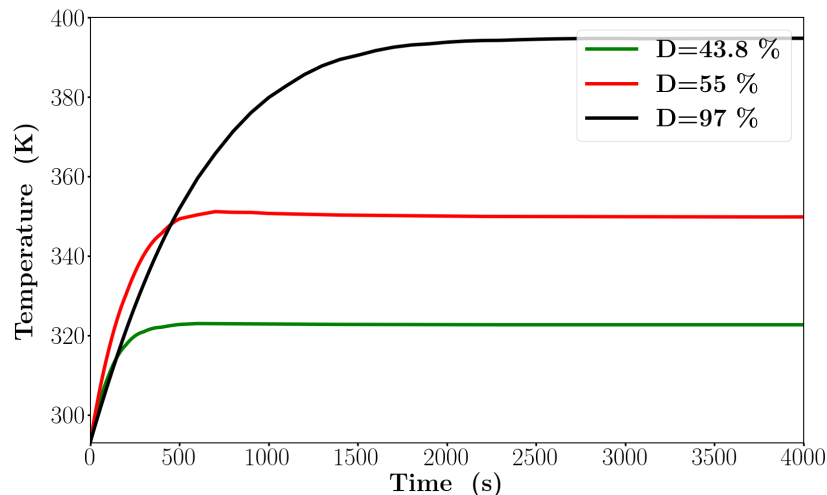


FIGURE 4.13 – Temperature evolution during microwave heating, for the three densities (43.8%, 55% and 97%), obtained by numerical simulation using EMA approximation.

EMA approximation to describe the experimental imaginary part of the porous alumina permittivity. Table 4.2 presents the comparison of complex permittivity of porous and sintered alumina samples found experimentally in the literature [36, 80] and predicted by EMA approximation. The order of magnitude for ϵ' as function of the relative density using EMA approximation is in accordance with the experimental results of Gershon *et al.* [36] and Penn *et al.* [80] for both porous and sintered samples.

For the imaginary part of the permittivity ϵ'' , the EMA prediction is in the contradiction with the experimental results [36, 80]. The imaginary part of the permittivity should increase when the density decreases.

TABLE 4.2 – Measured and predicted complex permittivity of porous and sintered alumina samples at ambient temperature.

	ϵ'	ϵ''
EMA ($D= 55\%$)	4.05	0.0012
Measured (Submicron sized $D= 55.5\%$ [36])	3.99	0.029
Measured (Micron sized $D= 59.3\%$ [36])	4.33	0.018
EMA ($D= 97\%$)	8.36	0.004
Measured (Submicron sized $D= 97.5\%$ [36])	8.82	0.0003
Measured (Micron sized $D= 96.8\%$ [36])	9.22	0.004
Measured (sintered polycrystalline alumina [80])	10	-

Simulations using the imaginary part of the permittivity deduced from experimental were then performed. Gershon's values [36] being limited to the densities $D= 55\%$ and $D=97\%$, we deduced values from the work of Penn *et al.* [80] who measured and successfully modeled the real part of the permittivity ϵ' and loss factor $\tan\delta$ as function of the porosity. The expressions of ϵ' and $\tan\delta$ in function of the relative density are given by the following expressions:

$$\epsilon' = \epsilon_m \left(1 - \frac{3(1-D)(\epsilon_m - 1)}{2\epsilon_m + 1} \right) \quad (4.11)$$

and

$$\tan\delta = D \tan\delta_0 + A'(1 - D) \left(\frac{1 - D}{D} \right)^{2/3} \quad (4.12)$$

where D is the relative density, $\epsilon_m = 10$ at ambient temperature for dense alumina material, $\tan\delta_0 = 1.565 \times 10^{-5}$ and $A' = 9.277 \times 10^{-3}$.

Using Equation (4.11), Equation (4.12), and Equation (1.9), the new values of ϵ'' calculated for the three relative densities ($D=43.8\%$, $D=55\%$ and $D=97\%$) are presented in the Table 4.3.

TABLE 4.3 – New values of the imaginary part of the permittivity of alumina materials.

	$D=43.8\%$	$D=55\%$	$D=97\%$
ϵ''	0.017	0.015	0.0004

The previous simulations are now carried out using the new ϵ'' values. The resonant cavity lengths are not affected by this change. The cavity lengths maximizing the average of the electric field in the sample are 344 mm, 343 mm and 341 mm for $D=43.8\%$, $D=55\%$ and $D=97\%$, respectively. The microwave heating is then simulated for the three densities with constant dielectric parameters values (not as functions of the temperature) whereas the thermal parameters (C_p and κ) depend on the temperature (Appendix C).

Figure 4.14 presents the temperature evolution during microwave heating for $D=43.8\%$, $D=55\%$ and $D=97\%$ using the new values. The most efficient heating is obtained with the lowest density $D=43\%$, followed by the intermediate one $D=55\%$. For $D=97\%$, the sample does not heat up: a temperature increases of only 0.2 K is observed. These results are in agreement with the experiences where the more porous sample is, the more efficient heating is. The complex experimental temperature evolution are however not obtained.

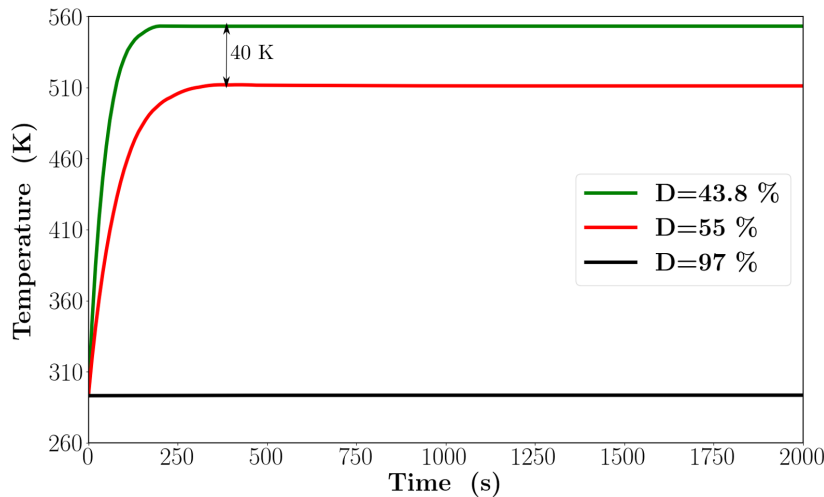


FIGURE 4.14 – Temperature evolution during microwave heating for $D=43.8\%$, $D=55\%$ and $D=97\%$ using the new values.

Results show also that the steady temperature is reached in a shorter time for $D=43.8\%$. This result is in agreement with experimental measurements. It correlates with the results presented in Figure 3.12b). The lower specific heat C_p value is, the faster the maximum temperature is reached.

To tackle the thermal exchanges between the insulating support and the sample that may be at the origin of the experimental temperature evolution in two steps, we proposed to change the boundary condition of the insulating support.

- **Effect of the boundary condition on the insulating support**

Considering a sample with a relative density $D = 43.8\%$, we force the insulating support to only exchange temperature with the sample. It means the thermal exchange between the insulating support and the air is impossible. Figure 4.15 shows the location of these thermal insulating conditions by black lines.

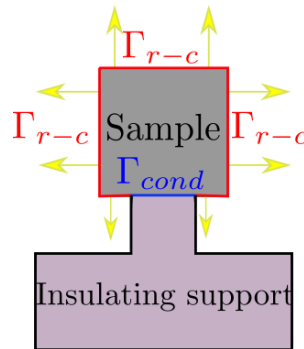


FIGURE 4.15 – Thermal boundary conditions while considering all the boundary of the insulating support are thermal insulating.

For 50 W power applied, the Figure 4.16 presents the temperature evolution in the sample and in the insulating support with this new boundary conditions. The inset in

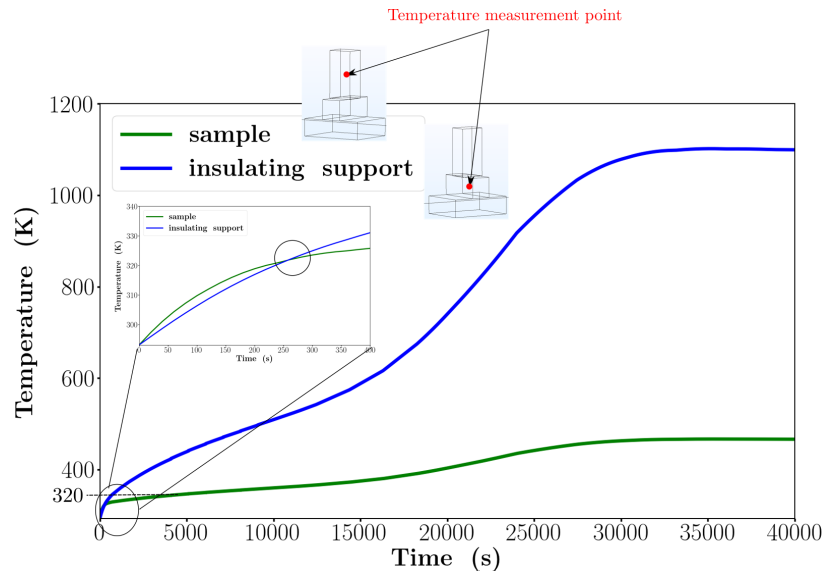


FIGURE 4.16 – Temperature evolution during microwave for the $D=43.8\%$ alumina sample and the insulating support, measured at the red point, while considering all the boundary of the insulating support are thermal insulating.

Figure 4.16 shows that the heating of the sample is more important at shorter times, *i.e.* for a time lower than 250s. For longer times, the temperature of the insulated support exceeds the sample temperature. A temperature increase in two steps is then observed

for both the insulating support and the sample. This temperature evolution corresponds to the experimental observation at shorter times.

Regarding the sample temperature evolution, this result shows that the first increasing step is due to the direct microwave heating of the sample. The second one is due to thermal exchange between the insulating support and the sample. The insulating support, which has permittivities close to alumina, has an important role on the complex thermal behavior observed. This simulation tends to show that it is responsible of the second temperature increase. Furthermore, we suspect that the decrease in the temperature of the sample once the maximum is reached (Figure 4.7) is due to the heating of the cavity walls, which detunes the cavity. This effect cannot be taken into account in the simulation here.

• Further experiments

To highlight these behaviors, we performed two experiments using a sample made of insulating support material (©RATH) with the same dimensions of alumina samples. It ensures that the sample and the insulating support have the same physical properties. A first, an experiment is conducted at room temperature (without air cooling). Second, an experiment is conducted in cooling the cavity with an air cooling system. For both experiments, 100 W power supplied is applied.

Figure 4.17 presents the temperature evolution and the reflected power during these experiments. In the first moments of both experiments, the slowing down of the temperature increase is no longer observed, contrary to the alumina © RATH previous case in Figure 4.7. Consequently, the corresponding reflected power does not present any fluctuations and increases monotonously. This result means that the insulating support and the sample made of the same material heat uniformly.

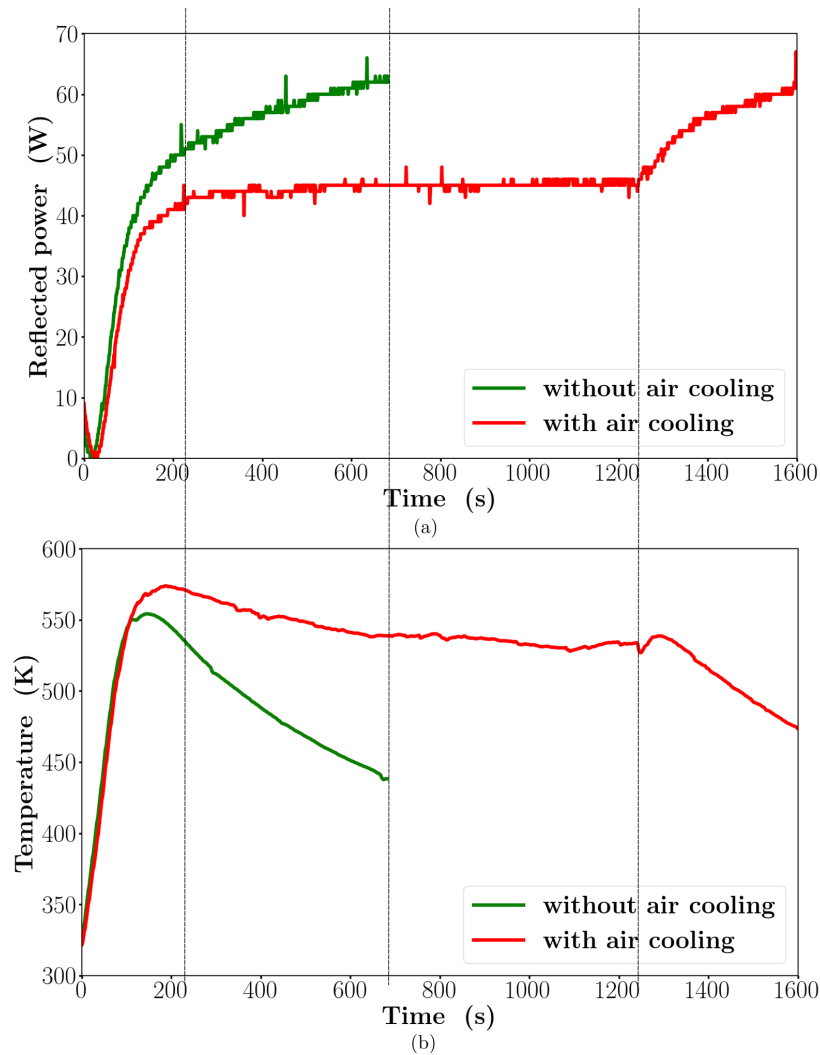


FIGURE 4.17 – (a) Temperature evolution and (b) reflected power during microwave heating with and without air cooling using a sample made of ©RATH.

After the sample reaches a maximum temperature, we show the same cooling behavior observed when the sample is made of alumina. The temperature decrease is higher for the experiment realized at room temperature (without air cooling) than the case where the cavity is cooled.

In the experiment with air cooling, when the air cooling system is switched off at 1250 s, we observe a fast decrease of the sample temperature and the corresponding reflected power increases. This fact clearly indicates that the cavity temperature has a huge influence on the sample temperature at long term as it has been shown in all the experiments using alumina samples.

This effect is not present in the case of the SiC sample which is a good absorber material. For low absorber materials as alumina or silica-alumina materials, a significant part of the EM energy is dissipated in the cavity walls, which are heated, detuning the resonant system. This effect degrades the heating efficiency of the sample.

4.6 Conclusion

This chapter has presented the experimental and the numerical results on the microwave heating of parallelepipedic alumina samples with three different densities ($D=43.8\%$, $D=55\%$ and $D=97\%$). In the experimental part, the calibration of the pyrometer used to measure the temperature shows that the apparent alumina emissivity is not very sensitive to the alumina density. The heating of the different samples is then performed using a 2.45-GHz single-mode cavity. After adjusting the length of the cavity to find the resonant length at room temperature, the alumina samples are heated using 50 W and 100 W power supplied. The results show a complex evolution of the sample temperature. The heating of the sample occurs in two steps until a maximum temperature followed by a cooling stage. It is also observed that the lower is the sample density, the higher is the heating efficiency.

To analyse the experimental results, simulations with *COMSOL multiphysics*® [23] were performed. In a first approach, simulations are carried out using the density dependence of alumina physical parameters of alumina obtained within the effective medium approximation. The results show that this approximation is limited to predict the imaginary part of the permittivity: the heating efficiency found as a function of density is in contradiction with the experiments. The experimental tendency is however recovered by using data from experimental permittivity measurements ϵ'' . From simulations, exhibited the importance of the heat transfer from the insulating support to the sample that causes the second temperature increase observed experimentally. It appears that the insulating support heat as much as the sample. The cooling of the sample, observed experimentally, is not recovered by the modelling due to the assumptions made. Indeed, the overall experimental set-up is not modelled. To understand the initial experimental observations, additional experiments with a sample made of insulating material were performed. From these additional experiments, we concluded that the insulating support is at the origin of the initial two step temperature increase and also that the final cooling is due to the temperature increase of the cavity.

Résumé en Français :

Ce chapitre a présenté les résultats expérimentaux et numériques sur le chauffage par micro-ondes d'échantillons d'alumine parallélépipédique avec trois densités différentes ($D=43.8\%$, $D=55\%$ et $D=97\%$). Dans la partie expérimentale, la calibration du pyromètre utilisé pour mesurer la température montre que l'émissivité apparente de l'alumine est peu sensible à la densité de l'alumine. Le chauffage des différents échantillons est ensuite réalisé à l'aide d'une cavité monomode de 2,45 GHz. Après avoir ajusté la longueur de la cavité pour trouver la longueur de résonance à température ambiante, les échantillons d'alumine sont chauffés en utilisant des puissances fournies de 50 W et 100 W. Les résultats montrent une évolution complexe de la température de l'échantillon. Le chauffage de l'échantillon se fait en deux étapes jusqu'à une température maximale suivie par un refroidissement. On observe également que plus la densité de l'échantillon est faible, plus l'efficacité du chauffage est élevée.

Pour analyser les résultats expérimentaux, des simulations avec *COMSOL multiphysics*® [23] ont été réalisées. Dans une première approche, les simulations sont effectuées en utilisant la dépendance en densité des paramètres physiques de l'alumine donnée par l'approximation du milieu effectif. Les résultats montrent que cette approximation est limitée pour la prédiction de la partie imaginaire de la permittivité. En effet l'efficacité du chauffage trouvée en fonction de la densité est en contradiction avec les résultats expérimentaux. La tendance expérimentale est cependant retrouvée en utilisant les données des mesures expérimentales de la permittivité ϵ'' . Les simulations ont montré l'importance du transfert de chaleur du support isolant vers l'échantillon qui provoque la seconde augmentation de température observée expérimentalement. Il apparaît que le support isolant chauffe autant que l'échantillon. Le refroidissement de l'échantillon, observé expérimentalement, n'est pas décrit par la modélisation en raison des hypothèses faites. En effet, l'ensemble du dispositif expérimental n'est pas modélisé. Pour comprendre les observations expérimentales initiales, des expériences supplémentaires avec un échantillon en matériau isolant ont été réalisées. De ces expériences supplémentaires, nous avons conclu que le support isolant est à l'origine de l'augmentation de température initiale en deux étapes et que le refroidissement final est dû à l'augmentation de température de la cavité qui désaccorde celle-ci.

Chapter 5

Towards the simulation of microwave sintering in hybrid configuration

Contents

5.1 Introduction	100
5.2 Microwave sintering	100
5.2.1 Experimental set-up	100
5.2.2 Development of the sintering cell	101
5.2.3 Thermal cycle	104
5.3 Numerical simulations	108
5.3.1 Computational domain	108
5.3.2 Numerical model and boundary conditions	108
5.3.3 Material parameters	111
5.4 Numerical results and discussion	111
5.5 Conclusion	114

5.1 Introduction

This last chapter presents a prospective work on microwave sintering of alumina in hybrid configuration, from both experimental and modelling/simulation point of view. As shown in the previous chapters, the low permittivity of alumina at room temperature does not allow to reach the sintering temperature ($\sim 1600 - 1700$ K) with microwave irradiation alone. Consequently, high permittivity susceptors, *i.e.* SiC susceptors in this study, have to be used in a single mode microwave cavity to heat the alumina by radiation, at least until the permittivity of the alumina reaches a sufficient value. This point will be discussed in this chapter. This experimental work was carried out at the CRISMAT laboratory in Caen. Indeed, this laboratory has equipment that is not available at Mines Saint-Étienne: a magnetron generator delivering an incident power of more than 1000 W slaved by a PID (Proportional Integral Derivative) controller, an automated short-circuit piston and an infrared camera. The modelling of this experimental set-up is more complex than the modelling presented in the previous chapters: two interacting materials, SiC and Al_2O_3 , have to be taken into account, as well as the shrinkage of alumina. An additional complexity also appears in *COMSOL*® [23] simulations: PID controller of the delivered power, application of the piston motion, and shrinkage of the sample.

5.2 Microwave sintering

5.2.1 Experimental set-up

Figure 5.1 shows the experimental set-up used in the CRISMAT laboratory: a magnetron generator at 2.45 GHz, a microwave cavity, delimited on one side by an iris (allowing the entry of the incident wave coming from the generator and the reflection of the wave already reflected by the piston), and on the other side by a moving short-circuit piston. Some differences with the equipment used in Mines Saint-Étienne can be mentioned. First, the waveguide is dimensioned for a TE_{105} mode, which means five maxima of the electric field in the z -direction, instead of four in our laboratory. Second, the presence of an impedance matching device composed of three stubs. By changing their positions, it is possible to cancel the reflected power. This system is of great interest for the direct sintering of alumina with low incident power (a few hundred watts). In this work, in order to limit the number of varying parameters, these stubs are kept fixed. Finally, as mentioned in the introduction, the motion of the short circuit-piston is automated, while the delivered power can be prescribed using a PID, according to the target temperature to be reached.

Two cylindrical chimneys can also be seen in Figure 5.1. They allow the measurement of both the temperature of the susceptors and that of the sample, using a FLIR A655sc [32] infrared camera (see Table 2.4 for technical specifications) and an IRCON [68] 5G-2024 monochromatic pyrometer (see Table 2.3). Note that the pyrometer points to the sample being sintered and provides the temperature for PID power control. In addition, due to space constraints, the pyrometer does not point directly at the sample, but through a reflecting mirror. This should be taken into account when calibrating the pyrometer.

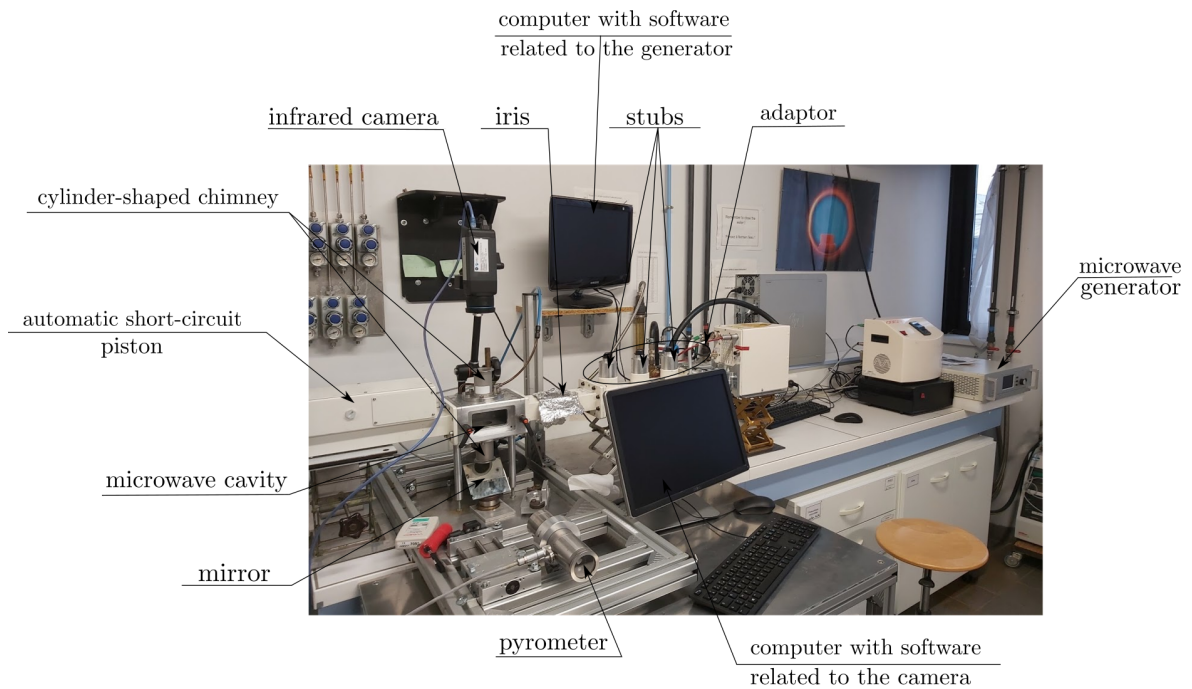


FIGURE 5.1 – Experimental set-up at CRISMAT laboratory.

5.2.2 Development of the sintering cell

5.2.2.1 Choice of susceptor configuration

The effect of the orientation of a parallelepipedal SiC sample in the electric field was studied in Chapter 3. The “case 1” configuration in Figure 3.2, where the sample is “aligned” in the (\mathbf{E}, \mathbf{k}) plane, was found to be the most suitable to achieve high temperatures. This is also the orientation chosen here. As the permittivity of alumina is low for “low” temperatures, this material cannot reach the sintering temperature by itself under microwave irradiation. Therefore, SiC susceptors initiate the temperature rise, heating the sample by radiation.

In the literature, several works investigate, both numerically and experimentally, the effect of the shape of the sample/susceptor pair on heating and sintering: SiC box or ring in [27], where the ring was finally retained for a cylindrical sample; SiC plates with a hexagonal sample in [59] under 2.45 GHz, or with a square sample in [52] under 915 MHz. The effect of the orientation of the sample/susceptor pair in the electric field, is also studied in these references, with two possible configurations: parallel or perpendicular.

In this work, the orientation of the alumina sample is already chosen and corresponds to case 1 orientation (Figure 3.2). The susceptors are two SiC plates, whose orientation is either “perpendicular” to the (\mathbf{E}, \mathbf{k}) plane in the sense of Figure 5.2a), or “parallel” to this plane as in Figure 5.2b). The most suitable orientation is determined numerically, solving only the electric field transport equation at room temperature (293 K), with an incident power of 800 W and considering the cavity walls as perfect electric conductors. The material properties of alumina and SiC, are presented in Appendix C.

Figure 5.3 presents the electric field distribution obtained with the two configurations, in the vicinity of the sample/susceptor system.

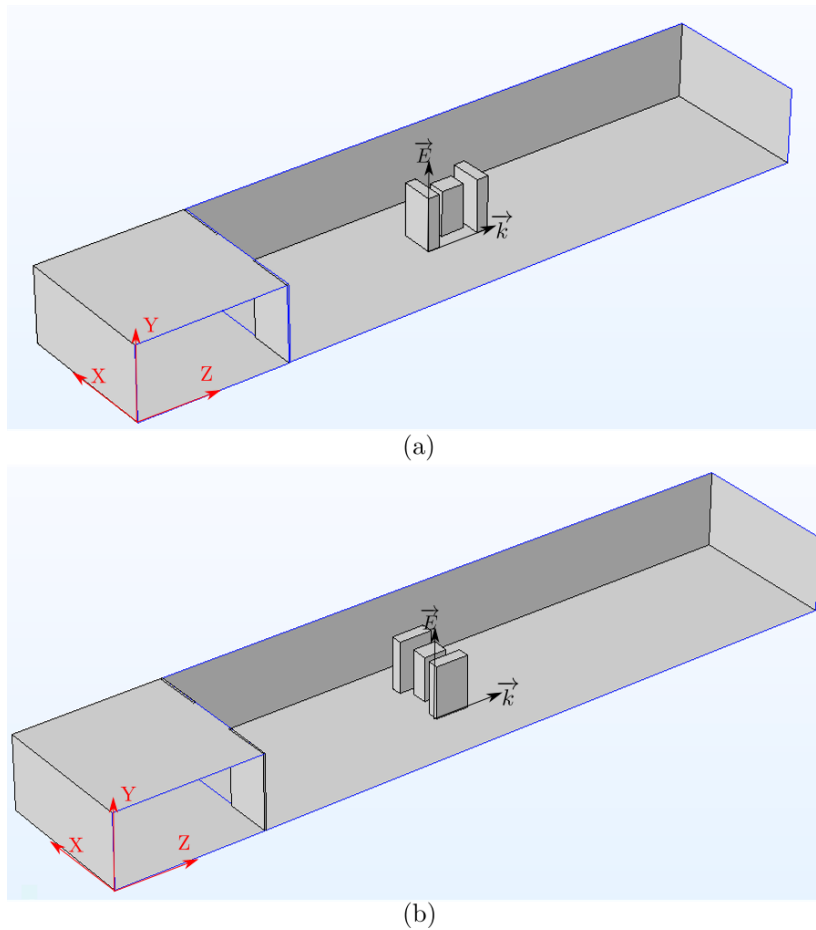


FIGURE 5.2 – Studied configurations: a) perpendicular configuration, b) parallel configuration.

With the perpendicular configuration (Figure 5.3a)), the electric field intensity is higher in the SiC plate facing the generator than in the one facing the piston. This non-homogeneity should lead to thermal gradients during the heating, *i.e.* a non-uniform temperature in the sample. On the contrary, with the parallel configuration the electric field is homogeneous in the system (Figure 5.3b)), which should lead to a more uniform heating. Consequently, the latter configuration is chosen for this work.

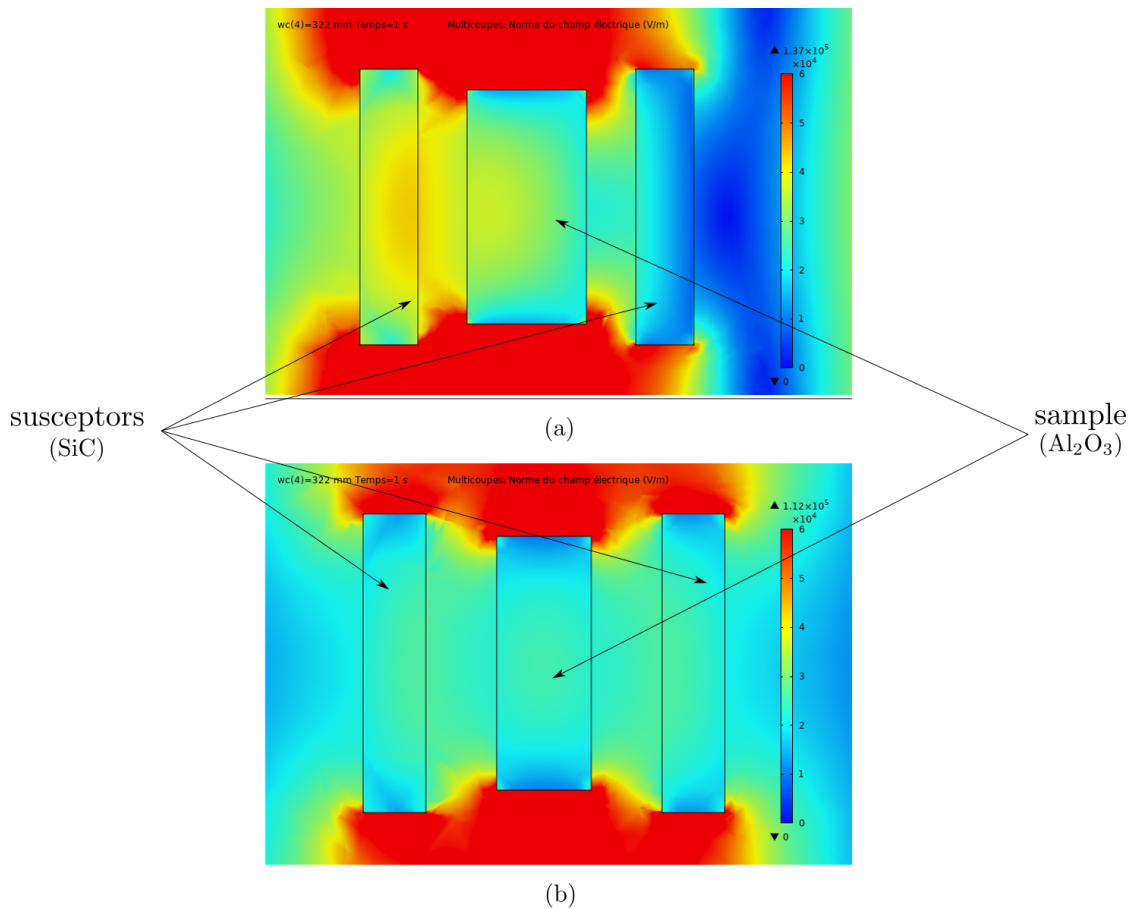


FIGURE 5.3 – Electric field distribution in both sample and susceptors for a) perpendicular configuration and b) parallel configuration.

5.2.2.2 Sintering cell

The alumina sample to be sintered was shaped according to the method detailed in Chapter 4, Section 4.2.1.2, with dimensions 25 mm × 13 mm × 9.1 mm and an initial relative density $D = 43\%$. The two SiC plates have dimensions 30 mm × 18.6 mm × 6.3 mm in order to cover the whole sample. Their corners were rounded by polishing to avoid any tip geometry effect, which favours plasma formation.

Figure 5.4 presents the sintering cell: the system, consisting of the two susceptors and the sample on a © RATH support, is placed in a thermal insulation box, also made of © RATH. A small hole is drilled in the bottom of this box for the measurement with the pyrometer. Similarly, a thin slot is made on the top for the infrared camera. This camera is calibrated with an emissivity of 0.95, the value found in Chapter 4, Section 4.2.2, and records both the “temperature” of the sample (Box 1 in photograph of Figure 5.4) and the susceptors (Box 2 and 3).

Finally, note that since the pyrometer points to a mirror and not directly the sample, an emissivity of 0.5 was used for its calibration. With this value, camera and pyrometer provide the same temperature.

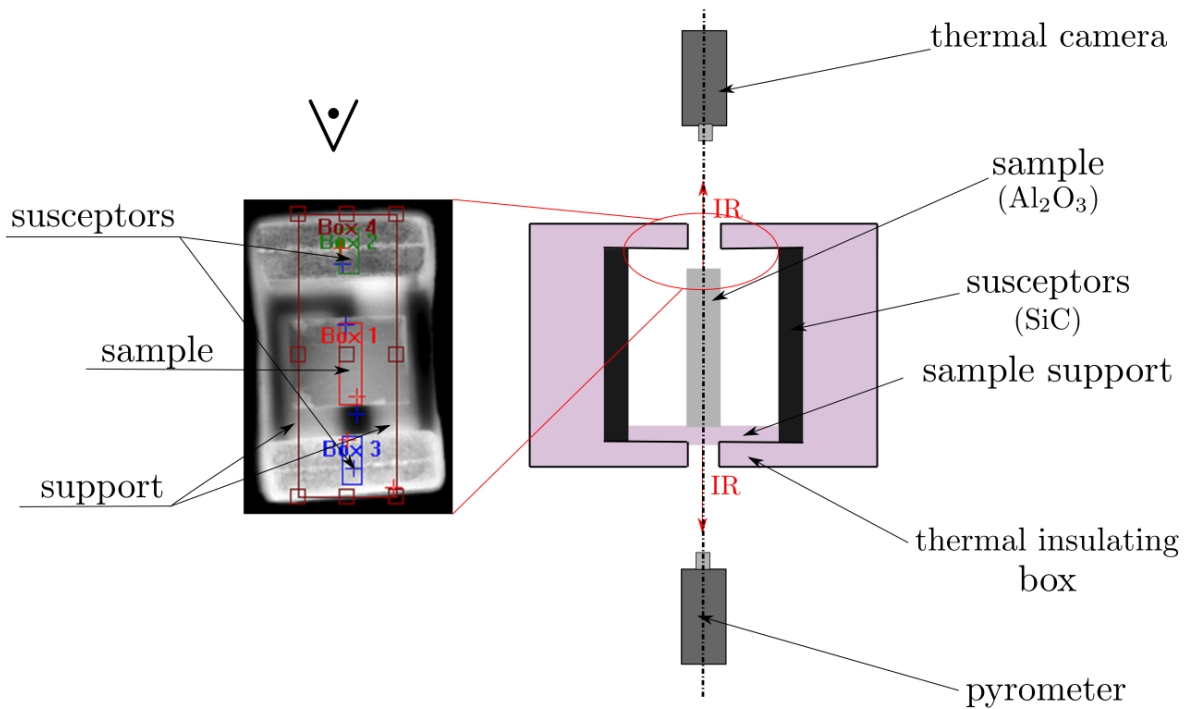


FIGURE 5.4 – Cell sintering: an explanatory scheme with a photograph of the thermal camera.

5.2.3 Thermal cycle

Different tests were necessary to determine a suitable thermal cycle to achieve a dense sample, with a final relative density $D = 97\%$. In particular, plasma formation was observed for a dwell temperature of 1873 K (1600°C), despite the rounding of the SiC plates (Figure 5.5). In order to avoid this problem, a dwell temperature of 1773 K (1500°C) was chosen, which is sufficient for alumina sintering.

Figure 5.6 shows the thermal cycle finally used. The temperature ramp is deliberately moderate to avoid any cracking of the sample. For the temperature decrease, the microwave generator is switched off and the sample cools down naturally. In this figure, it can also be seen that the temperature measured by the pyrometer at the bottom of the sample strictly follows the prescribed thermal cycle (black dotted line), as a result of the PID adjustment of the delivered incident power. This power denoted P_{in} is plotted over time in Figure 5.7, along with the reflected power P_r and the piston position PCC. In the early stages of heating, P_{in} is adjusted by the PID in order to find the prescribed temperature, accounting two peaks up to 1200 W, before to vary between 320 W and 1270 W during the cycle. The reflected power is first stabilised at 220 W, can be considered constant until 2000s, and then increases to 1000 W. The piston moves to minimise this reflected power. However, most of the incident power is reflected, and therefore not absorbed by the system: 30% of the power is absorbed just after the PID adjustment, and 20% at the end of the cycle. It can be hypothesised that this power is only absorbed by the SiC susceptors, which in turn heat the alumina by radiation. This will be discussed in the simulation section. Note that the reflected power could probably be minimised if stubs were used.

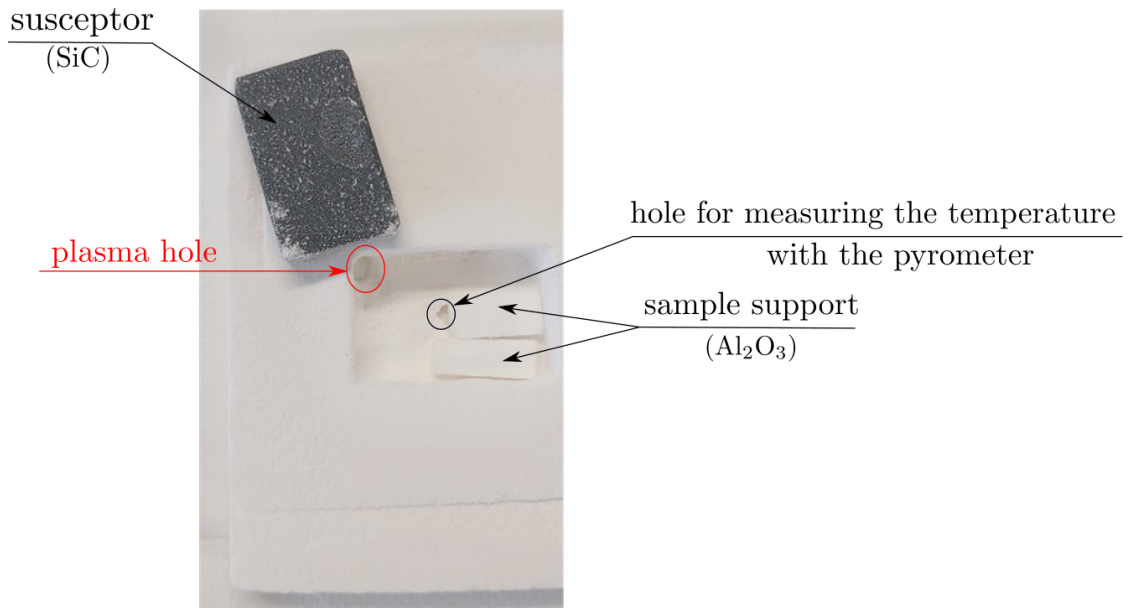


FIGURE 5.5 – Photograph of the plasma phenomenon.

The sample temperature values measured throughout the cycle, with both the pyrometer and the infrared camera are shown in Figure 5.8a). Figure 5.8b) presents the maximum temperature measured by the thermal camera, for both the sample and the susceptors. As expected, the susceptors have a higher temperature, and therefore heat the sample. When the dwell temperature is reached, the thermal system is in a steady state: sample and susceptors are at the same temperature.

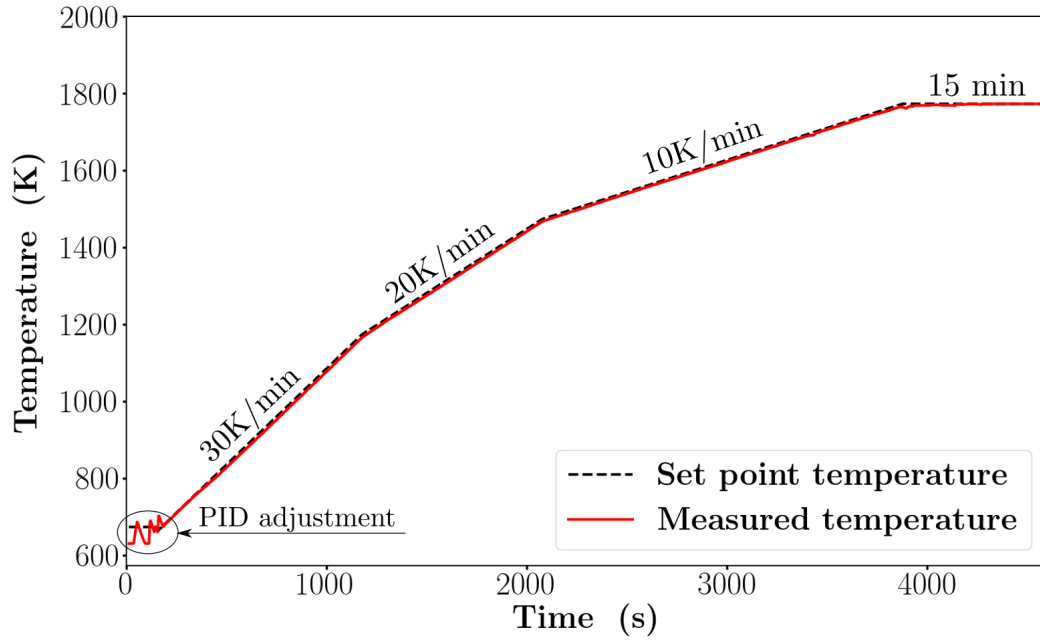


FIGURE 5.6 – Applied thermal cycle.

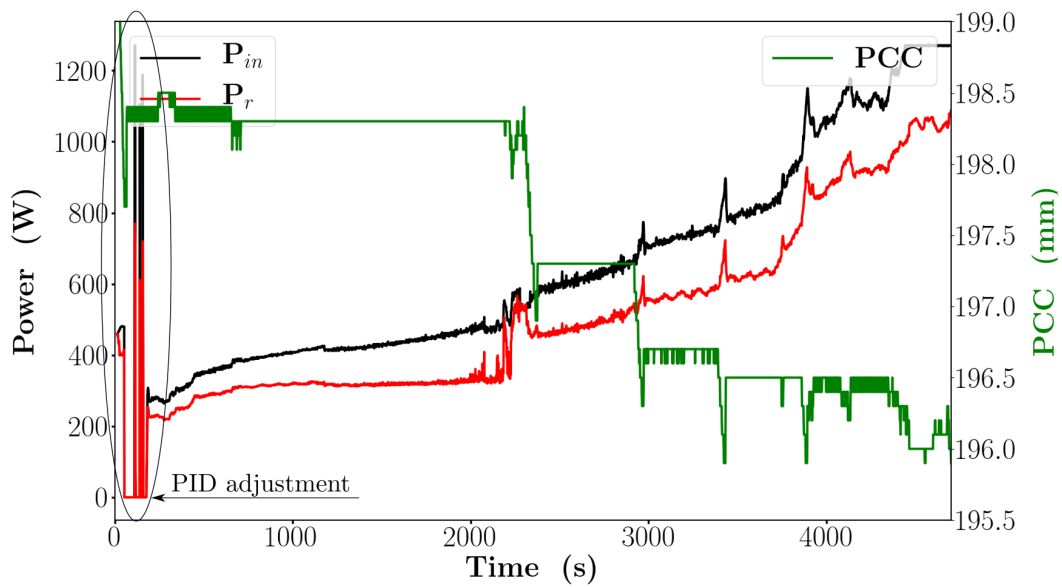


FIGURE 5.7 – The evolution of the incident, the reflected power and the piston position (PCC).

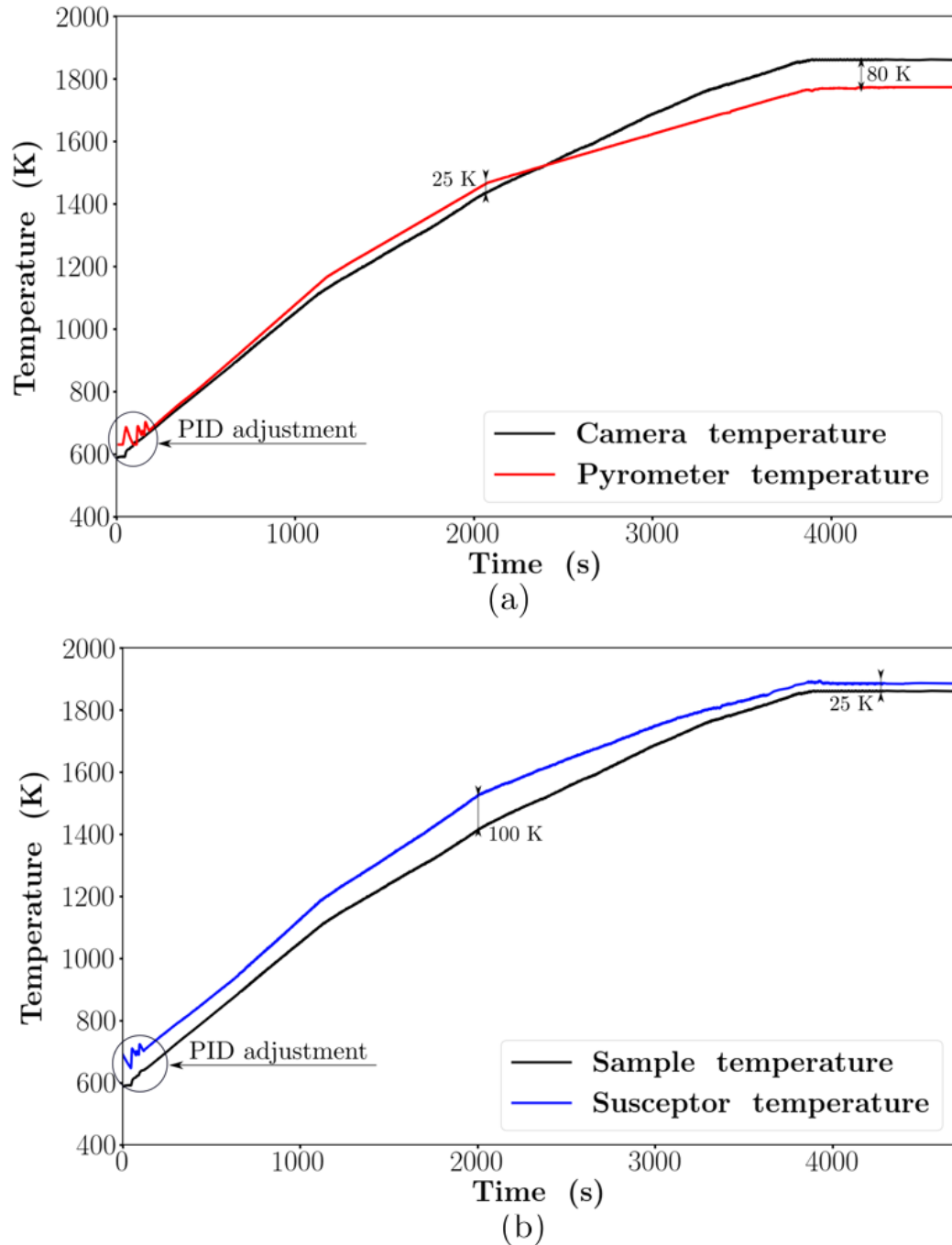


FIGURE 5.8 – Temperature evolution a) at a surface of the sample measured by thermal camera and pyrometer b) at a surface of the susceptor and sample measured by the thermal camera.

5.3 Numerical simulations

5.3.1 Computational domain

The geometry of the microwave cavity used for the numerical simulations of the alumina heating and sintering in hybrid configuration is presented in Figure 5.9. As in the experimental set-up (Figure 5.4), the sintering cell consists in a © RATH insulating box, containing the alumina sample (with parallel orientation), the © RATH support and the SiC susceptors, placed in the 2.45 GHz cavity. This cavity is delimited by an iris on one side and a short-circuit piston on the other side. The changes in the cavity length during the thermal cycle are taken from the experience (PCC curve in Figure 5.7).

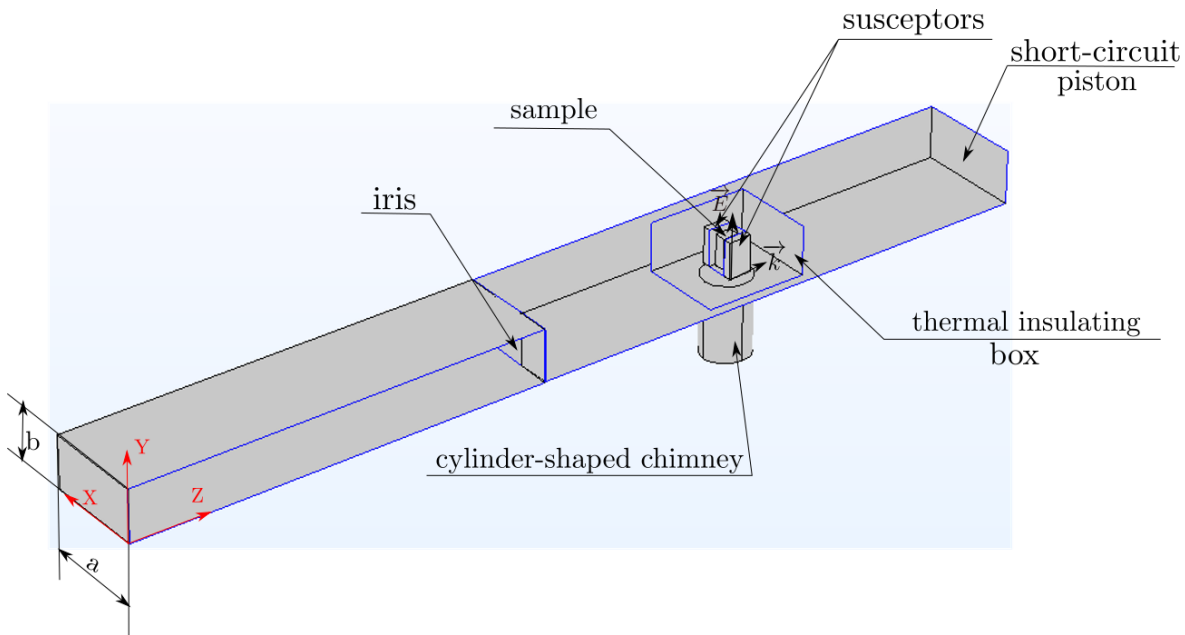


FIGURE 5.9 – 3D geometry of the microwave cavity used for the sintering.

5.3.2 Numerical model and boundary conditions

Figure 5.10 presents a 2D schematic of the microwave cavity used for alumina sintering with the different domains where the electromagnetic-thermal-mechanical coupled problem (Figure 2.7 and Figure 2.8) is solved:

- The electromagnetic problem, reduced in our case to the wave propagation Equation (2.8), is solved by a frequency approach, providing the electric field in the whole computational domain $\Omega = \Omega_{waveguide} \cup \Omega_{sample} \cup \Omega_{susceptor} \cup \Omega_{air} \cup \Omega_{insulating-box}$.
- The thermal problem, expressed by heat Equation (2.11), is solved using a linear finite element approximation in space, combined with an implicit time discretisation. This equation is solved only in the heated system $\Omega_{sample} \cup \Omega_{susceptor} \cup \Omega_{air} \cup \Omega_{insulating-box}$.
- As a first approach, the mechanical problem, described by the momentum balance equation (Equation (2.12)), is not solved in this work. Instead, the shrinkage of the

sample is taken into account by considering the dependence of the alumina parameters on the relative density D (see Section 5.3.3). This density is known throughout the thermal cycle thanks to dilatometry experiments. With this strategy, the shrinkage of the cylindrical sample is assumed to be homogeneous and corresponds simply to a homothety applied to the sample mesh, or at least to the nodes located on the sample surface. However, the implementation of this approach failed with *COMSOL*® [23] and remains a perspective to this work. Consequently, although the relative density changes with temperature, the dimensions of the sample are constant in the following simulations.

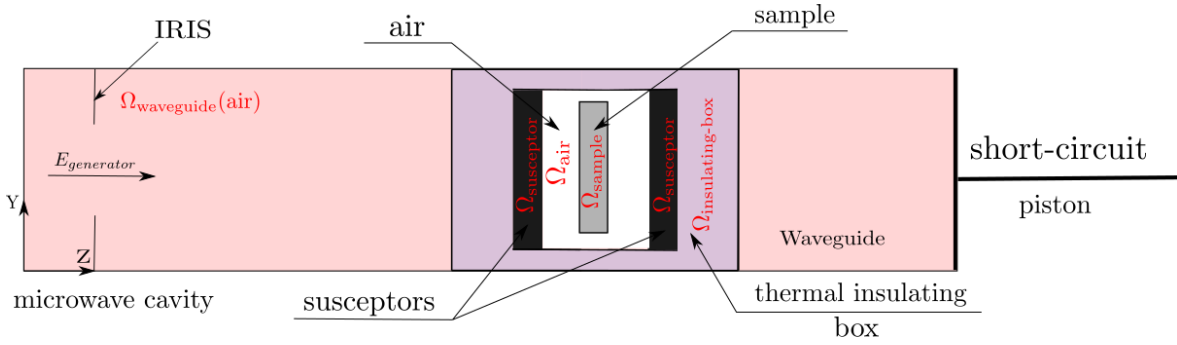


FIGURE 5.10 – Microwave cavity with the different physical domains.

The boundary conditions associated with the wave propagation equation are presented in Figure 5.11 a). As described in Section 1.3.1, microwaves are reflected on a metal surface. Therefore, the cavity walls are considered as perfect electric conductors which means that the wave is totally reflected by the internal surface of the cavity: $\mathbf{n} \times \mathbf{E} = 0$ on this surface, where \mathbf{n} is the unit vector orthogonal to the cavity walls. The second boundary condition for the electromagnetic problem is the rectangular port, in the *COMSOL multiphysics*® [23] denomination. This condition consists in defining the value of the incident power and the mode of propagation: transverse electric TE_{10p} in Figure 5.11 a), with $p = 5$.

The incident power is determined at each instant so as to impose the prescribed thermal cycle already mentioned in Section 5.2.3, Figure 5.6. As in the sintering experiment, a PID controller is therefore included in the simulations to control the sample temperature by adjusting the incident power P_{in} . This control variable is calculated by the standard PID control equation:

$$P_{in}(t) = K_p(T_{set}(t) - T(t)) + K_i \int_0^t (T_{set}(\tau) - T(\tau)) d\tau - K_d \frac{d(T_{set}(t) - T(t))}{dt} \quad (5.1)$$

where T_{set} is the reference value of temperature, and T the measured temperature. The three PID coefficients determined after several tests and used in the simulations are: $K_p = 5$, $K_i = 0.25$ and $K_d = 0.05$.

Concerning the thermal problem, radiative and convective boundary conditions are considered, as presented in Figure 5.11 b). More precisely, a radiative flux Φ_r and convective Φ_c are prescribed on the external surface Γ_{r-c} (in red in the figure) of the insulating

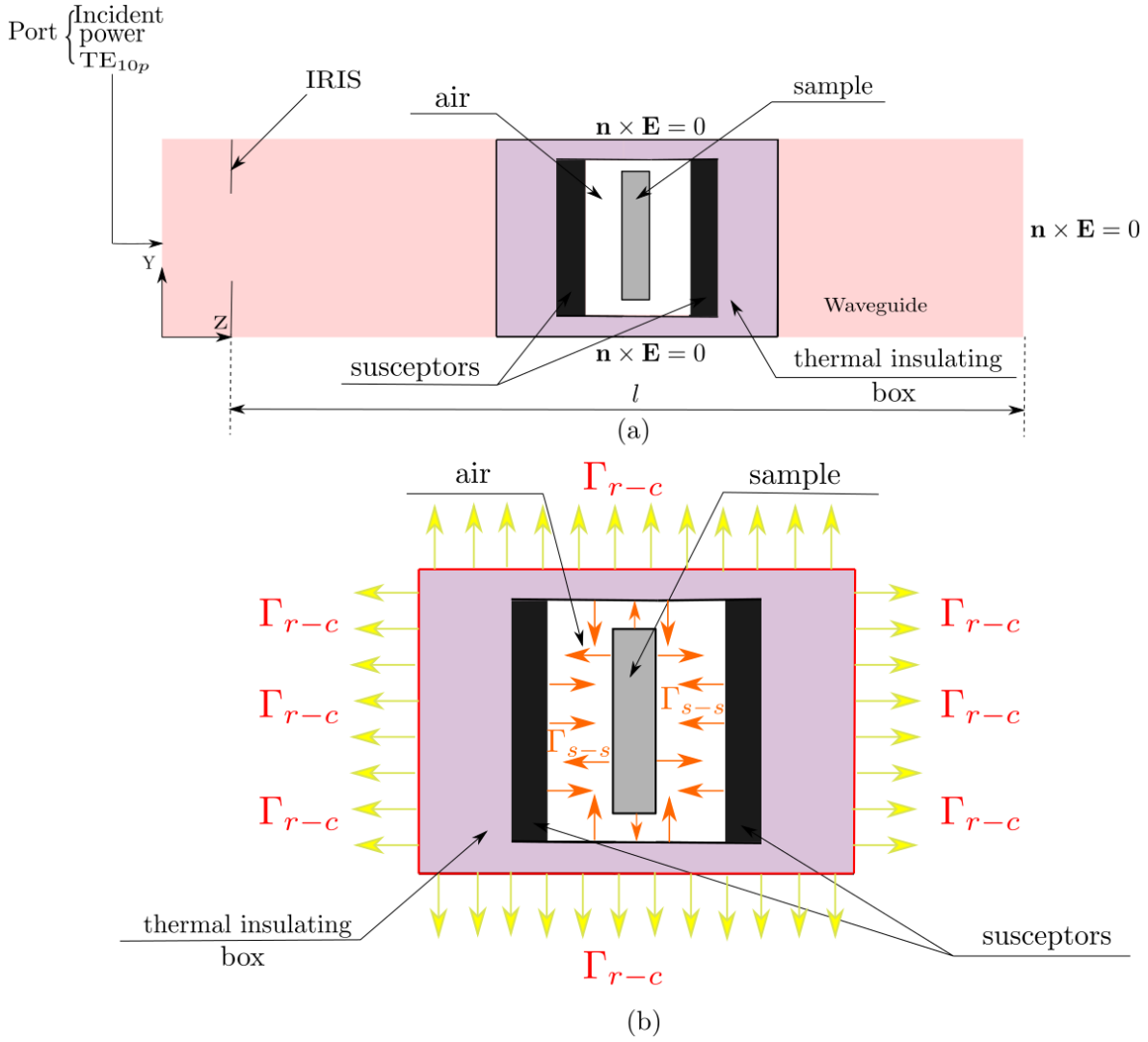


FIGURE 5.11 – Boundary conditions used for the microwave sintering simulation.

box. These fluxes are given by Equations (2.25) and (2.26). On the internal surfaces, denoted by Γ_{s-s} (in orange) in Figure 5.11b), a condition of heat transfer by radiation, called “surface to surface radiation” is applied. The outgoing radiation flux, or surface radiosity, J is defined as the sum of thermal radiation $\epsilon e_b(T)$ and the reflected radiations $(1 - \epsilon)G$ (see Figure 5.12):

$$J = (1 - \epsilon)G + \epsilon e_b(T) = (1 - \epsilon)G + \epsilon n^2 \sigma_B T^4 \quad (5.2)$$

where G is the radiation received from the environment, ϵ the emissivity, n is the reflection index, and σ_B the Stefan-Boltzmann’s constant.

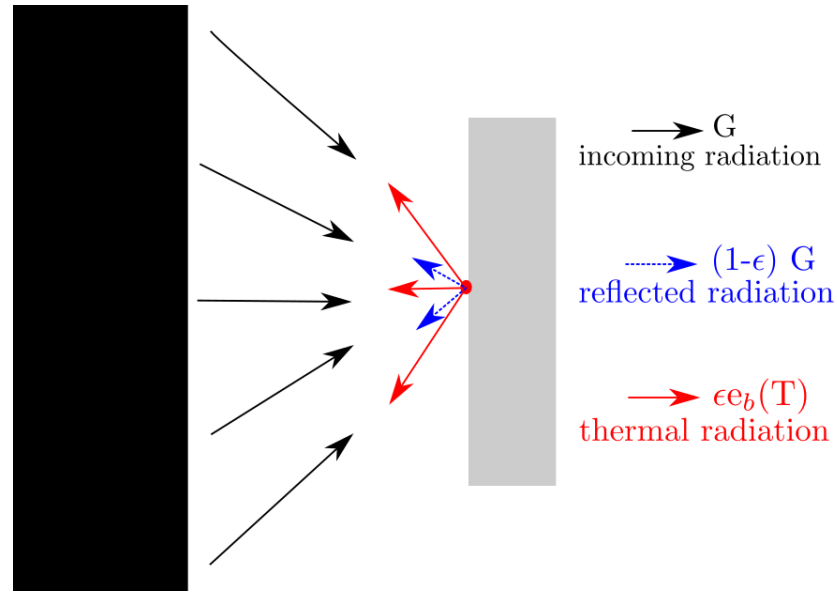


FIGURE 5.12 – Surface to surface radiation condition.

5.3.3 Material parameters

The material parameters of the susceptors, thermal insulation box and air are given as a function of temperature in Table C.1, Appendix C. As said in Section 5.3.2, the alumina parameters depend also on the relative density D . This dependence is expressed through the effective medium approximation introduced in Section 4.4.1. Furthermore, according to Croquesel [26], the alumina dilatometry curves, providing D versus temperature T during a thermal cycle, are quite similar for conventional and hybrid-microwave sintering. Hence, the temperature dependence of the relative density is directly extracted from the dilatometry curve shown in Figure 4.2 and established for conventional heating.

5.4 Numerical results and discussion

The simulations were carried out using a mesh made up of linear tetrahedral elements. The mesh size varies between 0.15 and 15 mm, while the total number of degrees of freedom (DOF), obtained by adding those of the wave transport equation (3 per node) and the heat equation (1 per node), is 2.9×10^4 . The corresponding computation time is 22 hours for 565 time increments, using 12 cores of an Intel Xeon Gold 6128 bi-processor at 3.4 GHz.

Figure 5.13 shows the evolution of the temperature over time, taken at the bottom surface of the susceptor and the sample (red points on the schematic view). The average of these two curves is also plotted, as it represents the control temperature considered in the PID control Equation 5.1, and therefore follows the set-point temperature. The temperature field, shown at three different instants in this same Figure, looks homogeneous in the sample. This result is validated with the one presented in the Figure 5.14, where the temperature is plotted along a line passing through the insulating box, the susceptors and the sample in X direction (Figure 5.9) at three different instants. Figure 5.14 shows that the temperature of the sample and the susceptors is almost homogeneous at any time.

The numerical curves (Figure 5.13), controlled by the PID, can be compared to the experimental curves shown in Figure 5.8. The same characteristics are observed: the temperature of the susceptors is 90 K higher than that of the sample. In contrast to Figure 5.8, this difference remains constant, even during the dwell time. However, it is not significant with respect to the difference between the temperatures measured by the pyrometer and the infrared camera.

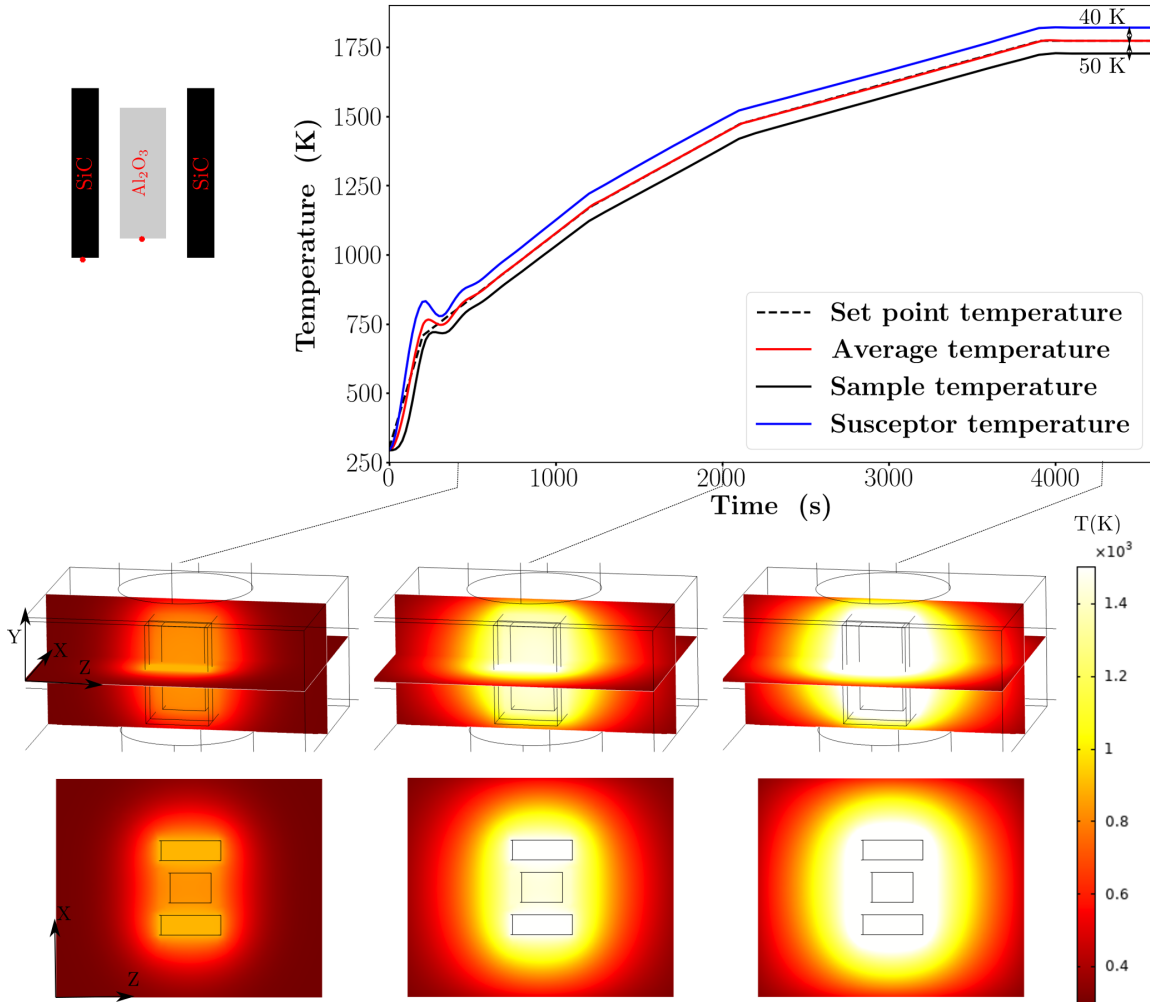


FIGURE 5.13 – Set point, average, sample and susceptor (measured at the red points) temperatures evolution during thermal cycle with temperature iso-values at three different instants.

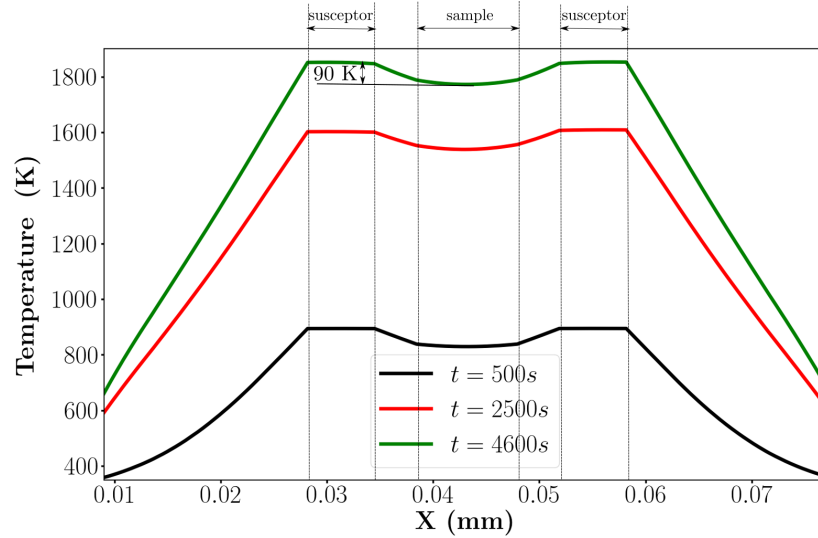


FIGURE 5.14 – The temperature along a line passing through the insulating box, the susceptors and the sample in X direction at three different instants.

More interesting, the incident power delivered during the simulations in the case of fixed and moving piston is presented in Figure 5.15, and can be compared with the incident power delivered during the sintering experiment, plotted in Figure 5.7. The magnitudes obtained experimentally and numerically are of the same order, with a peak up to 1200 W during the initial PID adjustment and a power set around 400 W just after this early stage. The PID in the simulation provides an incident power decreasing from 400 W to 200 W between $t = 1000$ s to $t = 2000$ s, before increasing, reaching a constant value during the dwell time, slightly above 600 W, when the cavity length is adjusted. In the experiment, once stabilised, the delivered power increases continuously, reaching 1270 W during the dwell time. This difference can be explained by the heat loss that occurs in the “real” experiment, due for example to the heating of the cavity walls, as mentioned in Chapter 4. Therefore, the incident power must increase to compensate for this dissipation. Despite this, the simulation and the experiment are close, which shows that the most important physical phenomena have been captured by the model and the simulation.

In addition, Figure 5.15 shows the effect of adjusting the length of the cavity during sintering: when the position of the piston follows that of the experiment (PCC curves in Figure 5.7), the piston starts to move at $t=2200$ s, the cavity remains tuned, and less power is needed to reach the same temperature (400 W instead of 100 W).

To quantify the power absorbed by the different elements of the system, the heat source Q_{EM} , due to the interaction with the electric field, has been integrated over the volume of each domain: susceptors, sample and insulation box. This absorbed power is plotted in Figure 5.16. Clearly, almost all the power absorbed is by the SiC susceptors. This confirms the scenario established in Section 5.2.3: only the SiC susceptors are heated by microwave irradiations. In turn, they heat the sample by thermal radiation. Furthermore, the decrease in the delivered incident power shown in Figure 5.15 between $t = 1000$ s and $t = 2000$ s can now be explained by the increase in the SiC permittivity ϵ'' as the absorbed power keeps increasing during this period.

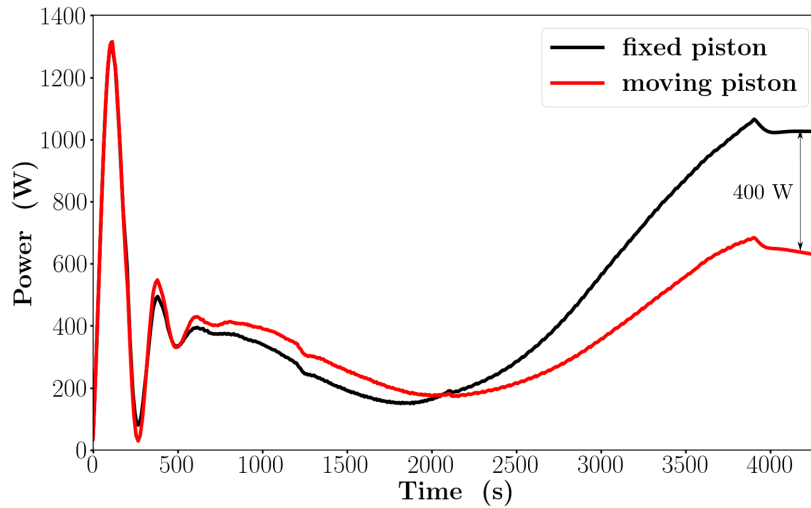


FIGURE 5.15 – Delivered incident power during simulation for fixed and moving piston.

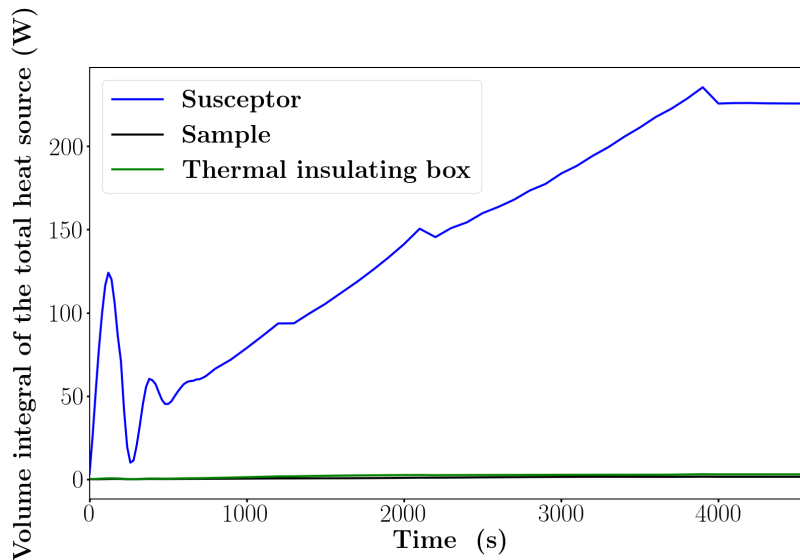


FIGURE 5.16 – Volume integral of the total heat source terms in the susceptors, the sample and the insulating support.

5.5 Conclusion

This chapter is the result of a collaboration between Mines Saint-Étienne and the CRISMAT laboratory in Caen. Experimentally, the hybrid heating and sintering of an alumina sample placed between two susceptors in a single-mode cavity at 2.45 GHz was studied by pyrometry and infrared camera. A PID was used to control the delivered power in order to respect a prescribed temperature cycle, while the reflected power was "minimised" by the automated motion of the piston. A simulation of this hybrid heating/sintering was also carried out, with a higher level of complexity than in previous Chapters: the thermal interaction between the sample, the susceptors, and a thermal insulation box has to be managed, the same thermal cycle as in the experiment has to be prescribed via a PID, while the motion of the piston recorded during the experiment is also imposed. Additionally, the alumina material parameters are taken as function of the temperature, of course,

but also of the relative density, whose variation along the thermal cycle is identified by dilatometry. Although the geometric shrinkage of the sample is not considered in this simulation, the numerical simulation and the experiment give similar results, especially with regard to the incident power, which is adjusted in both cases to follow the prescribed thermal cycle. Furthermore, the simulation confirms a hypothesis made by analysing the experimental results: all the power absorbed is by the SiC susceptors which then heat the alumina sample by radiation. To go further in this description, at least two perspectives can be evoked: to consider in the simulation the mechanical problem (momentum balance) during sintering, and to model the microwave cavity in the thermal problem, in order to take into account the associated thermal dissipation.

Résumé en Français :

Ce chapitre est le résultat d'une collaboration entre Mines Saint-Étienne et le laboratoire CRISMAT de Caen. Expérimentalement, le chauffage hybride et le frittage d'un échantillon d'alumine placé entre deux suscepteurs dans une cavité monomode à 2,45 GHz ont été étudiés par pyrométrie et caméra infrarouge. Un PID a été utilisé pour contrôler la puissance délivrée afin de respecter un cycle de température prescrit, tandis que la puissance réfléchie est "minimisée" par le mouvement automatisé du piston. Une simulation de ce chauffage/frittage hybride a également été réalisée, avec un niveau de complexité plus élevé que dans les chapitres précédents : l'interaction thermique entre l'échantillon, les suscepteurs et un caisson d'isolation thermique doit être gérée, le même cycle thermique que dans l'expérience doit être prescrit via un PID, tandis que le mouvement du piston enregistré pendant l'expérience est également imposé. De plus, les paramètres du matériau alumine sont pris en fonction de la température, la variation de la densité relative de l'alumine est prise en compte à partir de la mesure expérimentale de dilatométrie. Bien que le retrait géométrique de l'échantillon ne soit pas considéré dans cette simulation, la simulation numérique et l'expérience donnent des résultats similaires. En effet, les puissances incidentes expérimentale et numérique correspondent le long du thermique imposé. De plus, la simulation confirme une hypothèse émise par l'analyse des résultats expérimentaux : toute la puissance absorbée l'est par les suscepteurs SiC qui chauffent ensuite l'échantillon d'alumine par rayonnement. Pour aller plus loin dans cette description, au moins deux perspectives peuvent être évoquées : considérer dans la simulation le problème mécanique (bilan de quantité de mouvement) lors du frittage, et modéliser la cavité micro-ondes dans le problème thermique, afin de prendre en compte la dissipation thermique associée.

Conclusion and outlook

The purpose of this work was to carry out, by comparison between experimental and numerical approaches, the analysis of the microwave heating of a SiC sample, with different orientations in the electric field, of an alumina sample, with different relative densities, and of the SiC - alumina system, in order to achieve the sintering of alumina in hybrid configuration. All these studies were conducted in a 2.45 GHz single-mode cavity. In such a cavity, the heating efficiency depends on the length of the cavity: for a so-called resonance length, the incident electric wave is in phase with the reflected wave, resulting in a stationary wave, with positive interference, and therefore higher electric field intensities. The system to be heated is then placed in a maximum of the electric field. Furthermore, as the dielectric parameters of this system are temperature dependent, the cavity should be continuously tuned during the heating process, in order to maintain the resonance property. With the exception of Chapter 5, where the sintering temperature must be reached, the cavity length was adjusted once and for all at room temperature, in order to limit the number of parameters that vary and the associated uncertainty.

The study of the orientation of a parallelepiped sample in the electric field (Chapter 3) was carried out using a SiC sample. Silicon carbide is a material with high dielectric loss even at room temperature. It is often used as a susceptor in microwave heating in hybrid configuration and its temperature-dependent dielectric properties are well documented in the literature. Experimentally, the difficulty lies in the measurement of temperature, since thermocouples cannot be used in a microwave environment. In this work, pyrometers and an infrared camera were used. Both of these devices require a calibration step prior to any measurement, *i.e.* knowledge of the apparent emissivity of the material to be heated. This emissivity was determined under blackbody conditions following the procedure outlined in Chapter 2. The numerical simulations, performed with the *COMSOL multiphysics*® finite element software, consisted in solving an electromagnetic-thermal problem (Chapter 2) under the same conditions as in the experimental approach. Experimental and numerical results were found to be very close for the four analysed orientations, demonstrating the ability of the numerical model to describe microwave heating, as well as the confidence we can have in the SiC dielectric parameters used in these simulations.

The influence of relative density on microwave heating is then investigated in Chapter 4. As for SiC, the apparent emissivity of Al_2O_3 is first determined and it appears that the latter is not very sensitive to the density. Parallelepipedic alumina samples, prepared with three different relative densities, $D=43.8\%$, $D=55\%$ and $D=97\%$, disposed according to the most efficient orientation obtained in Chapter 3, are then heated in the 2.45 GHz monomode cavity. The results show a complex evolution of the sample temperature, with

a two-stage increase of temperature, a maximum temperature reached, before a decrease of in temperature. Further studies have shown that the two-step temperature increase is due to the heating of the insulating support, which leads to conductive heating of the alumina sample. In addition, the final temperature decrease is due to the heating of the cavity walls, which leads to the detuning of the cavity. It is also observed that the lower the density of the sample, the higher the heating efficiency.

To simulate the heating of alumina, the density dependence of its physical parameters was first established using of the classical Effective Medium Approximation. The numerical results were at odds with the experimental facts as the permittivity ϵ'' , and thus the heating efficiency, was predicted to increase with density. By taking experimental permittivity values from the literature and fitting them to the relevant densities, we were able to find a variation in permittivity and therefore temperature in agreement with the experiments. Furthermore, although the two-step temperature increase was not obtained in these simulations, this effect was recovered by modifying the thermal boundary conditions of the insulating substrate. Although this modification is rather arbitrary, it indicates that the substrate can heat the sample (the two materials are "similar") in some situations and that the physical parameters materials still be not well-known. The final temperature decrease cannot be captured by the simulation, since the cavity walls are not represented by physical entities.

The heating of the system silicon carbide - alumina was finally analysed in Chapter 5. The experimental part of this work was carried out at the CRISMAT laboratory in Caen. The alumina parallelepiped is heated up to sintering, between two SiC plates, and this system is itself contained in an insulating box placed in a 2.45 GHz monomode cavity. A thermal cycle is imposed through a PID controller that adjusts the incident power. In addition the cavity length is automatically tuned in order to minimise the reflected power. This device is reproduced numerically. The variation of the relative density of alumina during the thermal cycle is given by dilatometry experiments. However, the geometric shrinkage of the sample was not taken into account. Despite this, the experimental and numerical results remain comparable. In both cases, all the power is absorbed by the SiC susceptors, which heat the alumina by radiation, thus following the set temperature. The simulation shows a quite homogeneous temperature in both the susceptors and the sample, with less than 100 K difference between the two.

At the end of this work, different perspectives can be envisaged. The most immediate prospect concerns the numerical simulation, which should take into account the shrinkage of the material being sintered. To do this, it is necessary to establish a solid mechanics problem, based on the momentum balance equation, and to update the geometry of the material according to the displacement field, solution of this equation. However, the question arises of the constitutive law of the material during sintering : the elastoviscoplastic law in all generality, the derivation of the different parameters of this law from experimental and numerical characterisation, the temperature and density dependence of the parameter. In other words, the work done for the thermal-electromagnetic problem, should be extended to the mechanical problem, with simple tests decorrelating the

different phenomena.

The second perspective concerns the dielectric parameters of the materials to be heated, in particular the permittivity, which has appeared throughout this work as the key parameter determining microwave heating. The permittivity values remain difficult to find in the literature, even for pure materials. For heating efficiency, the industrial materials can be doped by some chemical species to modify their permittivity. Consequently, the control of microwave heating seems to require the ability to perform reliable permittivity measurements of materials for different temperatures and relative densities. This is still challenging. Furthermore, some advantages can be found in considering multi-materials (ceramic/ceramic, or ceramic/metal), or even architecturally engineered materials, for example manufactured by an additive process. Numerical simulation, not at the macroscopic scale as in this work but at a mesoscopic scale, could be used in conjunction with experimental characterisations, to evaluate and optimise the dielectric behaviour of these complex materials. Such simulations remain based on the tools explored in this work.

Conclusion et perspectives

Le but de ce travail a été de réaliser, par comparaison entre des approches expérimentales et numériques, l'analyse du chauffage par micro-ondes d'un échantillon en SiC, pour différentes orientations dans le champ électrique, d'un échantillon d'alumine, avec différentes densités relatives, et un système SiC - alumine, afin de réaliser le frittage de l'alumine en configuration hybride. Toutes ces études ont été menées dans une cavité monomode de 2,45 GHz. Dans une telle cavité, l'efficacité du chauffage dépend de la longueur de la cavité : pour une longueur dite de résonance, l'onde électrique incidente est en phase avec l'onde réfléchie, ce qui donne une onde stationnaire, avec interférence positive, et donc des intensités de champ électrique plus élevées. Le système à chauffer est alors placé dans un maximum du champ électrique. En outre, comme les paramètres diélectriques de ce système dépendent de la température, la cavité doit être réglée en permanence pendant le processus de chauffage, afin de maintenir la propriété de résonance. A l'exception du Chapitre 5, où la température de frittage doit être atteinte, la longueur de la cavité a été ajustée une fois pour toutes à température ambiante, afin de limiter le nombre de paramètres qui varient et l'incertitude associée.

L'étude de l'orientation d'un échantillon parallélépipédique placé dans le champ électrique (Chapitre 3) a été réalisée avec un échantillon en SiC. Le carbure de silicium est un matériau à forte perte diélectrique même à température ambiante. Il est souvent utilisé comme suscepteur dans le chauffage par micro-ondes en configuration hybride. Ses propriétés diélectriques en fonction de la température sont bien documentées dans la littérature. La difficulté des études expérimentales du chauffage par micro-ondes réside dans la mesure de la température car les thermocouples ne peuvent être utilisés dans un environnement micro-ondes. Dans ce travail, des pyromètres et une caméra infrarouge ont été utilisés. Ces deux appareils nécessitent une étape d'étalonnage avant toute mesure, c'est-à-dire la connaissance de l'émissivité apparente du matériau à chauffer. Cette émissivité a été déterminée dans les conditions d'un corps noir en suivant la procédure décrite dans le Chapitre 2. Les simulations numériques, réalisées avec le logiciel d'éléments finis *COMSOL multiphysics*®, ont consisté à résoudre un problème couplé électromagnétique-thermique (Chapitre 2) dans les mêmes conditions que dans l'approche expérimentale. Les résultats expérimentaux et numériques se sont avérés très proches pour les quatre orientations analysées, démontrant la capacité du modèle numérique à décrire le chauffage par micro-ondes. Ils ont également permis de valider les paramètres diélectriques du SiC utilisés dans ces simulations.

L'influence de la densité relative sur le chauffage par micro-ondes est ensuite étudiée dans le Chapitre 4. Comme pour le SiC, l'émissivité apparente de Al_2O_3 est d'abord déterminée et il apparaît que cette dernière est peu sensible à la densité. Des échantillons

parallélépipédiques d'alumine, préparés à trois densités relatives différentes, $D=43,8\%$, $D=55\%$ et $D=97\%$, disposés selon l'orientation la plus efficace obtenue au Chapitre 3, sont ensuite chauffés dans la cavité monomode de 2,45 GHz. Les résultats montrent une évolution complexe de la température de l'échantillon, avec une augmentation de la température en deux étapes, une température maximale atteinte, avant une diminution de la température. Des études complémentaires ont montré que l'augmentation de température en deux étapes est due au chauffage du support isolant, qui entraîne un chauffage par conduction de l'échantillon d'alumine. La diminution finale de la température est due à l'échauffement des parois de la cavité, ce qui entraîne le désaccord de la cavité. On observe également que plus la densité de l'échantillon est faible, plus l'efficacité du chauffage est élevée.

Pour simuler le chauffage de l'alumine, la dépendance de ses paramètres physiques avec la densité a d'abord été établie en utilisant l'approximation des milieux effectifs (EMA). Des résultats numériques en contradiction avec les faits expérimentaux ont été obtenus en raison de l'approximation qui donne des valeurs de permittivités (efficacité du chauffage) qui augmentent avec la densité. En prenant les valeurs de permittivité expérimentales issue de la littérature et en les ajustant aux densités utilisées, nous avons pu trouver une variation de la permittivité et donc de la température en accord avec les expériences. Bien que l'augmentation de température en deux étapes n'ait pas été obtenue dans ces simulations, cet effet a pu être décrit en modifiant les conditions limites thermiques du substrat isolant. Bien que cette modification soit plutôt arbitraire, elle indique que le substrat peut chauffer l'échantillon (les deux matériaux ont des propriétés diélectriques voisines) dans certaines situations. Ce résultat montre également que les paramètres physiques des matériaux ne sont pas bien connus. La décroissance finale de la température ne peut pas être décrite par la simulation, en raison de l'approximation faite où les parois de la cavité ne sont pas représentées par des entités physiques.

Le chauffage du système carbure de silicium - alumine a enfin été analysé dans le Chapitre 5. La partie expérimentale de ce travail a été réalisée au laboratoire du CRISMAT à Caen. Le parallélépipède d'alumine est chauffé jusqu'au frittage, entre deux plaques de SiC. Ce système est lui-même contenu dans une boîte isolante placée dans une cavité monomode de 2,45 GHz. Un cycle thermique est imposé par un contrôleur PID qui ajuste la puissance incidente. De plus, la longueur de la cavité est automatiquement ajustée afin de minimiser la puissance réfléchie. Ce dispositif est reproduit numériquement. La variation de la densité relative de l'alumine au cours du cycle thermique est donnée par des expériences de dilatométrie. Bien que, le retrait géométrique de l'échantillon n'a pas été pris en compte, les résultats expérimentaux et numériques sont comparables. Dans les deux cas, toute la puissance est absorbée par les suscepteurs SiC, qui chauffent l'alumine par rayonnement, suivant ainsi la température imposée. La simulation montre une température assez homogène à la fois dans les suscepteurs et dans l'échantillon, avec moins de 100 K d'écart entre les deux.

A l'issue de ce travail, différentes perspectives peuvent être envisagées. La perspective la plus immédiate concerne la simulation numérique, qui devrait prendre en compte

le retrait du matériau fritté. Pour ce faire, il est nécessaire d'établir un problème de mécanique du solide, basé sur l'équation du bilan de quantité de mouvement, et d'actualiser la géométrie du matériau en fonction du champ de déplacement, solution de cette équation. Cependant, la question de la loi constitutive du matériau pendant le frittage se pose : loi élasto-viscoplastique, dérivation des différents paramètres de cette loi à partir de caractérisations expérimentales et numériques, dépendance à la température et à la densité du paramètre. En d'autres termes, le travail effectué pour traiter le problème thermo-électromagnétique, devrait être étendu au problème mécanique, avec des tests simples décorrélant les différents phénomènes.

La deuxième perspective concerne les paramètres diélectriques des matériaux à chauffer, en particulier la permittivité, qui est apparue tout au long de ce travail comme le paramètre clé qui détermine le chauffage par micro-ondes. Les valeurs de permittivité sont difficiles à trouver dans la littérature, pour les matériaux purs. Elles le sont d'autant plus pour les matériaux industriels qui peuvent être dopés par certaines espèces chimiques pour modifier leur permittivité. Par conséquent, le contrôle du chauffage par micro-ondes semble exiger la capacité d'effectuer des mesures fiables de la permittivité des matériaux pour différentes températures et densités relatives. Cela reste un défi. En outre, certains avantages du chauffage micro-onde pourraient être trouvés en considérant des matériaux multiples (céramique/céramique, ou céramique/métal), ou même des matériaux architecturaux, par exemple fabriqués par un procédé additif. La simulation numérique, non pas à l'échelle macroscopique comme dans ce travail mais à une échelle mésoscopique, pourrait être utilisée en parallèle conjonction avec des caractérisations expérimentales, pour évaluer et optimiser le comportement diélectrique de ces matériaux complexes. De telles simulations restent basées sur les outils qui ont été explorés dans ce travail.

APPENDICES

Annexe A

Time-average of poynting vector

The instantaneous Poynting vector of an electromagnetic wave is given by [83] :

$$\Pi(t) = \mathbf{E} \times \mathbf{H} = \text{Re}(\tilde{\mathbf{E}}) \times \text{Re}(\tilde{\mathbf{H}}) \quad (\text{A.1})$$

where \mathbf{E} is the physical electric field, \mathbf{H} is the physical magnetic field, $\tilde{\mathbf{E}}$ is the complex representation of the electric field and $\tilde{\mathbf{H}}$ is the complex representation of the magnetic field.

The complex representation of the electric and magnetic fields can be written as :

$$\tilde{\mathbf{E}} = \tilde{\mathbf{E}}_m e^{j\omega t} = \tilde{\mathbf{E}}_m (\cos(\omega t) + j \sin(\omega t)) \quad (\text{A.2})$$

$$\tilde{\mathbf{H}} = \tilde{\mathbf{H}}_m e^{j\omega t} = \tilde{\mathbf{H}}_m (\cos(\omega t) + j \sin(\omega t)) \quad (\text{A.3})$$

where $\tilde{\mathbf{E}}_m$ and $\tilde{\mathbf{H}}_m$ contain the space dependence and the phase, ω is the angular frequency and j is the complex number such as $j^2 = -1$.

Using Equation (A.2) and Equation (A.3), the poynting vector will be written as :

$$\Pi = \text{Re} [\tilde{\mathbf{E}}_m (\cos(\omega t) + j \sin(\omega t))] \times \text{Re} [\tilde{\mathbf{H}}_m (\cos(\omega t) + j \sin(\omega t))] \quad (\text{A.4})$$

The complex vectors $\tilde{\mathbf{E}}_m$ and $\tilde{\mathbf{H}}_m$ can be written as :

$$\tilde{\mathbf{E}}_m = \text{Re}(\tilde{\mathbf{E}}_m) + j \text{Im}(\tilde{\mathbf{E}}_m) \quad (\text{A.5})$$

$$\tilde{\mathbf{H}}_m = \text{Re}(\tilde{\mathbf{H}}_m) + j \text{Im}(\tilde{\mathbf{H}}_m) \quad (\text{A.6})$$

Using Equation (A.5) and Equation (A.6), the poynting vector, Equation (A.4), will be written as :

$$\Pi = \text{Re} \left[\left(\text{Re}(\tilde{\mathbf{E}}_m) + j \text{Im}(\tilde{\mathbf{E}}_m) \right) (\cos(\omega t) + j \sin(\omega t)) \right] \times \text{Re} \left[\left(\text{Re}(\tilde{\mathbf{H}}_m) + j \text{Im}(\tilde{\mathbf{H}}_m) \right) (\cos(\omega t) + j \sin(\omega t)) \right] \quad (\text{A.7})$$

Extracting the real parts from Equation (A.7), we have :

$$\Pi = \left(\text{Re}(\tilde{\mathbf{E}}_m) \cos(\omega t) - \text{Im}(\tilde{\mathbf{E}}_m) \sin(\omega t) \right) \times \left(\text{Re}(\tilde{\mathbf{H}}_m) \cos(\omega t) - \text{Im}(\tilde{\mathbf{H}}_m) \sin(\omega t) \right) \quad (\text{A.8})$$

$$\begin{aligned} &= \text{Re}(\tilde{\mathbf{E}}_m) \times \text{Re}(\tilde{\mathbf{H}}_m) \cos^2(\omega t) - \text{Re}(\tilde{\mathbf{E}}_m) \times \text{Im}(\tilde{\mathbf{H}}_m) \cos(\omega t) \sin(\omega t) \\ &\quad + \text{Im}(\tilde{\mathbf{E}}_m) \times \text{Im}(\tilde{\mathbf{H}}_m) \sin^2(\omega t) - \text{Im}(\tilde{\mathbf{E}}_m) \times \text{Re}(\tilde{\mathbf{H}}_m) \cos(\omega t) \sin(\omega t) \end{aligned} \quad (\text{A.9})$$

Applying the double-angle identities for $\cos^2(\omega t)$, $\sin^2(\omega t)$ and $\cos(\omega t) \sin(\omega t)$, Equation (D.3) becomes :

$$\begin{aligned} \Pi = & \operatorname{Re}(\tilde{\mathbf{E}}_m) \times \operatorname{Re}(\tilde{\mathbf{H}}_m) \left(\frac{1 + \cos 2\omega t}{2} \right) - \operatorname{Re}(\tilde{\mathbf{E}}_m) \times \operatorname{Im}(\tilde{\mathbf{H}}_m) \left(\frac{\sin 2\omega t}{2} \right) \\ & + \operatorname{Im}(\tilde{\mathbf{E}}_m) \times \operatorname{Im}(\tilde{\mathbf{H}}_m) \left(\frac{1 - \cos 2\omega t}{2} \right) - \operatorname{Im}(\tilde{\mathbf{E}}_m) \times \operatorname{Re}(\tilde{\mathbf{H}}_m) \left(\frac{\sin 2\omega t}{2} \right) \end{aligned} \quad (\text{A.10})$$

Upon time-averaging over a single period $T = 2\pi/\omega$ at the fundamental frequency, the $\cos 2\omega t$ and $\sin 2\omega t$ terms of average to zero, yielding :

$$\langle \Pi \rangle = \frac{1}{2} [(\operatorname{Re}(\tilde{\mathbf{E}}_m) \times \operatorname{Re}(\tilde{\mathbf{H}}_m)) + (\operatorname{Im}(\tilde{\mathbf{E}}_m) \times \operatorname{Im}(\tilde{\mathbf{H}}_m))] \quad (\text{A.11})$$

We now add and subtract the same pure imaginary term :

$$\begin{aligned} \langle \Pi \rangle = & \frac{1}{2} \operatorname{Re} \left[(\operatorname{Re}(\tilde{\mathbf{E}}_m) \times \operatorname{Re}(\tilde{\mathbf{H}}_m)) + (\operatorname{Im}(\tilde{\mathbf{E}}_m) \times \operatorname{Im}(\tilde{\mathbf{H}}_m)) \right. \\ & \left. - \underbrace{j(\operatorname{Re}(\tilde{\mathbf{E}}_m) \times \operatorname{Im}(\tilde{\mathbf{H}}_m)) + j(\operatorname{Im}(\tilde{\mathbf{E}}_m) \times \operatorname{Re}(\tilde{\mathbf{H}}_m))}_{\text{added pure imaginary terms}} \right] \end{aligned} \quad (\text{A.12})$$

$$= \frac{1}{2} \operatorname{Re} [(\operatorname{Re} \tilde{\mathbf{E}}_m + j \operatorname{Im} \tilde{\mathbf{E}}_m) \times (\operatorname{Re} \tilde{\mathbf{H}}_m - j \operatorname{Im} \tilde{\mathbf{H}}_m)] \quad (\text{A.13})$$

Finally, the Poynting vector averaged over a time period is written as :

$$\langle \Pi \rangle = \frac{1}{2} \operatorname{Re} (\tilde{\mathbf{E}} \times \overline{\tilde{\mathbf{H}}}) \quad (\text{A.14})$$

where $\overline{\tilde{\mathbf{H}}}$ is the complex conjugate of the magnetic field.

Note that, as the electric and magnetic fields change with the temperature of the material, the them $\langle \Pi \rangle$ changes also with the temperature.

Annexe B

Heat source term

The heat source term Q_{EM} due to the dissipation of the electromagnetic energy, can be calculated from the integration of the Poynting vector across a closed surface S . According to Appendix A, the heat source Q_{EM} , is written as :

$$Q_{EM} = -\frac{1}{2} \oint_S \text{Re}(\tilde{\mathbf{E}} \times \bar{\tilde{\mathbf{H}}}) \cdot d\mathbf{S} \quad (\text{B.1})$$

where $\tilde{\mathbf{E}}$ is the complex representation of the electric field and $\bar{\tilde{\mathbf{H}}}$ is the conjugate of the complex representation of the magnetic field.

Using the divergence (Green-Ostrogradsky) theorem, leads to :

$$\oint_S (\tilde{\mathbf{E}} \times \bar{\tilde{\mathbf{H}}}) \cdot d\mathbf{S} = \int_V \nabla \cdot (\tilde{\mathbf{E}} \times \bar{\tilde{\mathbf{H}}}) dV \quad (\text{B.2})$$

where :

$$\nabla \cdot (\tilde{\mathbf{E}} \times \bar{\tilde{\mathbf{H}}}) = \bar{\tilde{\mathbf{H}}} \cdot \nabla \times \tilde{\mathbf{E}} - \tilde{\mathbf{E}} \cdot \nabla \times \bar{\tilde{\mathbf{H}}} \quad (\text{B.3})$$

The complex representation of the electric field $\tilde{\mathbf{E}}$ and the complex representation of the magnetic field $\tilde{\mathbf{H}}$ are written as :

$$\tilde{\mathbf{E}} = \tilde{\mathbf{E}}_m e^{(j\omega t)} \quad (\text{B.4})$$

$$\tilde{\mathbf{H}} = \tilde{\mathbf{H}}_m e^{(j\omega t)} \quad (\text{B.5})$$

The complex-conjugates are :

$$\bar{\tilde{\mathbf{E}}} = \bar{\tilde{\mathbf{E}}}_m e^{(j\omega t)} \quad (\text{B.6})$$

$$\bar{\tilde{\mathbf{H}}} = \bar{\tilde{\mathbf{H}}}_m e^{(-j\omega t)} \quad (\text{B.7})$$

Using Faraday's and Ampere's laws (Equations (1.3) and (1.4) respectively) and interaction of the electromagnetic field with the matter equations (Equation (1.5), Equation (D.8) and Equation (1.7)) in Equation (B.3), this last will be written as :

$$\begin{aligned} \nabla \cdot (\tilde{\mathbf{E}} \times \bar{\tilde{\mathbf{H}}}) &= \bar{\tilde{\mathbf{H}}} \cdot \left(-\mu^* \frac{\partial \tilde{\mathbf{H}}}{\partial t} \right) - \tilde{\mathbf{E}} \cdot \left(\sigma_e \bar{\tilde{\mathbf{E}}} + \bar{\varepsilon}^* \frac{\partial \bar{\tilde{\mathbf{E}}}}{\partial t} \right) \\ &= -j\omega \mu^* \bar{\tilde{\mathbf{H}}}_m \cdot \tilde{\mathbf{H}}_m - \sigma_e \bar{\tilde{\mathbf{E}}}_m \cdot \tilde{\mathbf{E}}_m + j\omega \bar{\varepsilon}^* \bar{\tilde{\mathbf{E}}}_m \cdot \tilde{\mathbf{E}}_m \\ &= -j\omega \left(\mu^* \bar{\tilde{\mathbf{H}}}_m \cdot \tilde{\mathbf{H}}_m - \bar{\varepsilon}^* \bar{\tilde{\mathbf{E}}}_m \cdot \tilde{\mathbf{E}}_m \right) - \sigma_e \bar{\tilde{\mathbf{E}}}_m \cdot \tilde{\mathbf{E}}_m \end{aligned} \quad (\text{B.8})$$

The complex permittivity ε^* and the complex permeability μ^* are written as :

$$\varepsilon^* = \varepsilon' - j\varepsilon'' = \varepsilon_0(\varepsilon'_r - j\varepsilon''_r) \quad (\text{B.9})$$

$$\mu^* = \mu' - j\mu'' = \mu_0(\mu'_r - j\mu''_r) \quad (\text{B.10})$$

The conjugate of the complex permittivity $\overline{\varepsilon^*}$ is :

$$\overline{\varepsilon^*} = \varepsilon' + j\varepsilon'' = \varepsilon_0(\varepsilon'_r + j\varepsilon''_r) \quad (\text{B.11})$$

Replacing the complex permeability and the conjugate of the complex permittivity by their expressions, Equation (B.8) will be written as :

$$\begin{aligned} \nabla \cdot (\tilde{\mathbf{E}} \times \overline{\tilde{\mathbf{H}}}) &= -j\omega \left((\mu' - j\mu'')\tilde{\mathbf{H}}_m^2 - (\varepsilon' + j\varepsilon'')\tilde{\mathbf{E}}_m^2 \right) - \sigma_e \tilde{\mathbf{E}}_m^2 \\ &= -\omega \left(\mu''\tilde{\mathbf{H}}_m^2 + \varepsilon''\tilde{\mathbf{E}}_m^2 \right) - \sigma_e \tilde{\mathbf{E}}_m^2 - j\omega \left(\mu'\tilde{\mathbf{H}}_m^2 + \varepsilon'\tilde{\mathbf{E}}_m^2 \right) \\ &= -\omega \left(\mu_0\mu''_r\tilde{\mathbf{H}}_m^2 + \varepsilon_0\varepsilon''_r\tilde{\mathbf{E}}_m^2 \right) - \sigma_e \tilde{\mathbf{E}}_m^2 - j\omega \left(\mu_0\mu'_r\tilde{\mathbf{H}}_m^2 + \varepsilon_0\varepsilon'_r\tilde{\mathbf{E}}_m^2 \right) \end{aligned} \quad (\text{B.12})$$

Using Equation (B.1), the heat source term is finally written as :

$$Q_{EM} = \frac{1}{2}\sigma_e \tilde{\mathbf{E}}_m^2 + \frac{\omega}{2}\varepsilon_0\varepsilon''_r\tilde{\mathbf{E}}_m^2 + \frac{\omega}{2}\mu_0\mu''_r\tilde{\mathbf{H}}_m^2 \quad (\text{B.13})$$

Annexe C

Electromagnetic-thermal material properties

TABLE C.1 – Electromagnetic-thermal material properties.

Material	Symbol (unit)	Temperature range (K)	Expression
Insulation[57]	C_p (J.kg ⁻¹ .K ⁻¹)	273-1873 K	$5.82 \times 10^2 + 1.25T - 5.31 \times 10^{-4}T^2$
	κ (W.m ⁻¹ .K ⁻¹)	273-1873 K	$6.15 \times 10^{-2} + 1.74 \times 10^{-4}T$
	$\bar{\rho}$ (kg.m ⁻³)	273-1873 K	$4.43 \times 10^2 - 1.04 \times 10^{-2}T$
	ϵ	273-1873 K	0.83
	Hyp 1 [57] : ϵ_r	273-1873 K	1. (microwave transparent)
	Hyp 2 [56] : ϵ'_r	273-1873 K	$1.5 + 1.37 \times 10^{-5}T + 5.03 \times 10^{-8}T^2$
	Hyp 2 [56] : ϵ''_r	273-1873 K	$3.96 \times 10^{-4} - 1.64 \times 10^{-6}T + 2.5 \times 10^{-9}T^2$
SiC[11, 62]	C_p (J.kg ⁻¹ .K ⁻¹)	273-673 K 673-1873 K	$-8.35 + 3.08T - 0.00293T^2 + 1.0268 \times 10^{-6}T^3$ $772 + 0.431T - 2.1 \times 10^{-5}T^2$
	κ (W.m ⁻¹ .K ⁻¹)	273-1873 K	$192 - 0.326T + 2.74 \times 10^{-4}T^2 - 7.71 \times 10^{-8}T^3$
	$\bar{\rho}$ (kg.m ⁻³)	273-1873 K	$2977 + 0.051T - 2.29 \times 10^{-4}T^2 + 2.98 \times 10^{-7}T^3$ $-1.92 \times 10^{-10}T^4 + 4.77 \times 10^{-14}T^5$
	ϵ [37]	273-1873 K	$-1.239 \times 10^{-12}T^4 + 4.51 \times 10^{-9}T^3 - 6.114 \times 10^{-6}T^2$ $+ 0.0037T + 0.1436$
	ϵ'_r	273-1873 K	$6.4 - 1.67 \times 10^{-3}T + 1.88 \times 10^{-6}T^2$
	ϵ''_r	273-1873 K	$0.992 - 3.43 \times 10^{-4}T + 7.72 \times 10^{-6}T^2 - 7.15 \times 10^{-9}T^3$ $+ 2.36 \times 10^{-12}T^4$
	Air[59]	C_p (J.kg ⁻¹ .K ⁻¹)	273-1873 K
κ (W.m ⁻¹ .K ⁻¹)		273-1873 K	$0.0035 + 6 \times 10^{-5}T$
$\bar{\rho}$ (kg.m ⁻³)		273-1873 K	$0.02897P/(RT)$
ϵ_r		273-1873 K	1
Al ₂ O ₃	C_p (J.kg ⁻¹ .K ⁻¹) [7]	298-1873 K	$-40.92 + 4.024T - 0.0005T^2 + 2.8852 \times 10^{-6}T^3$ $- 6.2488 \times 10^{-10}T^4$
	κ (W.m ⁻¹ .K ⁻¹) [7]	298-1873 K	$85.686 - 0.23T + 2.607 \times 10^{-4}T^2 - 1.36 \times 10^{-7}T^3$ $+ 2.7092 \times 10^{-11}T^4$
	$\bar{\rho}$ (kg.m ⁻³)	273-1873 K	3987
	ϵ	273-1873 K	0.95
	ϵ'_r [59]	273-1873 K	$8.3 + 1.34 \times 10^{-3}T$
	ϵ''_r [59]	273-1873 K	$-8.87 \times 10^{-3} + 4.62 \times 10^{-5}T$

Annexe D

Wave propagation equation

To write the wave propagation equation, we use Maxwell equations and the wave/matter interaction equations. Let's first of all write Faraday's law and the expression of the magnetic field interaction with the matter :

$$\nabla \times \mathbf{E} = -\frac{\partial \mathbf{B}}{\partial t} \quad (\text{D.1})$$

$$\mathbf{B} = \mu^* \mathbf{H} \quad (\text{D.2})$$

Combining both equations, we obtain :

$$\nabla \times \mathbf{E} = -\mu^* \frac{\partial \mathbf{H}}{\partial t} \quad (\text{D.3})$$

Dividing Equation (D.3) by μ^* , we obtain :

$$(\mu^*)^{-1} \nabla \times \mathbf{E} + \frac{\partial \mathbf{H}}{\partial t} = 0 \quad (\text{D.4})$$

Then taking the rotational of this equation :

$$\nabla \times ((\mu^*)^{-1} \nabla \times \mathbf{E}) + \nabla \times \left(\frac{\partial \mathbf{H}}{\partial t} \right) = 0 \quad (\text{D.5})$$

Using Ampere' law (Equation (D.6)), the displacement (Equation (D.7)) and the conductivity (Equation (D.8)) :

$$\nabla \times \mathbf{H} = \mathbf{J} + \frac{\partial \mathbf{D}}{\partial t} \quad (\text{D.6})$$

$$\mathbf{D} = \varepsilon^* \mathbf{E} \quad (\text{D.7})$$

$$\mathbf{J} = \sigma_e \mathbf{E} \quad (\text{D.8})$$

Equation (D.5) becomes :

$$\nabla \times ((\mu^*)^{-1} \nabla \times \mathbf{E}) + \sigma_e \frac{\partial \mathbf{E}}{\partial t} + \varepsilon^* \frac{\partial^2 \mathbf{E}}{\partial t^2} = 0 \quad (\text{D.9})$$

The general form of the solution to Equation (D.9) can be written in harmonic form :

$$\mathbf{E} = \text{Re}(\tilde{\mathbf{E}}) = \text{Re}(\tilde{\mathbf{E}}_m e^{(j\omega t)}) \quad (\text{D.10})$$

where \mathbf{E} is the physical electric field, $\tilde{\mathbf{E}}$ is the complex representation of the electric field, $\tilde{\mathbf{E}}_m$ is the complex vector containing the space dependence and the phase, t is the time variable, j the complex number such as $j^2 = -1$ and ω is the angular frequency.

Using the time harmonic form of the electric field (Equation (D.10)), Equation (D.9), reduces to [89, 84] :

$$\nabla \times ((\mu^*)^{-1} \nabla \times \tilde{\mathbf{E}}_m) + j\omega\sigma_e \tilde{\mathbf{E}}_m - \varepsilon^* \omega^2 \tilde{\mathbf{E}}_m = 0 \quad (\text{D.11})$$

which can be written also as :

$$\nabla \times ((\mu^*)^{-1} \nabla \times \tilde{\mathbf{E}}_m) = \omega^2 \left(\varepsilon^* - \frac{j\sigma_e}{\omega} \right) \tilde{\mathbf{E}}_m \quad (\text{D.12})$$

Introducing the relative permittivity $\varepsilon^* = \varepsilon_0 \varepsilon_r^*$ and the relative permeability $\mu^* = \mu_0 \mu_r^*$, we finally obtain the wave propagation equation of the electric field :

$$\nabla \times ((\mu_r^*)^{-1}) \nabla \times \tilde{\mathbf{E}}_m = k_0^2 \left(\varepsilon_r^* - \frac{j\sigma_e}{\omega \varepsilon_0} \right) \tilde{\mathbf{E}}_m \quad (\text{D.13})$$

where $k_0^2 = \omega^2 \mu_0 \varepsilon_0$ is the vacuum wave number.

Annexe E

Permittivity calculation as function of relative density : EMA approximation

Different algebraic mixing laws can be used to describe the dielectric properties as function of the relative density [36]. The effective medium approximation (EMA) originally proposed by Bruggeman [18] is used in this work. The principle of this approximation is to consider the medium composed of spherical inclusions with different properties ($\epsilon_i, \overline{\rho}_i, \dots$).

The permittivity of the effective medium $\epsilon_{eff} = \epsilon'_{eff} - j\epsilon''_{eff}$, is deduced by solving the following relationship [91] :

$$C_{Al_2O_3} \left(\frac{\epsilon_{Al_2O_3} - \epsilon_{eff}}{\epsilon_{Al_2O_3} + 2\epsilon_{eff}} \right) + C_{gas} \left(\frac{\epsilon_{gas} - \epsilon_{eff}}{\epsilon_{gas} + 2\epsilon_{eff}} \right) = 0 \quad (E.1)$$

where $\epsilon_{Al_2O_3}$ is the alumina complex dielectric permittivity, ϵ_{gas} is the gas complex dielectric permittivity which is assumed to be 1, $C_{Al_2O_3}$ is the volume fraction of alumina and C_{gas} is the volume fraction of gas. Note that the volume fraction of gas C_{gas} corresponds to the porosity, equal to 1 minus the relative density D :

$$C_{gas} = \frac{V_{gas}}{V_{tot}} = 1 - D \quad (E.2)$$

where V_{gas} is the volume of gas present in the sample volume V_{tot} .

Combining Equation (E.1) and Equation (E.2) leads to :

$$D \left(\frac{\epsilon_{Al_2O_3} - \epsilon_{eff}}{\epsilon_{Al_2O_3} + 2\epsilon_{eff}} \right) + (1 - D) \left(\frac{\epsilon_{gas} - \epsilon_{eff}}{\epsilon_{gas} + 2\epsilon_{eff}} \right) = 0 \quad (E.3)$$

Equation (E.3) can be written also as :

$$\frac{D\epsilon_{Al_2O_3} - D\epsilon_{eff}}{\epsilon_{Al_2O_3} + 2\epsilon_{eff}} = \frac{\epsilon_{eff} - D\epsilon_{eff} - \epsilon_{gas} + D\epsilon_{gas}}{\epsilon_{gas} + 2\epsilon_{eff}} \quad (E.4)$$

or,

$$(D\epsilon_{Al_2O_3} - D\epsilon_{eff})(\epsilon_{gas} + 2\epsilon_{eff}) = (\epsilon_{Al_2O_3} + 2\epsilon_{eff})(\epsilon_{eff} - D\epsilon_{eff} - \epsilon_{gas} + D\epsilon_{gas}) \quad (E.5)$$

Developing Equation (E.5), this last is written in a polynomial form as :

$$\underbrace{2}_{a} \varepsilon_{eff}^2 + \varepsilon_{eff} \underbrace{[(1-3D)\varepsilon_{Al_2O_3} + (3D-2)\varepsilon_{gas}]}_b - \underbrace{\varepsilon_{Al_2O_3}\varepsilon_{gas}}_c = 0 \quad (E.6)$$

Equation (E.6) is an equation of second order in $\varepsilon_{eff} = \varepsilon'_{eff} - j\varepsilon''_{eff}$. To solve this last a positive discriminant $\Delta = b^2 - 4ac$ is first calculated for ε'_{eff} , then for ε''_{eff} . Two solutions are found for both compound (ε'_{eff} , ε''_{eff}), one negative and one positive. Only the positive solution is retained, $\varepsilon_{eff} = (-b + \sqrt{\Delta})/2a$. As $\varepsilon_{Al_2O_3}$, the permittivity of alumina, is temperature dependent (Appendix C), the coefficient b and c also depend on temperature, and so does ε'_{eff} and ε''_{eff} . Figure E.1 presents the real part of the effective permittivity using EMA for a relative density $D = 43.8\%$

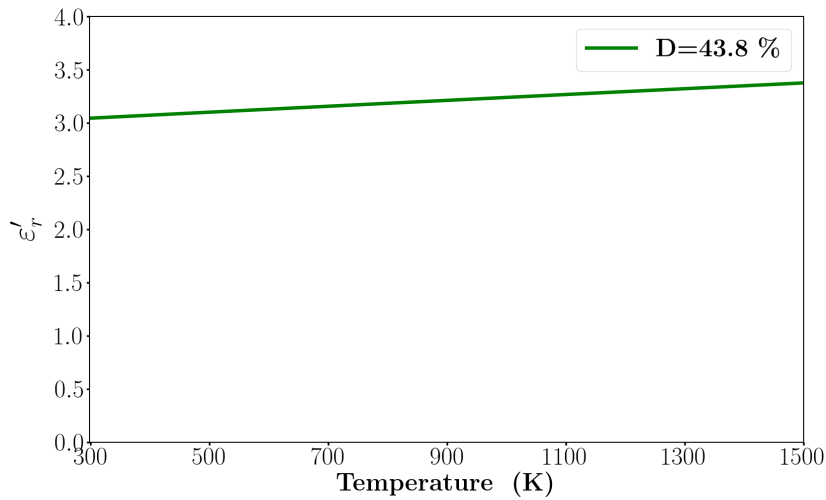


FIGURE E.1 – Real part of the permittivity using EMA approximation for a relative density $D = 43.8\%$.

Bibliographie

- [1] H. ABDERRAZAK et E.S HMIDA. « Silicon Carbide : Synthesis and Properties ». In : *Properties and Applications of Silicon Carbide*. Sous la dir. de Rosario GERHARDT. Rijeka : IntechOpen, 2011. Chap. 16.
- [2] D. AGRAWAL. « 9 - Microwave sintering of ceramics, composites and metal powders ». In : *Sintering of Advanced Materials*. Sous la dir. de Zhigang Zak FANG. Woodhead Publishing Series in Metals and Surface Engineering. Woodhead Publishing, 2010, p. 222 -248.
- [3] D. AGRAWAL. « Microwave Sintering of Ceramics, Composites and Metallic Materials, and Melting of Glasses ». In : *Transactions of the Indian Ceramic Society* 65 (2006), p. 129 -144.
- [4] D. AGRAWAL. « Microwave sintering of metal powders ». In : *Advances in Powder Metallurgy*. Sous la dir. d'Isaac CHANG et Yuyuan ZHAO. Woodhead Publishing, 2013, p. 361 -379.
- [5] D. AGRAWAL, J. CHENG, H. PENG, L. HURT et K. CHERIAN. « Microwave Energy Applied to Processing of High-Temperature Materials ». In : *Am. Ceram. Soc. Bull.* 87 (mar. 2008).
- [6] T. L. ALFORD, M. J. GADRE, R. N. P. VEMURI et N. D. THEODORE. « Susceptor-assisted microwave annealing for activation of arsenic dopants in silicon ». In : *Thin Solid Films* 520.13 (2012), p. 4314 -4320.
- [7] *Alumina thermal parameters* : <http://www-ferp.ucsd.edu/LIB/PROPS/PANOS/al2o3.html>.
- [8] *American Society for Testing and Materials*. <https://www.astm.org/>.
- [9] M. F. ASHBY. « A first report on sintering diagrams ». In : *Acta Metallurgica* 22.3 (1974), p. 275 -289.
- [10] K. G. AYAPPA, H. T. DAVIS, G. CRAPISTE, E. A. DAVIS et J. GORDON. « Microwave heating : an evaluation of power formulations ». In : *Chemical Engineering Science* 46.4 (1991), p. 1005 -1016.
- [11] T. A. BAERAKY. « Microwave measurements of the dielectric properties of silicon carbide at high temperature ». In : *Egypt. J. Sol* 25.(2) (2002), 263-273.
- [12] *BAIKOWSKI@society* : <url=https://www.baikowski.com/fr/>.
- [13] J. BATT, W. H. SUTTON, J. G.P. BINNER et T. E. CROSS. « A parallel measurement programme in high temperature dielectric property measurement : An update ». In : (1995).

- [14] F. BECKER. « Surface temperature and emissivity at various scales : Definition, measurement and related problems ». In : *Remote Sensing Reviews* 12 (jan. 1995).
- [15] M. BHATTACHARYA et T. BASAK. « A review on the susceptor assisted microwave processing of materials ». In : *Energy* 97 (2016), p. 306-338.
- [16] M. BIESUZ et V. M. SGLAVO. « Flash sintering of ceramics ». In : *Journal of the European Ceramic Society* 39.2 (2019), p. 115 -143.
- [17] M. BRAGINSKY, V. TIKARE et E.A. OLEVSKY. « Numerical simulation of solid state sintering ». In : *International Journal of Solids and Structures* 42.2 (2005). *Micro-mechanics of Materials*, p. 621 -636.
- [18] D. A. G. BRUGGEMAN. « Berechnung verschiedener physikalischer Konstanten von heterogenen Substanzen. I. Dielektrizitätskonstanten und Leitfähigkeiten der Mischkörper aus isotropen Substanzen ». In : *Annalen der Physik* 416 (1935), p. 636-664.
- [19] Y. V. BYKOV, K. I. RYBAKOV et V. E. SEMENOV. « High-temperature microwave processing of materials ». In : *Journal of Physics D : Applied Physics* 34.13 (2001), R55.
- [20] J. P. CALAME, K. RYBAKOV, Y. CARMEL, D. GERSHON, W. H. SUTTON, D. A. LEWIS et D. E. CLARK. « Electric Field Intensification in Spherical Neck Ceramic Microstructures During Microwave Sintering, World congress; 1st, Microwave processing ». In : *CERAMIC TRANSACTIONS, Microwave processing, World congress; 1st, Microwave processing*. T. 80. American Ceramic Society; 1997, p. 135-142.
- [21] S. CHARMOND, C. P. CARRY et D. BOUVARD. « Densification and microstructure evolution of Y-Tetragonal Zirconia Polycrystal powder during direct and hybrid microwave sintering in a single-mode cavity ». In : *Journal of the European Ceramic Society* 30.6 (2010), p. 1211 -1221.
- [22] D. CLARK et W. SUTTON. « Microwave Processing of Materials III ». In : *Annual Review of Materials Research* 26 (2003), p. 299-331.
- [23] COMSOL Multiphysics®. <https://www.comsol.com>.
- [24] ©RATH-Group : <https://www.rath-group.com/en/products/insulating-fire-bricks>.
- [25] National Research COUNCIL. *Microwave Processing of Materials*. Washington, DC : The National Academies Press, 1994.
- [26] J. CROQUESEL. « Etude des spécificités du frittage par micro-ondes de poudres d'alumine alpha et gamma ». PhD thesis. Université Grenoble Alpes, 2015.
- [27] J. CROQUESEL, D. BOUVARD, J.M. CHAIX, C. P. CARRY et S. SAUNIER. « Development of an instrumented and automated single mode cavity for ceramic microwave sintering : Application to an alpha pure alumina powder ». In : *Materials & Design* 88 (2015), p. 98 -105.
- [28] L. ČURKOVIĆ, M. F. JELAČA et S. KURAJICA. « Corrosion behavior of alumina ceramics in aqueous HCl and H₂SO₄ solutions ». In : *Corrosion Science* 50.3 (2008), p. 872 -878.

- [29] R. DOREY. « Chapter 4 - Microstructure–property relationships : How the microstructure of the film affects its properties ». In : *Ceramic Thick Films for MEMS and Microdevices*. Sous la dir. de Robert DOREY. Micro and Nano Technologies. Oxford : William Andrew Publishing, 2012, p. 85 -112.
- [30] *E-Field and H-Field distributions in different modes in rectangular waveguides* : <https://electronics.stackexchange.com/questions/268431/what-is-the-simple-meaning-of-te10-waveguide>.
- [31] Z. C. FENG. *SiC Power Materials : Devices and Applications*. Springer Series in Materials Science. Springer Berlin Heidelberg, 2013.
- [32] FLIR® A655sc : <https://www.flir.fr/products/a655sc/model=55001-0302>.
- [33] *Fluke® Endurance® Series documentation*. http://support.fluke.com/ircon-sales/Download/Asset/6006198_6252_ENG_E_W.PDF.
- [34] E. GAFFET. "Spark Plasma Sintering". Sous la dir. d'Innovation 128. 2004.
- [35] R. M. GERMAN. *Sintering Theory and Practice*. Wiley, 1996.
- [36] D. GERSHON, J. CALAME et A. BIRNBOIM. « Complex permittivity measurements and mixing laws of porous alumina ». In : *Journal of Applied Physics* 89 (juin 2001).
- [37] I. GHORBEL, P. GANSTER, N. MOULIN, C. MEUNIER et J. BRUCHON. « Experimental and numerical thermal analysis for direct microwave heating of silicon carbide ». In : *Journal of the American Ceramic Society* (2020).
- [38] B. D. GUENTHER. « Electromagnetic Theory ». In : *Modern Optics*. 2^e éd. Oxford; New York, NY : OUP Oxford, 2015, p. 15-51.
- [39] M. GUPTA et W.L.E. WONG. « Microwaves – Theory ». In : *Microwaves and Metals*. John Wiley & Sons, Ltd, 2007. Chap. 2, p. 25-41.
- [40] H. A. HAUS et J. R. MELCHER. *Electromagnetic fields and energy / Hermann A. Haus, James R. Melcher*. English. Prentice Hall Englewood Cliffs, N.J, 1989, xxiii, 742 p. :
- [41] W. HERMEL, G. LEITNER et R. KRUMPHOLD. « Review of Induction Sintering : Fundamentals and Applications ». In : *Powder Metallurgy* 23.3 (1980), p. 130-135.
- [42] R. HEUGUET, S. MARINEL, A. THUAULT et A. BADEV. « Effects of the Susceptor Dielectric Properties on the Microwave Sintering of Alumina ». In : *Journal of the American Ceramic Society* 96 (2013).
- [43] A. I. HOFMANN, R. KROON et C MÜLLER. « 13 - Doping and processing of organic semiconductors for plastic thermoelectrics ». In : *Handbook of Organic Materials for Electronic and Photonic Devices (Second Edition)*. Sous la dir. d'Oksana OSTROVERKHOVA. Second Edition. Woodhead Publishing Series in Electronic and Optical Materials. Woodhead Publishing, 2019, p. 429 -449.
- [44] S. HORIKOSHI, R. SCHIFFMANN, J. FUKUSHIMA et N. SERPONE. *Microwave Chemical and Materials Processing : A Tutorial*. 2018.
- [45] S. HORIKOSHI et N. SERPONE. « General Introduction to Microwave Chemistry ». In : *Microwaves in Catalysis*. John Wiley & Sons, Ltd, 2015. Chap. 1, p. 1-28.

- [46] M. F. ISKANDER, R. L. SMITH, A. O. M. ANDRADE, H. KIMREY et L. M. WAL. « FDTD simulation of microwave sintering of ceramics in multimode cavities ». In : *IEEE Transactions on Microwave Theory and Techniques* 42.5 (1994), p. 793-800.
- [47] J. D. JACKSON. *Classical electrodynamics*. 3rd ed. Wiley, 1999.
- [48] V. KARAYANNIS. « Microwave sintering of ceramic materials ». In : *IOP Conference Series Materials Science and Engineering* 161 (2016), p. 012068.
- [49] T. KIM, J. LEE et K. LEE. « Microwave heating carbon-based solid materials ». In : *Carbon letters* 15 (2014), p. 15-24.
- [50] D. LANCE, F. VALDIVIESO et P. GOEURIOT. « Correlation between densification rate and microstructural evolution for pure alpha alumina ». In : *Journal of the European Ceramic Society* 24.9 (2004), p. 2749 -2761.
- [51] L. LBOS, M. MARCHETTI, A. BOUDENNE, S. DATCU, Y. CANDAU et J. LIVET. « Infrared emissivity measurement device : principle and applications ». In : *Measurement Science and Technology* 17.11 (2006), p. 2950-2956.
- [52] R. MACAIGNE. « Frittage micro-ondes du matériau spinelle $MgAl_2O_4$: vers des céramiques transparentes ». PhD thesis. Normandie Université, 2017.
- [53] R. MACAIGNE, S. MARINEL, D. GOEURIOT, C. MEUNIER, S. SAUNIER et G. RIQUET. « Microwave sintering of pure and TiO_2 doped $MgAl_2O_4$ ceramic using calibrated, contactless in-situ dilatometry ». In : *Ceramics International* 42.15 (2016), p. 16997 -17003.
- [54] Yukio MAKINO, T. OHMAE, Yuichi SETSUHARA, S. MIYAKE et Sadao SANO. « Sintering of Al_2O_3 - ZrO_2 Composites Using Millimeter-Wave Radiation ». In : *The Science of Engineering Ceramics II*. T. 161. Key Engineering Materials. •. Trans Tech Publications Ltd, juil. 1998, p. 41-44.
- [55] C. MANIÈRE, S. CHAN et E. A. OLEVSKY. « Microwave sintering of complex shapes : From multiphysics simulation to improvements of process scalability ». In : *Journal of the American Ceramic Society* 102.2 (2019), p. 611-620.
- [56] C. MANIÈRE, L. GEUNTAK, T. ZAHRAH et E. A. OLEVSKY. « Microwave flash sintering of metal powders : From experimental evidence to multiphysics simulation ». In : *Acta Materialia* 147 (2018), p. 24 -34.
- [57] C. MANIÈRE, T. ZAHRAH et E. A. OLEVSKY. « Fully coupled electro-magnetic-thermal-mechanical comparative simulation of direct vs hybrid microwave sintering of 3Y- ZrO_2 ». In : *Journal of the American Ceramic Society* 100.6 (2016), p. 2439-2450.
- [58] C. MANIÈRE, T. ZAHRAH et E. A. OLEVSKY. « Inherent heating instability of direct microwave sintering process : Sample analysis for porous 3Y- ZrO_2 ». In : *Scripta Materialia* 128 (2017), p. 49 -52.
- [59] S. MARINEL, C. MANIÈRE, A. BILOT, C. BILOT, C. HARNOIS, G. RIQUET, F. VALDIVIESO, C. MEUNIER, C. COUREAU et F. BARTHÉLEMY. « Microwave Sintering of Alumina at 915 MHz : Modeling, Process Control, and Microstructure Distribution ». In : *Materials* 12 (2019), p. 2544.

- [60] M. MASSOUD. *Engineering Thermofluids : Thermodynamics, Fluid Mechanics, and Heat Transfer*. Springer Berlin Heidelberg, 2005.
- [61] *Materials Emissivity Table* : https://www.engineeringtoolbox.com/emissivity-coefficients-d_447.html.
- [62] *MatWeb Material Property Data*. url=<http://www.matweb.com/>.
- [63] V. MEDA, V. ORSAT et V. RAGHAVAN. « 2 - Microwave heating and the dielectric properties of foods ». In : *The Microwave Processing of Foods (Second Edition)*. Sous la dir. de Marc REGIER, Kai KNOERZER et Helmar SCHUBERT. Second Edition. Woodhead Publishing Series in Food Science, Technology and Nutrition. Woodhead Publishing, 2017, p. 23 -43.
- [64] P. MELINON et B. MASENELLI. *From Small Fullerenes to Superlattices : Science and Applications*. Science and Applications. Jenny Stanford Publishing, 2012.
- [65] R. J. MEREDITH. *Engineers' Handbook of Industrial Microwave Heating*. Power & Energy Series. The Institution of Engineering et Technology, 1998.
- [66] R. J. MEREDITH et A. C. METAXAS. *Industrial microwave heating*. IEE power engineering series 4. Peter Peregrinus, 1993.
- [67] R. R. MISHRA et A. K. SHARMA. « Microwave-material interaction phenomena : Heating mechanisms, challenges and opportunities in material processing ». In : *Composites Part A : Applied Science and Manufacturing* 81 (2016), p. 78 -97.
- [68] *Modline®5 Infrared Thermometers* : <http://www.eustispyrocom.com/documents/pages/Modline5.pdf>.
- [69] A.S. MUKASYAN. « Silicon Carbide ». In : *Concise Encyclopedia of Self-Propagating High-Temperature Synthesis*. Sous la dir. d'Inna P. BOROVINSKAYA, Alexander A. GROMOV, Evgeny A. LEVASHOV, Yuri M. MAKSIMOV, Alexander S. MUKASYAN et Alexander S. ROGACHEV. Amsterdam : Elsevier, 2017, p. 336 -338.
- [70] D. V. OLEVSKY E. A. and Dudina. « Induction Heating Sintering ». In : *Field-Assisted Sintering : Science and Applications*. Cham : Springer International Publishing, 2018, p. 275-291.
- [71] E. A. OLEVSKY. « SINTERING THEORY ». In : Spring School. 2011.
- [72] E. A. OLEVSKY. « Theory of sintering : from discrete to continuum ». In : *Materials Science and Engineering : R : Reports* 23.2 (1998), p. 41 -100.
- [73] E. A. OLEVSKY et D. V. DUDINA. *Field-assisted Sintering : Science and Applications*. New York, NY : Springer International Publishing AG, 2018.
- [74] E. A. OLEVSKY et D. V. DUDINA. « Flash Sintering ». In : *Field-Assisted Sintering : Science and Applications*. Springer International Publishing, 2018, p. 193-232.
- [75] E. A. OLEVSKY et D. V. DUDINA. « Microwave Sintering ». In : *Field-Assisted Sintering : Science and Applications*. Springer International Publishing, 2018, p. 237-274.
- [76] E. A. OLEVSKY et D. V. DUDINA. « Sintering by Low-Voltage Electric Pulses (Including Spark Plasma Sintering (SPS)) ». In : *Field-Assisted Sintering : Science and Applications*. Springer International Publishing, 2018, p. 89-191.

- [77] E. A. OLEVSKY, V. TIKARE et T. GARINO. « Multi-Scale Study of Sintering : A Review ». In : *Journal of the American Ceramic Society* 89.6 (2006), p. 1914-1922.
- [78] *opti'Waves startup* : <https://opti-waves.com/>.
- [79] K. D. PAULSEN, D. R. LYNCH et J. W. STRAHBEHN. « Three-dimensional finite, boundary, and hybrid element solutions of the Maxwell equations for lossy dielectric media ». In : *IEEE Transactions on Microwave Theory and Techniques* 36.4 (1988), p. 682-693.
- [80] S. J. PENN, N. M. ALFORD, A. TEMPLETON, X. WANG, M. XU, M. REECE et K. SCHRAPEL. « Effect of Porosity and Grain Size on the Microwave Dielectric Properties of Sintered Alumina ». In : *Journal of the American Ceramic Society* 80.7 (1997), p. 1885-1888.
- [81] E. PERT, Y. CARMEL, A. BIRNBOIM, T. OLORUNYOEMI, D. GERSHON, J. CALAME, I. K. LLOYD et O. C. WILSON. « Temperature Measurements during Microwave Processing : The Significance of Thermocouple Effects ». In : *Journal of the American Ceramic Society* 84.9 (2001), p. 1981-1986.
- [82] D.H. PINO-MUNOZ. « High-performance computing of sintering process at particle scale. » PhD thesis. Mines Saint-Étienne, 2012.
- [83] *Poyting vector demonstration* : [url=http://www.amanogawa.com/archive/docs/EM8.pdf](http://www.amanogawa.com/archive/docs/EM8.pdf).
- [84] D. M. POZAR. *Microwave Engineering*. Wiley-BT. Wiley, 1998.
- [85] X. QIAO et X. XIE. « The effect of electric field intensification at interparticle contacts in microwave sintering ». In : *Scientific Reports* 6 (sept. 2016), p. 32163.
- [86] M. N. RAHAMAN. *Ceramic Processing and Sintering*. T. 875. 2003.
- [87] M.N. RAHAMAN. « 2 - Kinetics and mechanisms of densification ». In : *Sintering of Advanced Materials*. Sous la dir. de Zhigang Zak FANG. Woodhead Publishing Series in Metals and Surface Engineering. Woodhead Publishing, 2010, p. 33 -64.
- [88] A. RANA, M. KANG et H. KIM. « Microwave-assisted Facile and Ultrafast Growth of ZnO Nanostructures and Proposition of Alternative Microwave-assisted Methods to Address Growth Stoppage ». In : *Scientific Reports* 6 (avr. 2016), p. 24870.
- [89] M. REGIER, K. KNOERZER et H. SCHUBERT. « 1 - Introducing microwave-assisted processing of food : Fundamentals of the technology ». In : *The Microwave Processing of Foods (Second Edition)*. Sous la dir. de Marc REGIER, Kai KNOERZER et Helmar SCHUBERT. Second Edition. Woodhead Publishing Series in Food Science, Technology and Nutrition. Woodhead Publishing, 2017, p. 1 -22.
- [90] R. ROY, D. K. AGRAWAL, J. CHENG et S. GEDEVANISHVILI. « Full sintering of powdered-metal bodies in a microwave field ». In : *Nature* 399 (1999), p. 668-670.
- [91] K. I. RYBAKOV, E. A. OLEVSKY et E. V. KRIKUN. « Microwave Sintering : Fundamentals and Modeling ». In : *Journal of the American Ceramic Society* 96 (2013), p. 1003-1020.
- [92] *SAIREM documentation*. [url=https://www.sairem.com/wp-content/uploads/2019/02/GMSP10-EN.pdf](https://www.sairem.com/wp-content/uploads/2019/02/GMSP10-EN.pdf).

- [93] C. SALTIEL et A. K. DATTA. « Heat and Mass Transfer in Microwave Processing ». In : sous la dir. de James P. HARTNETT, Thomas F. IRVINE, Young I. CHO et George A. GREENE. T. 33. *Advances in Heat Transfer*. Elsevier, mar. 1999, p. 1 -94.
- [94] J. SAMUELS et J. R. BRANDON. « Effect of composition on the enhanced microwave sintering of alumina-based ceramic composites ». In : *Journal of Materials Science* 27.12 (1992), p. 3259-3265.
- [95] *SCERAM Advanced Ceramics*. url=<https://www.sceram.com/carbure-de-silicium/>.
- [96] *SensorTec-Thermocouple Theory*. <http://www.sensortecinc.com/TCTheory.aspx>.
- [97] J. SHI. « Experiment and simulation of micro injection molding and microwave sintering ». Thèse de doct. Besançon : Université de Franche-Comté, 2014.
- [98] T. SHIRAI, H. WATANABE, M. FUJI et M. TAKAHASHI. « Structural properties and surface characteristics on aluminum oxide powders ». In : *Ceramics Research Lab* 9 (2009), p. 23-31.
- [99] S. SINGH, D. GUPTA, V. JAIN et A. SHARMA. « Microwave Processing of Materials and Applications in Manufacturing Industries : A Review ». In : *Materials and Manufacturing Processes* 30.1-29 (2014).
- [100] E. M. SPARROW, L. U. ALBERS et E. R.G. ECKERT. « Thermal radiation characteristics of cylindrical enclosures ». English (US). In : *Journal of Heat Transfer* 84.1 (1962), p. 73-79.
- [101] W. SUTTON. « Microwave Processing of Ceramics - An Overview ». In : *MRS Proceedings* 269 (2011).
- [102] *TE and TM modes* : <http://www.engineeringdone.com/te-tm-modes/te-tm-modes/>.
- [103] *Thermocouple fundamentals*. <https://eu.flukecal.com/fr/literature/articles-and-education/temperature-calibration/application-notes/thermocouple-app-notes-s>.
- [104] H. TOSSOUKPE. « Modélisation et simulation du frittage de matériaux dopés et de multimatériaux à l'échelle de la microstructure ». PhD thesis. Mines Saint-Étienne, 2013.
- [105] P. VERONESI. « Microwave Chemistry ». In : sous la dir. de Giancarlo CRAVOTTO et Diego CARNAROGGIO. De Gruyter, 2017. Chap. 2. An Introduction to dielectric heating, 18–30.
- [106] J. WANG. « Evidence for the microwave effect during hybrid sintering and annealing of ceramics ». PhD thesis. Loughborough University, 2006.
- [107] *Waveguide sizes* : <https://www.everythingrf.com/tech-resources/waveguides-sizes>.
- [108] M. J. WHITE, M. F. ISKANDER et Z. HUANG. « Development of a multigrid FDTD code for three-dimensional applications ». In : *IEEE Transactions on Antennas and Propagation* 45.10 (1997), p. 1512-1517.
- [109] M. J. WHITE, M. F. ISKANDER, Zhenlong HUANG et H. D. KIMREY. « A three dimensional multi-grid FDTD code for modeling microwave sintering of materials ». In : *IEEE Antennas and Propagation Society International Symposium. 1996 Digest*. T. 1. 1996, 120-123 vol.1.

- [110] N. YOSHIKAWA. « Recent Studies on Fundamentals and Application of Microwave Processing of Materials ». In : 2011. Chap. 1.
- [111] F. ZUO, S. SAUNIER, S. MARINEL, P. CHANIN-LAMBERT, N. PEILLON et D. GOEURIOT. « Investigation of the mechanism(s) controlling microwave sintering of α -alumina : Influence of the powder parameters on the grain growth, thermodynamics and densification kinetics ». In : *Journal of the European Ceramic Society* 35.3 (2015), p. 959 -970.
- [112] D. ZYMELKA. « Suivi par methode optique du frittage micro-ondes d'oxydes ceramiques. » PhD thesis. Mines Saint-Étienne, 2012.

Publications and conferences during the thesis

Articles in international journals

- I. Ghorbel, P. Ganster, N. Moulin, C. Meunier and J. Bruchon, (2020), Experimental and numerical thermal analysis for direct microwave heating of Silicon Carbide. J Am Ceram Soc.

Conference participation

- Oral presentation acceptance at CIMTEC (15 th INTERNATIONAL CONFERENCES MATERIALS AND TECHNOLOGIES) 2020 Montecatini Terme, Italy. Postponed 2021 (Covid-19).
- Oral presentation acceptance at the GFC (French Group of the Ceramics) 2020 Caen, France. Postponed 2021 (Covid-19).
- Participation in the best poster competition acceptance at the GFC (French Ceramics Group) 2020 Caen, France. Postponed 2021 (Covid-19).
- Oral presentation at ECerS (European Ceramic Society) 2019 Turin, Italy.
- Oral presentation at Poudres 2019 Grenoble, France.

École Nationale Supérieure des Mines
de Saint-Étienne

NNT : *Communiqué le jour de la soutenance*

Inès GHORBEL

Numerical and experimental study of the heating of alumina under microwave field in hybrid configuration. Application to sintering.

Speciality : Mechanics and Engineering

Keywords : sintering, microwave heating, multi-physics simulation, silicon carbide, alumina.

Abstract :

The use of microwave heating to produce ceramics is an interesting way to obtain a faster densification compared to conventional heating. The objective of this thesis is to study, experimentally and numerically, the microwave sintering of alumina (Al_2O_3) in a 2.45 GHz single-mode cavity in a hybrid configuration. For this purpose, silicon carbide (SiC) is used as a susceptor due to its high permittivity. The first part of this work focused on the study of the heating of parallelepipedic SiC samples. The first part of this work focused on the study of the heating of SiC parallelepipedic samples. It allowed, on the one hand, to validate the simulations carried out with the finite element simulation software *COMSOL Multiphysics*® and, on the other hand, to report on the evolution of the temperature field as a function of its orientation in the electric field. The results show that the heating is more efficient for certain orientations of the sample. A good agreement between experimental measurements and numerical results was obtained. This orientation is subsequently used to study experimentally and numerically the heating of alumina samples of different densities. The experimental results show that the lower the density of the sample, the higher the heating efficiency. Furthermore, a complex evolution of the sample temperature is observed. To analyse these experimental results, simulations with *COMSOL* were carried out. The third part of this thesis, resulting from a collaboration between the Mines Saint-Étienne and the CRISMAT laboratory in Caen, studies numerically and experimentally the sintering of alumina in hybrid configuration. The first results of this study show that all the power absorbed is by the susceptors which then heat the alumina sample by radiation. Again, the experimental trends are found numerically, and the main differences can be explained.

École Nationale Supérieure des Mines
de Saint-Étienne

NNT : *Communiqué le jour de la soutenance*

Inès GHORBEL

Étude numérique et expérimentale du chauffage de l'alumine sous champ micro-onde en configuration hybride. Application au frittage.

Spécialité: Mécanique et Ingénierie

Mots clefs : frittage, chauffage micro-ondes, simulation multi-physique, carbure de silicium, alumine.

Résumé :

L'utilisation du chauffage micro-onde pour réaliser des céramiques est une voie intéressante permettant d'obtenir une densification plus rapide par rapport à un chauffage conventionnel. L'objectif de cette thèse est d'étudier, expérimentalement et numériquement, le frittage sous champ micro-onde de l'alumine (Al_2O_3) dans une cavité monomode 2,45 GHz, en configuration hybride. Pour cela, le carbure de silicium (SiC) est utilisé comme suscepteur en raison de sa permittivité élevée. La première partie de ce travail a porté sur l'étude du chauffage d'échantillons parallélépipédiques en SiC. Il a permis d'une part de valider les simulations réalisées avec le logiciel de simulation par éléments finis *COMSOL Multiphysics®*, d'autre part de rendre compte de l'évolution du champ de température en fonction de son orientation dans le champ électrique. Les résultats montrent que le chauffage est plus efficace pour certaines orientations de l'échantillon. Un bon accord entre les mesures expérimentales et résultats numériques ont été obtenus. Cette orientation est utilisée par la suite pour étudier expérimentalement et numériquement le chauffage d'échantillons d'alumine de différentes densités. Les résultats expérimentaux montrent que plus la densité de l'échantillon est faible, plus l'efficacité du chauffage est élevée. De plus, une évolution complexe de la température de l'échantillon est observée. Pour analyser ces résultats expérimentaux, des simulations avec *COMSOL* ont été réalisées. La troisième partie de cette thèse, issue d'une collaboration entre Mines Saint-Étienne et le laboratoire CRISMAT de Caen, étudie numériquement et expérimentalement le frittage de l'alumine en configuration hybride. Les premiers résultats de cette étude montrent que toute la puissance absorbée l'est par les suscepteurs qui chauffent ensuite l'échantillon d'alumine par rayonnement. Là aussi, les tendances expérimentales sont retrouvées numériquement, et les principales différences peuvent être expliquées.

